SEMMELWEIS EGYETEM

DOKTORI ISKOLA

Ph.D. értekezések

3286.

KIS NOÉMI

Funkcionális idegtudományok

című program

Programvezető: Dr. Sperlágh Beáta, egyetemi tanár

Témavezető: Dr. Makara Judit, csoportvezető

Diversity and cholinergic regulation of dendritic Ca^{2+} spikes in hippocampal CA3 pyramidal neurons

PhD thesis

Noémi Kis

János Szentágothai Neurosciences Division
Doctoral College, Semmelweis University

Supervisor: Judit Makara, MD, PhD

Official reviewers: Gábor Czirják, PhD
Attila Szűcs, PhD

Head of the Complex Examination Committee: Tibor Zelles, PhD

Members of the Complex Examination Committee:
Gábor Gerber, DMD, PhD
Katalin Schlett, PhD

Budapest
2025

TABLE OF CONTENTS

LIST OF ABBREVIATIONS

2P – two-photon

2PGU – two-photon glutamate uncaging

ACh – Acetylcholine

ACSF – artificial cerebrospinal fluid

ADP – afterdepolarization

AHP – afterhyperpolarization

AP – action potential

bAP – backpropagating action potential

CA (1-3) – cornu ammonis 1-3

CCh – cabachol

ChAT – choline acetyltransferase

ChR2 – channelrhodopsin

CSB – complex spike burst

CSB_H – high bursting cells

CSB_L – low bursting cells

CTX – ω-Conotoxin MVIIC

CV – coefficient of variation

DTX – dendrotoxin-I

DG – Dentate Gyrus

DI – dendritically initiated

dV/dt_{max} – maximum rate of rise

dV/dt_{min} – maximum rate of decay

dV/dt_{total} – total dV/dt range

EC – Entorhinal Cortex

EPSP – excitatory postsynaptic potential

GxTX - guangxitoxin

HC – hippocampus

HVA – high voltage activated

IbTx – iberiotoxin

I_{inj} – current injection

LVA – low voltage activated

mAChR – muscarinic acetylcholine receptor

MF – mossy fiber

nAChR – nicotinic acetylcholine receptor

nife – nifedipine

nimo – nimodipine

NMDA – N-methyl-D-aspartate

NMDAR – N-methyl-D-aspartate receptor

OGB-1 – Oregon Green 488 BAPTA-1

PC – pyramidal cell

PP – perforant path

RC – recurrent collateral

R_{in} – input resistance

RS – regular spiking

SD – standard deviation

SC – Schaffer collateral

SEM – standard error of mean

SLM – stratum lacunosum moleculare

STED – stimulated emission depletion

str. – stratum

Sub – subiculum

SWR – sharp wave ripple

TE – thorny excrescence

TTX – tetrodotoxin citrate

VGCC – voltage-gated Ca^{2+} channel

VGKC – voltage-gated K^{+} channel

VGNC – voltage-gated Na^{+} channel

V_m – membrane potential

1. INTRODUCTION

1.1. Overview of the hippocampus

The hippocampus is a C-shaped structure located in the temporal lobe of the brain. It is part of the limbic system and plays a fundamental role in several cognitive functions, especially those related to memory, learning, spatial navigation and emotional processing in mammals including humans (O'Keefe and Conway, 1978; Schiller et al., 2015). The hippocampus is in reciprocal relationship with almost all sensory and associative areas through the entorhinal and perirhinal cortices. One of its crucial functions is to support the formation and retrieval of memory traces, by constructing a cognitive map that binds and encodes spatial and contextual information (Andersen et al., 1971). An important component of this role is the processing of spatial memory, allowing individuals to recognize and navigate familiar environments, such as recalling the layout of a building or the route home. As widely studied cellular substrates of this mechanism in animals, place cells within the hippocampus fire in response to specific locations, contributing to the brain's internal representation of physical space (Eichenbaum, 2017; O'Keefe et al., 1971).

Besides spatial memory, the hippocampus is essential for processing declarative and episodic memories in humans (Buzsáki, 2015), and damage to this region can result in severe deficits, such as anterograde amnesia, where individuals struggle to form new memories while retaining older ones (as seen in the famous patient H.M.) (Corkin, 1984; Scoville and Milner, 2000). Additionally, the hippocampus interacts with the amygdala to regulate emotional memory (Yavas et al., 2019). It plays a vital role in neuroplasticity, allowing for the reorganization of neural circuits throughout life. It is particularly vulnerable to neurodegenerative diseases like Alzheimer's, as well as conditions such as stress and hypoxia, which can lead to significant cognitive impairments (Eichenbaum, 2013). Without a properly functioning hippocampus, our ability to form and retrieve memories would be severely compromised.

1.2. Structural organization and subfields of the hippocampus

The hippocampus is one of the most extensively studied brain regions. The hippocampus proper includes distinct subfields: Cornu Ammonis area 1 (CA1), CA2, CA3, the dentate gyrus (DG), and the subiculum. The main excitatory cell types are the

pyramidal cells (PCs) and the granule cells of the dentate gyrus. Its subfields are thought to form a sequential information processing network with special input systems and distinct roles.

Each subfield of the hippocampus exhibits a trilaminar organization, which is similar for all fields of the hippocampus, including a deep fiber layer, a principal cellular layer, and an outer molecular layer. The main cellular layer, known as the pyramidal cell layer or stratum (str.) pyramidale in the CA areas, is the principal site of the cell bodies of excitatory neurons. Beneath this layer lies the str. oriens, a narrow zone containing basal dendrites and afferent and efferent fibers. The molecular layer of the CA regions is subdivided into additional layers. Unique to CA3, is the str. lucidum, a thin band that sits directly above the pyramidal layer and contains mossy fiber (MF) axons originating from DG. At the distal end of the str. lucidum, a thickened region marks the transition between CA3 and CA2. While classical theories suggested that CA2 neurons lack MF input (Lorente de No, 1934), more recent studies (Chevaleyre and Siegelbaum, 2010; Kohara et al., 2014) using cell type specific molecular markers have shown that a small fraction of CA2PCs do receive MF projection, although these boutons are smaller and the density is lower than in the CA3. The str. radiatum contains the apical dendrites of neurons. The outermost hippocampal layer, str. lacunosum-moleculare (SLM) contains the apical tuft dendrites and houses perforant pathway fibers mostly from the entorhinal cortex (Andersen et al., 1971; Cappaert et al., 2015; van Strien et al., 2009) (**Fig. 1B**).

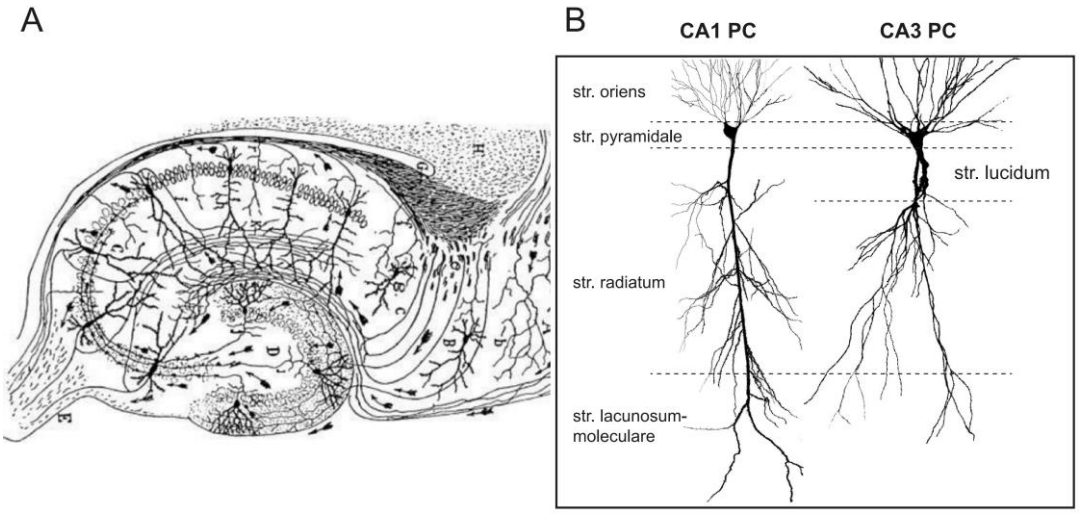

Figure 1. Structure and PCs of the hippocampus. **(A)** *Classical illustration of hippocampus, drawn by Santiago Ramón y Cajal.* **(B)** *Layers and morphological*

differences between CA1 and CA3 (own image of a CA1 and CA3PC, loaded with fluorescent dye).

1.3. The trisynaptic circuit

The cells in DG, CA3 and CA1 are connected via the 'trisynaptic loop' (Amaral and Witter, 1989; Andersen et al., 1971) (**Fig. 2A**).

The circuit begins in the entorhinal cortex (EC), where neurons in layer 2 project via the perforant path (PP) to the DG and also send axons to CA3PCs (Witter, 1993). This pathway carries information about spatial and contextual cues from various sensory modalities, providing the hippocampus with external sensory input.

The DG is thought to serve as a gatekeeper, regulating the flow of information into the hippocampus. It participates in pattern separation, the process by which similar inputs are differentiated into distinct representations, thus facilitating the formation of unique memories. From DG, granule cells project to proximal dendrites of CA3PCs via MFs which provide a sparse but powerful excitatory connection. Each granule cell typically forms about 15 synaptic contacts with different CA3PCs, and a single CA3PC receives input from ~50 MF boutons. This leads to a highly divergent and convergent connectivity pattern in the MF pathway (Henze et al., 2002; Vyleta et al., 2016). In addition to MF input, CA3PCs also receive excitatory input from the EC via the PP. While these inputs are more abundant, they are weaker than MF synapses (Ishizuka et al., 1990). CA3PCs also give prominent recurrent collaterals (RCs) to other CA3PCs that are proposed to be essential in pattern completion (Guzman et al., 2016). However, measurements of the actual connectivity rates in brain slice experiments yielded conflicting numbers that do not suggest particularly high interconnectivity. Guzman et al. found a very low rate of connectivity (0.9%) between CA3PCs of rats. However, Sammons et al. found ten times higher connectivity rate in mice (Sammons et al., 2024). A recent study (also in mice) showed that recurrent connectivity was abundant from superficial to deep, but almost absent from deep to superficial PCs (Watson et al., 2024).

The final stage of the trisynaptic circuit is the Schaffer collateral (SC) pathway, through which CA3PCs send projections to CA1PCs.

In addition to the canonical loop, a direct monosynaptic projection from layer 3 EC neurons – known as the temporoammonic pathway – targets the distal dendrites of CA1PCs. This input bypasses the DG and CA3 and allows cortical information to

influence CA1 activity more rapidly and directly, contributing to the integration of current sensory input with stored memory representations (Dvorak-Carbone and Schuman, 1999; Maccaferri and McBain, 1995).

CA1 integrates processed information from CA3 with direct input from layer 3 of the EC. CA1 then transmits information back to the deep layers of EC (layer 5), closing the loop of the trisynaptic circuit (Cenquizca and Swanson, 2007; Delatour and Witter, 2002).

The trisynaptic pathway is essential within the hippocampus, playing a key role in processing and encoding declarative memories, especially those related to spatial navigation and episodic memory. Since these connections are vital for transmitting and storing important information about the environment, it is crucial to understand how principal neurons integrate different input patterns and how this integration influences the output.

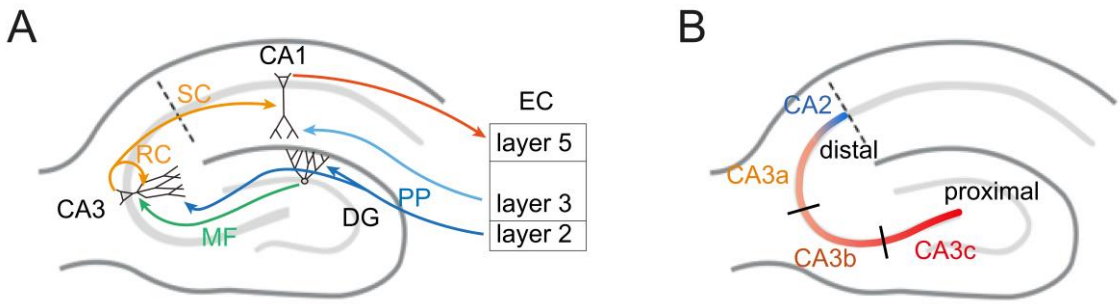

Figure 2. Schematic illustration of the hippocampal circuitry. (A) *The trisynaptic loop.* ***(B)*** *Subregions of the CA3 (own illustrations).*

1.4. Cellular heterogeneity in the CA3 region

CA3 is thought to be essential for memory recall due to its dense recurrent connectivity, which enables associative memory retrieval (pattern completion). This property allows for the reconstruction of previously stored information even when only partial cues are available. CA3 plays a critical role in associating incoming sensory information with stored memories, contributing to episodic memory formation.

Traditionally, CA3 has been considered a single interconnected network. However, accumulating evidence suggests significant functional heterogeneity along both the proximodistal (Kowalski et al., 2016; Sun et al., 2017) and radial (deep-superficial) axes

(Bilkey and Schwartzkroin, 1990; Fitch et al., 1989), reflecting differences in dendritic morphology, innervation patterns, and electrophysiological properties.

CA3 is commonly divided into three approximately equal-size subfields along the proximodistal axis, CA3a, b and c, which likely fulfill different functions when encoding spatial information (Sun et al., 2017) (**Fig. 2B**). Proximal CA3c PCs, located closest to the DG, receive strong MF input on both their apical and basal dendrites but have relatively sparse dendritic arborization in SLM, resulting in weak PP input (Sun et al., 2017). Distal CA3 neurons (CA3a and CA3b) have larger dendritic trees with significant recurrent input (Ishizuka et al., 1990; Witter, 2007). Notably, CA3a-CA3b PCs display more dendritic intersections in the SLM compared to CA3c PCs (Sun et al., 2017). Recent work by the Knierim and Moser groups suggests that the proximal CA3 may support pattern separation through interactions with the DG (GoodSmith et al., 2019), whereas distal CA3, where the RCs are more extensive, may rather play a role in pattern completion (Lee et al., 2015; Lu et al., 2015).

A small gradient in the resting membrane potential (V_m) has been identified, with CA3c having the most negative V_m followed by CA3b, CA3a and CA2. Another study found that the probability of burst-type activity is highest in CA3a, followed by b and c (Oliva et al., 2016; Spruston, 2008)

Furthermore, differences along the deep-superficial axis have been documented. Multiple studies (Bilkey and Schwartzkroin, 1990; Fitch et al., 1989; Watson et al., 2024) indicate that deep cells (with soma near str. oriens) are more likely to fire in bursts compared to superficial cells (with soma closer to str. radiatum). The most notable difference between these two cell subtypes is in the length of the proximal apical dendrite: deep-layer cells tend to have a longer primary apical dendrite.

Recent work from the Spruston lab in rodent slices has suggested the existence of a distinct class of bursting CA3PCs that lack MF input, as indicated by the absence of thorny excrescences (TE) – referred to as ‘athorny’ cells (Hunt et al., 2018). However, findings from the Jonas group propose a more flexible classification of CA3PCs. Their study in mouse slices demonstrated that the complete absence of TEs is not a strict requirement for subclass identity. Instead, deep CA3PCs exhibit burst firing phenotype and may have either sparse or absent MF input (Watson et al., 2024).

Based on these studies, it is evident that CA3 is not a homogeneous network. Rather, there is significant diversity in dendritic morphology and electrical properties depending on both proximodistal and radial positioning, highlighting distinct functional differences among its subregions.

1.5. Passive and active electrical properties of dendrites

The dendritic tree, which receives the majority of synaptic inputs, integrates those signals throughout a combination of passive and active electrical properties. This process, known as synaptic integration, is shaped by the spatial and temporal arrangement of inputs. When inputs arrive close together on a branch, they may summate in a sublinear fashion, producing a smaller effect than expected due to reduction in driving force. When inputs are more dispersed in time, their summation tends to be linear. In some cases, active ion channels boost the effect of individual inputs, creating supralinear summation (Gulledge et al., 2005; London and Häusser, 2005).

Passive membrane properties of dendrites influence electrical signals without active amplification by voltage-gated ion channels. These properties are determined by membrane resistance, axial resistance, and membrane capacitance, which collectively modulate how signals attenuate as they travel along the dendritic tree. These parameters influence the local amplitude, the kinetics and the dynamic interactions of synaptic events, as well as the propagation of synaptic voltage signals along dendrites. Passive properties are strongly influenced by dendritic morphology, including branching patterns (e.g. the presence of oblique dendrites) and diameter variations, affecting the integration of synaptic inputs and neuronal output. Computational models clearly demonstrated that dendritic morphology is important in shaping local synaptic responses (Gulledge et al., 2005; Stuart and Spruston, 2015).

Active electrical properties of dendrites enable neurons to dynamically shape and propagate electrical signals through voltage-gated ion channels. Unlike passive properties, which influence signal attenuation and integration, active properties allow dendrites to amplify and modulate the kinetics of voltage signals produced by synaptic inputs. Voltage-gated ion channels, such as Na^+, K^+, Ca^{2+} and non-specific cation channels (e.g. h-current) are critical for dendritic excitability, dendritic spike generation, and neuronal output (Gulledge et al., 2005; London and Häusser, 2005; Spruston, 2008).

1.5.1. Voltage-gated Na^+ channels (VGNCs)

VGNCs are primarily responsible for the initiation and propagation of action potentials (APs). While they are most concentrated at the axon initial segment, dendrites also express these channels (Lorincz and Nusser, 2010). In many neurons (e.g., hippocampal CA1PCs), APs can travel back actively into the dendrites (backpropagating APs (bAPs)) via Nav1.2 and Nav1.6 channels (Golding et al., 2001; Hu et al., 2009). This backpropagation plays a crucial role in synaptic plasticity. Additionally, Na^+ channels contribute to nonlinear synaptic integration by generating dendritic Na^+ spikes, one mechanism whereby clustered synaptic activation can lead to supralinear summation (Ariav et al., 2003; Losonczy and Magee, 2006; Sun et al., 2014; Waters et al., 2005).

1.5.2. Voltage-gated K^+ channels (VGKCs)

VGKCs counteract depolarization by repolarizing the membrane, shaping the action potential, shortening spike duration, and overall controlling firing patterns and synaptic integration. There are many different VGKC subtypes, which modulate dendritic excitability in distinct ways (Golding et al., 1999). Low threshold voltage activated Kv1 channels primarily influence AP threshold and neural excitability (Feria Pliego and Pedroarena, 2020). Kv2 channels mediate delayed rectifier K^+ current that regulates intrinsic excitability, repolarize the membrane after APs and limit dendritic spike duration (Bishop et al., 2015; Murakoshi and Trimmer, 1999; Palacio et al., 2017). Ca^{2+}-activated K^+ channels (BK, SK) link Ca^{2+} influx to changes in K^+ outflow, regulate neuronal excitability, shape AP duration and firing pattern. Large conductance BK channels contribute to fast afterhyperpolarization (AHP), spike repolarization, while small conductance SK channels mediate slow AHP, spike frequency adaptation and dampen dendritic EPSPs (Sah and Faber, 2002). A-type K^+ channels (Kv1.4, Kv3.4, Kv4.2, Kv4.3) also known as transient outward K^+ channels, which are defined by their rapid inactivation kinetics. They play a crucial role in the regulation of local Na^+ spike initiation and propagation, AP backpropagation, as well as synaptic integration and plasticity (Losonczy et al., 2008). To support these diverse roles, they are highly expressed in dendrites (Hoffman and Johnston, 1998; Kerti et al., 2012). M-type K^+ channels (Kv7/KCNQ) generate a slow outward current, stabilizing the membrane potential and preventing excessive firing or burst generation.

1.5.3. Voltage-gated calcium channels (VGCCs)

VGCCs are found in many cell types, and their properties may vary from cell to cell. They are essential mediators of neuronal excitability and intracellular calcium signaling, influencing synaptic transmission, plasticity, and intrinsic firing properties (Zamponi et al., 2015). They are classified into high-voltage-activated (HVA) and low-voltage-activated (LVA) channels based on their activation thresholds. The Cav1 (L-type) and Cav2 (P/Q-, N-, and R-type) families belong to the HVA category, requiring substantial depolarization to open, while Cav3 (T-type) channels are LVA, activating at more hyperpolarized potentials, a property making them critical for subthreshold oscillations and burst firing (Simms and Zamponi, 2014).

L-type Ca^{2+} channels (Cav1.1 - Cav1.4) exhibit slow inactivation (the "L" stands partly for long-lasting). Cav1.1 channels are predominantly expressed in skeletal muscle, Cav1.4 is mostly localized in retinal photoreceptors, but Cav1.2 and Cav1.3 channels are the most abundant in the brain and they are located postsynaptically on the soma and dendrites (Zamponi et al., 2015).

The Cav2 channel family includes three members: P/Q-, N- and R-type Ca^{2+} channels (Cav2.1, Cav2.2 and Cav2.3). These channels play roles in synaptic transmission and contribute to plasticity.

T-Type Ca^{2+} channels (Cav3.1–3.3) activate at low voltages and due to their hyperpolarized range of activation and inactivation they are suited to regulate neuronal excitability. They also contribute to rhythmic firing in neurons, pacemaker activity and enhancing temporal coding (Zamponi et al., 2015).

Na^+, K^+, and Ca^{2+} channels work together to regulate dendritic excitability, synaptic integration, and neuronal output. Na^+ channels drive AP generation and backpropagation, K^+ channels refine excitability and firing precision, while Ca^{2+} channels mediate synaptic plasticity and dendritic spike dynamics. Their interplay determines how neurons process information, encode memory, and generate complex firing patterns, making them essential for hippocampal and cortical computations.

1.5.4. NMDA receptors as active conductances

Although not voltage-gated in the classical sense, dendrites also contain N-methyl-D-aspartate receptors (NMDARs), which contribute to active synaptic integration and dendritic excitability. Due to the voltage-dependent removal of intracellular Mg^{2+} ions from the channel pore, NMDA receptors require both voltage depolarization and glutamate binding for efficient ion conductance, making them critical for coincidence detection and synaptic plasticity.

1.5.5. Dendritic spikes in the hippocampus

Dendritic ion channels are essential for shaping local voltage responses that eventually determine somatic firing patterns, yet their precise roles remain incompletely understood. Various voltage-gated ion channels can be activated by subthreshold excitatory postsynaptic potentials (EPSPs) (Magee and Johnston, 1995), while certain dendritic voltage-gated cation channels are capable of generating regenerative voltage responses, known as dendritic spikes, in response to strong synaptic input. These dendritic spikes can be mediated by voltage-gated Na^+ or Ca^{2+} channels or NMDARs, enhancing synaptic depolarization, modulating firing patterns, and contributing to synaptic plasticity.

The temporal and spatial characteristics of dendritic spikes depend on the type of ion channel involved and the dendritic compartment in which they are generated. Na^+ spikes are typically observed in small-diameter dendrites, but they can be also evoked in the main apical dendrites of cortical and hippocampal PCs, they are fast (lasting only a few milliseconds) and exhibit variable propagation, typically attenuating as they travel toward the soma (Gasparini et al., 2004). NMDAR-mediated spikes are typically initiated in thin basal and tuft dendritic compartments (Stuart and Spruston, 2015), they are slow (lasting tens of milliseconds) and remain spatially restricted, as they require both voltage depolarization and glutamate binding for activation (Major et al., 2008). Ca^{2+} spikes often occur in the main apical trunk of CA1PCs and layer 5 PCs, display intermediate durations (several tens of milliseconds) and propagate relatively effectively within the dendrites (Golding et al., 1999; Schiller et al., 1997).

While dendritic spikes are well-characterized in CA1PCs, less is known about their types and roles in CA3PCs. Pioneering work by the Jonas group suggested that CA3PC

dendrites can efficiently generate local Na^+ spikes, likely due to a high dendritic Na^+ channel density (Kim et al., 2012). Furthermore, our laboratory has identified synaptically evoked Na^+ and NMDA spikes in thin perisomatic basal and apical dendrites of CA3PCs, which receive RC inputs (Makara and Magee, 2013).

1.5.6. Dendritic Ca^{2+} spikes

Studies have shown that various PC types, including CA1 and cortical L5 PCs, can generate VGCC-mediated spikes – large, global events that lead to prolonged depolarization, typically occurring in the main apical dendrite (Francioni and Harnett, 2021; London and Häusser, 2005; Stuart and Spruston, 2015; Stuyt et al., 2021; Williams and Stuart, 1999). These Ca^{2+} spikes emerge in the apical dendrites in response to widespread synaptic depolarization, often coinciding with bAPs and complemented by NMDAR activation (Grienberger et al., 2014; Harnett et al., 2013; Larkum et al., 2009; Takahashi and Magee, 2009). At the soma, Ca^{2+} spikes manifest as an afterdepolarization (ADP) driving additional APs and thereby producing a characteristic complex spike bursts (CSBs) output (Lisman, 1997; Wong and Prince, 1978).

1.5.7. Complex spike burst (CSB)

CSBs represent a characteristic firing pattern of hippocampal PCs, consisting of high-frequency burst of 2–6 APs with progressively decreasing amplitude and increasing duration (Raus Balind et al., 2019). CSBs occur during goal-directed behavior, navigation, rest, and sharp-wave ripples (SWRs) (Bittner et al., 2015; Grienberger et al., 2014; Kowalski et al., 2016; Ranck, 1973; Zucca et al., 2017). A key mechanism underlying CSBs is the plateau potential, a prolonged dendritic depolarization event primarily mediated by Ca^{2+} and NMDA spikes. Once initiated, the plateau potential sustains neuronal excitability, leading to additional APs and burst firing. Recent in vivo intracellular recordings demonstrated that CSBs often occur when CA1PCs fire within place fields, and dendritic plateau potentials – whether spontaneous or experimentally induced – are sufficient to establish new place fields in previously silent CA1PCs (Bittner et al., 2017, 2015).

In vitro studies revealed that in CA1PCs CSBs are typically initiated by coincident activation of proximal SC and distal EC excitatory synapses, producing an ADP lasting ~20–60 ms at the soma (Bittner et al., 2017; Lisman, 1997). These bursts are thought to

encode associative input patterns and contribute to long-term synaptic plasticity (Takahashi and Magee, 2009).

Compared to CA1PCs, CA3PCs exhibit distinct dendritic morphology and connectivity, potentially leading to differences in CSB generation. However, the mechanisms underlying CSB generation in CA3PCs, as well as their role in vivo, remain poorly understood.

1.6. Neuromodulatory regulation of dendritic function

Beyond voltage-gated ion channels, neuronal activity is also influenced by various neuromodulatory systems, which fine-tune excitability, synaptic integration and plasticity. In the hippocampus, multiple neuromodulators, including acetylcholine, dopamine, serotonin, and norepinephrine, dynamically regulate neuronal function by modulating intrinsic membrane properties and synaptic transmission (Hasselmo, 1999; Palacios-Filardo and Mellor, 2019). Among these, the cholinergic system plays a crucial role in learning, memory, and attention. The cholinergic system and its specific effects on hippocampal activity will be introduced in the following chapter.

1.7. Cholinergic modulation of hippocampal neurons

The cholinergic system plays a critical role in the modulation of hippocampal function, influencing synaptic plasticity, neuronal excitability, and network oscillations. The hippocampus receives cholinergic input primarily from the medial septal nucleus, which projects extensively to the hippocampal formation, targeting pyramidal neurons and interneurons. Acetylcholine (ACh) exerts its effects via muscarinic (mAChRs) and nicotinic (nAChRs) receptors. Among mAChRs, the hippocampus expresses M1, M2, M3, and M4 receptors, with M1 and M3 receptors predominantly located on CA3PCs, and M2/M4 on GABAergic interneurons (Dasari and Gulledge, 2011; Hájos et al., 1998; Levey et al., 1995; Martinello et al., 2015). Activation of mAChRs leads to membrane depolarization, enhanced excitability, and persistent firing in PCs, effects that are thought to facilitate memory encoding and synaptic plasticity. nAChRs, particularly the α7 subtype, mediate fast synaptic responses and influence interneuron excitability, thereby modulating inhibitory control within hippocampal circuits (Cobb and Davies, 2005; Dannenberg et al., 2017; Prince et al., 2016).

Cholinergic activity helps to shape memory encoding and retrieval by modifying synaptic plasticity and network oscillations. Cholinergic modulation in CA3 is thought to balance memory encoding (pattern separation) and retrieval (pattern completion) by dynamically shifting network activity (Prince et al., 2016).

1.8. Unexplored properties and roles of the CA3 region

The CA3 region has long been recognized for its critical role in memory formation and retrieval, particularly in pattern completion and autoassociative network functions (Marr, 1971; McNaughton and Morris, 1987; Rolls, 2013). These theories are based on the dense recurrent connectivity among CA3PCs, which is thought to support the rapid storage and retrieval of associative memories from partial cues. However, despite these well-established concepts, several aspects of CA3's cellular and computational properties remain underexplored, especially regarding synaptic integration, plasticity mechanisms, and neuronal heterogeneity.

Although CA3PCs frequently generate CSBs both in vivo and in vitro (Ding et al., 2020; Hablitz and Johnston, 1981; Hunt et al., 2018; Kowalski et al., 2016; Mizuseki et al., 2012; Oliva et al., 2016) – sometimes more frequently than CA1PCs in vivo (Mizuseki et al., 2012; Oliva et al., 2016) –, the dendritic events underlying CSB generation remain largely unexplored. In vitro studies and computational models suggested that VGCCs contribute to CSB generation (Lazarewicz et al., 2002; Traub et al., 1994; Wong and Prince, 1978), but a detailed mechanistic understanding of the dendritic events underlying these bursts is still lacking.

While dendritic Na^+ and NMDA spikes have been demonstrated in CA3PCs (Brandalise et al., 2016; Kim et al., 2012; Makara and Magee, 2013), the mechanisms underlying dendritic Ca^{2+} spikes, key drivers of regenerative dendritic events and plateau potentials are still largely unknown. Early studies using blind microelectrode recordings observed putative dendritic Ca^{2+} spikes to which bursting was attributed (Nuñez and Buño, 1992; Wong et al., 1979), but these spikes have not been systematically examined.

Plateau potential has emerged as key mechanisms in synaptic plasticity and memory formation. These large, sustained depolarizations can induce a form of long-term synaptic modification known as behavioral time scale plasticity (BTSP), which operates over seconds rather than milliseconds (Bittner et al., 2017). Unlike traditional Hebbian models, where synaptic strengthening depends on precise millisecond-scale correlations between

presynaptic and postsynaptic activity, BTSP allows synapses to be modified by postsynaptic depolarization occurring even seconds after presynaptic activation. This mechanism has been well characterized in CA1PCs (Bittner et al., 2017, 2015), where it contributes to rapid place field formation and may play a crucial role in the formation of context-dependent memories. Interestingly, CA3PCs have higher incidence of long bursts than those in CA1 and recent results indicate that place field-inducing plateau potentials and CSBs in CA3PCs are particularly prolonged, lasting for up to several hundreds of milliseconds (Li et al., 2024). However, the dendritic mechanisms underlying such long-lasting regenerative events in CA3PCs remain poorly understood, and it is still unclear whether BTSP operates in CA3 with similar rules as in CA1.

One more striking feature is that unlike the long main, often unbranched apical trunks of CA1PCs, CA3PCs exhibit early bifurcation of their primary apical dendrites into multiple trunk branches. This creates distinct apical subtrees receiving laminally segregated inputs: MF synapses from the DG target the thick proximal dendrites in str. lucidum, RCs from other CA3PCs arrive to thinner higher-order basal and proximal apical dendrites and EC inputs targeting distal branches in SLM. These anatomical features suggest that CA3PC dendrites may act as parallel integrative compartments.

In line with the cellular heterogeneity discussed earlier in Chapter 1.4, CA3 is not a homogeneous network but consists of functionally distinct subregions (CA3a, b, c) that differ in their connectivity, intrinsic excitability, and computational roles. (Lee et al., 2015; Sun et al., 2017). Cells in proximal CA3 (CA3c) receive strong MF input and are thought to contribute to pattern separation, which helps distinguish similar memories. In contrast, distal CA3 (CA3a-b) has more recurrent connections and is more involved in pattern completion Despite this heterogeneity, it remains unknown whether all CA3PCs can generate dendritic Ca^{2+} spikes and long-lasting CSBs, or whether these properties are restricted to specific subpopulations.

Given the extensive topographic variability in morphology, connectivity, and intrinsic properties, it is likely that the mechanisms underlying CSB generation are similarly heterogeneous across the CA3 network.

2. OBJECTIVES

The hippocampal CA3 region plays a critical role in memory encoding and retrieval. While Ca^{2+} spikes are well characterized in CA1PCs, their properties in CA3PCs remain less understood. Although early electrophysiological studies suggested their presence (Lazarewicz et al., 2002; Nuñez and Buño, 1992; Wong et al., 1979), their specific role and characteristics in CA3PCs require further exploration. This raises the question: Do Ca^{2+} spikes universally serve the same function across hippocampal PC types, or do their properties vary, enabling different forms of input-output transformations and computations?

The aim of this dissertation is to unravel the properties, biophysical mechanisms and functional significance of dendritic Ca^{2+} spikes and CSBs in CA3PCs by addressing the following questions:

1. What are the intrinsic mechanisms of CSB generation in CA3PCs?
2. What are the biophysical properties and roles of dendritic Ca^{2+} spikes in CA3PCs?
3. How heterogeneous are these properties and functions across CA3PCs?
4. How are they regulated by cholinergic neuromodulation?

By addressing these questions, the dissertation will contribute to a deeper understanding of the mechanisms underlying dendritic integration, burst generation, and neuromodulation in CA3PCs, providing new insights into their role in hippocampal memory processes.

3. METHODS

3.1. **Contributions**

The majority of the somatic patch-clamp recordings, Ca^{2+} imaging and pharmacological experiments were done by me, in collaboration with Judit Makara, Snezana Raus Balind, Mahboubeh Ahmadi, Bela Erlinghagen and Mátyás Irás. Dendritic patch-clamp experiments were carried out by Ádám Magó (**Fig. 7**), Judit Makara and me, with Ádám Magó also performing dual recording. Morphological reconstructions and Sholl analysis were performed together with Zsófia Varga Németh. All optogenetic experiments were conducted by me. Judit Herédi made confocal and STED images from biocytin-filled cells (**Fig. 19**). Data analysis and clustering were supported by custom scripts developed by Balázs Lükő and Balázs Ujfalussy.

3.2. Hippocampal slice preparation

Adult (7 to 12-week-old) male Wistar rats, male FVB/AntJ mice, and male and female ChAT-Cre/Ai32 transgenic mice were used to prepare acute slices from the middle to dorsal part of the hippocampus of both hemispheres (400-µm-thick transverse slices in rats and 300-µm-thick coronal or transverse slices in mice) as described (Kis et al., 2024; Magó et al., 2021; Makara and Magee, 2013; Raus Balind et al., 2019), according to methods approved by the Animal Care and Use Committee of the Institute of Experimental Medicine, and in accordance with the Institutional Ethical Codex, Hungarian Act of Animal Care and Experimentation 40/2013 (II.14), and European Union guidelines (86/609/EEC/2 and 2010/63/EU Directives). To obtain expression of Channelrhodopsin-2 (ChR2) in cholinergic fibers for optogenetic experiments, we crossbred ChAT-Cre (The Jackson Laboratory, RRID: IMSR_JAX:006410) and Ai32 (The Jackson Laboratory, RRID: IMSR_JAX:024109) mice.

Animals were deeply anesthetized with 5% isoflurane and quickly perfused through the heart with ice-cold cutting solution containing (in mM): sucrose 220, $NaHCO_3$ 28, KCl 2.5, NaH_2PO_4 1.25, $CaCl_2$ 0.5, $MgCl_2$ 7, glucose 7, Na-pyruvate 3, and ascorbic acid 1, saturated with 95 % O_2 and 5 % CO_2. The brain was quickly removed, and slices were prepared in cutting solution using a vibratome (VT1000S, Leica, Leica Biosystems

GmbH, Nussloch, Germany). Slices were incubated in a submerged holding chamber in ACSF at 35 °C for 30 min and then stored in the same chamber at room temperature.

3.3. Patch-clamp recordings

Slices were transferred to a custom-made submerged recording chamber under the microscope where experiments were performed at 32-34 °C in ACSF containing (in mM): NaCl 125, KCl 3, $NaHCO_3$ 25, NaH_2PO_4 1.25, $CaCl_2$ 1.3, $MgCl_2$ 1, glucose 25, Na-pyruvate 3, and ascorbic acid 1, saturated with 95 % O_2 and 5 % CO_2. Cells were visualized using Zeiss Axio Examiner or Olympus BX-61 epifluorescent microscope under infrared illumination and water immersion lens (63X or 60X during recording, 20X or 10X for overview z-stacks, Zeiss or Olympus). In every slice, we selected a region within CA3 where the apical trunks of most neurons were oriented slightly downwards to access neurons with mostly preserved dendritic arborization (directed into the tissue), and we targeted somata located >50 µm deep in the slice. Somatic (2–6 MΩ) and/or dendritic (6–10 MΩ) patch pipettes were filled with a solution containing (in mM): K-gluconate 134, KCl 6, HEPES 10, NaCl 4, Mg_2ATP 4, $Tris_2GTP$ 0.3, phosphocreatine 14 (pH = 7.25), typically complemented with 50 µM Alexa Fluor 594 and 100 µM Oregon Green BAPTA-1 (OGB-1) or Oregon Green BAPTA-6 (OGB-6) (all fluorescent dyes from Invitrogen-Molecular Probes). Electrophysiological results were similar using OGB-1 and OGB-6F and therefore results obtained with different Ca^{2+}-sensitive dyes were pooled.

Current-clamp whole-cell recordings were performed using BVC-700 amplifiers (Dagan, Minneapolis, MN) in the active "bridge" mode, filtered at 3 kHz and digitized at 50 kHz. Series resistance was typically between 15-25 MΩ in somatic and 25–60 MΩ in dendritic recordings, frequently checked and compensated with bridge balance and capacitance compensation; recordings were terminated when somatic series resistance exceeded 30 MΩ. Only CA3PCs with somatic V_m more negative than -60 mV after break-in were used for experiments. Cells were usually kept at -68 – -72 mV with appropriate constant current injection. After establishing the somatic whole-cell current clamp configuration, cells were loaded for >20 min to visualize the dendritic tree by two-photon imaging. Application of carbachol usually led to ~2 – 6 mV depolarization, which was compensated with hyperpolarizing current to keep V_m constant.

At dual soma-dendrite recordings, a dendrite was patched first, and after establishing the dendritic whole-cell configuration, cells were loaded for >10 minutes to visualize the soma for targeted patching. Intracellular solution and recording settings were the same at the dendrite as at the soma.

In all recorded CA3 neurons, dendrites were carefully inspected for thorny excrescences in proximal apical parent dendrites and small spines on more distal dendritic branches, and for verifying that no main proximal apical trunk was cut.

3.4. Two-photon imaging and uncaging

Dual galvanometer based two-photon (2P) scanning systems (Bruker, former Prairie Technologies, Middleton, WI, USA) were used to image the patched neurons and to uncage glutamate at individual dendritic spines. Two ultrafast pulsed laser beams (Chameleon Ultra II; Coherent, Auburn, CA) were used: one laser at 920 or 860 nm for imaging OGB dyes and Alexa Fluor 594, respectively, and the other laser tuned to 720 nm to photolyze MNI-caged-L-glutamate (Tocris). The intensity of the laser beam was controlled with electro-optical modulators (model 350-80, Conoptics, Danbury, CT). Linescan Ca^{2+} measurements were performed with 8 μs dwell time at ~200 to 300 Hz. MNI-caged-L-glutamate (10 mM in ACSF) was applied through a puffer pipette with a ~20-30-μm-diameter, downward-tilted aperture above the slice using pneumatic ejection system (PDES-02TX, NPI, Tamm, Germany).

2P glutamate uncaging (2PGU) was performed at a clustered set of 20 spines on the patched apical trunk using 0.5 ms uncaging duration at each spine with 0.1 ms intervals between synapses, repeated five times at 40 Hz (i.e., gamma burst stimulus). Uncaging laser power was adjusted to yield compound voltage responses near the threshold of regenerative events (bAPs or dendritic spikes), preferably so that both subthreshold and suprathreshold responses could be evoked.

3.5. Optogenetic stimulation of cholinergic axons

Optogenetics enables precise control of neuronal activity using genetically encoded light-sensitive proteins (opsins), such as ChR2, a blue-light-activated cation channel that induces neuronal depolarization and action potential firing (Duebel et al., 2015; Häusser, 2014). This technique provides high temporal precision and cell-type specificity, making it an invaluable tool for investigating neural circuit function.

Acute slices were prepared from ChAT-Cre/Ai32 mice as described above. Cholinergic axons were activated using pulsed train illumination (100-ms pulses with 100-ms intervals, applied for 10 s (Hunt et al., 2018) through the 60X objective with 447-nm laser light. While we cannot precisely mimic the firing dynamics of cholinergic axons projecting to the hippocampus, elevated acetylcholine release on a similar second-long time scale was observed in the hippocampus of awake behaving animals (Lovett-Barron et al., 2014; Zhang et al., 2021). 1-s I_{inj} steps were applied either without preceding illumination (control) or during the end of the illumination train. CSB rate and duration were measured at the threshold I_{inj} level eliciting CSBs under control conditions (3 cells produced no CSBs with up to 1 nA I_{inj}).

3.6. Chemicals

Tetrodotoxin (TTX, Tocris or Alomone Labs), guangxitoxin (GxTX, Tocris), XE991 dihydrochloride (XE991, Tocris), iberiotoxin (IbTx, Tocris), apamin (Ap, Tocris), carbachol (CCh, Tocris), hexamethonium bromide (Tocris), D-AP5 (Tocris), SNX-482 (Peptides International), ω-Conotoxin MVIIC (CTX, Alomone Labs), dendrotoxin-I (DTX, Alomone Labs), AmmTx3 (Alomone Labs) and ipratropium bromide (Sigma-Aldrich) were prepared in stock solution in distilled water. For peptide toxins the solvent also contained 0.1% BSA (Sigma- Aldrich). Nimodipine (Tocris), nifedipine (Tocris) and TTA-P2 (Alomone Labs) were dissolved in DMSO.

Stock solutions were stored at -20°C and dissolved to final concentration (in at least 1:1000 dilution) into bubbled ACSF before application. In experiments with peptide toxins, the perfusion tubes were pretreated with 0.1% BSA (dissolved in ACSF) to prevent the toxin from binding to the wall.

TTX at 1 μM concentration is widely used to block VGNCs (Kaneda et al., 1989; Madeja, 2000) and it eliminated APs in our experiments. Ca^{2+} channel blockers at the concentration applied in this study are generally considered selective to the targeted Ca^{2+} channel subtype. TTA-P2 inhibits primarily T-type Ca^{2+} channels (Choe et al., 2011; Dreyfus et al., 2010; Mishra and Hermsmeyer, 1994), SNX-482 specifically blocks R-type Ca^{2+} channels (Newcomb et al., 1998), CTX inhibits N-type and P/Q-type Ca^{2+} channels (Hillyard et al., 1992), and nimodipine and nifedipine are antagonists of L-type Ca^{2+} channels (Furukawa et al., 2005, 1999). Although SNX-482 has been reported to also inhibit Kv4 potassium channels (Kimm and Bean, 2014), we did not observe an effect

of SNX-482 on the halfwidth of Ca^{2+} spikes, arguing against a confounding effect on K^+ channels. The concentration of carbachol we applied (2 μM) is expected to activate acetylcholine receptors in the physiological range: the concentration of acetylcholine during awake exploration or memory tasks has been estimated to rise to the ~0.1-1 μM range (Kametani and Kawamura, 1990; McIntyre et al., 2003; Mineur and Picciotto, 2023; Nail-Boucherie et al., 2000; Pepeu and Giovannini, 2004), and CCh has a several-fold lower affinity for mAChRs compared to acetylcholine (Kellar et al., 1985; Yamamura and Snyder, 1974).

3.7. Data analysis

Analysis of voltage and Ca^{2+} recordings was performed using custom-written scripts in IgorPro (WaveMetrics, Lake Oswego, OR) and Python.

3.7.1. Analysis of CSBs and Ca^{2+} spike properties

CSBs evoked by I_{inj} were identified based on the combination of the following properties: (1) ≥2 high-frequency APs with progressively decreasing peak amplitude, preceded by at least one additional simple AP in the given I_{inj} pulse, (2) riding on an underlying slow ADP that followed the first AP of the CSB, and (3) typically accompanied by a Ca^{2+} signal in a distal apical dendrite.

CSB rate (i.e. propensity) was calculated by dividing the number of I_{inj} steps (100-ms-long steps of 300–600 pA) displaying CSB with the total number of I_{inj} steps (5 per trace, 5-10 repetitions). The duration of full-blown CSBs evoked by I_{inj} was measured using the 1-s-long I_{inj} steps at or slightly above the lowest current evoking CSBs. CSB duration was calculated as the time difference between the peak of the last simple ('reference') AP before the sudden drop in the AP amplitude, which marks the beginning of the CSB and the peak of the last AP in the CSB either (i) with reduced amplitude compared to reference AP or (ii) fired <50 ms after the preceding AP, whichever comes first. The AP threshold was measured as the voltage value where dV/dt exceeded 20 V/s.

The properties of pharmacologically isolated Ca^{2+} spikes were determined after >10 min bath application of Na^+ channel blocker tetrodotoxin (TTX), using 1-s-long step or ramp I_{inj}. Typically, a range of I_{inj} levels were tested with multiple repetitions, including subthreshold and different suprathreshold values that evoked the Ca^{2+} spike with different

latencies. We aimed to set the I_{inj} to the level where the Ca^{2+} spike was evoked at the approximate middle of the step.

To analyze Ca^{2+} spike properties measured in TTX at the soma (illustrated in **Fig. 16A, B**), traces were smoothed using the built-in binomial (Gaussian) smoothing algorithm (num=10000) of IgorPro. dV/dt_{max} and dV/dt_{min} were determined as the maximum and minimum of the derivative of this smoothed trace, respectively. We defined the parameter dV/d_{total} as the full dV/dt range (dV/dt_{max} minus dV/dt_{min}). Spike threshold was measured as the voltage where dV/dt crossed an adaptive threshold (20% of the maximum of the first spike-associated dV/dt peak with an upper bound of 0.25 V/s). Amplitude was measured as voltage peak minus threshold; halfwidth was calculated as the time difference at half maximum amplitude. The number of spike peaks was calculated using a custom Python algorithm where we take all the local maxima and discard those which are not separated by a local minimum that is at least 3 mV smaller than maxima on either side. The above parameters were measured on multiple (typically 5) repetitions and averaged to represent Ca^{2+} spike properties of a cell. In some of the experiments testing the effect of carbachol on Ca^{2+} spikes, the slow repolarization after the Ca^{2+} spike prevented the precise measurement of the halfwidth; in these cases we considered halfwidth to be 0.3 s.

In a small subset of CA3PCs, the step I_{inj} invariably evoked the Ca^{2+} spikes at the beginning of the step (<100 ms) where kinetic parameters could not be adequately measured. These cells were either excluded from detailed Ca^{2+} spike analysis, or alternatively we applied a ramp protocol using linearly increasing current for 1 second that allowed extraction of the parameters.

3.7.2. Analysis of Ca^{2+} signals

Ca^{2+} signals are expressed as $\Delta F/F0 = (F(t)-F0)/F0$, where F(t) is fluorescence at a given time point and F0 is the mean fluorescence during 50 ms preceding the depolarizing I_{inj}. To measure Ca^{2+} spike associated Ca^{2+} signal amplitude, traces were aligned to the initial rise (~300 mV/s dV/dt value) of the Ca^{2+} spike, and we calculated the difference between the maximum average of 5 consecutive points following the spike and the average of the 20-50 ms period preceding the spike. Ca^{2+} traces and some of the electrophysiological traces are presented with slight smoothing (binomial, num=1).

3.8. Clustering

Clustering of Ca^{2+} spikes measured in TTX was performed with the Ward hierarchical clustering method, using the sklearn.cluster module in Python. For each individual cell, the z-score normalized dV/dt_{total}, $\log_{10}$(halfwidth), and number of peaks were considered.

3.9. Morphological analysis

Dendritic morphological and distance measurements were performed using ImageJ (NIH, Bethesda, MD) on stacked 2P images of dye-loaded (Alexa Fluor 594) neurons, collected at the end of the experiment. The analysis was done blind to the electrophysiological cluster identity of the cells.

Primary apical trunk length was measured on the 2D z-stacks by manually drawing a segmented line from the apical edge of the soma to the first main bifurcation. A cell was considered to have a single primary trunk if the initial thick apical trunk was at least 10 μm long before the first branchpoint. In cells with multiple primary trunks the length of all primary trunks was averaged as a measure of primary trunk length.

Radial soma position was determined for a subset of cells where 2P Dodt contrast images were also taken and was measured as the Euclidean distance of the soma center from the border of str. pyramidale and str. lucidum.

The relative proximodistal position was calculated based on measurements on low-magnification fluorescent images of the whole hippocampus. The distal border of CA3a (from CA2) was considered to be located at 200 μm from the sudden widening of the pyramidal cell layer (i.e., CA1-CA2 border). For separate analysis of proximal (relative position 0-0.3) and distal (relative position: 0.4-1) CA3PCs, cells in the transition zone (relative position between 0.3-0.4) were not included (Kis et al., 2024). Proximal CA3 approximately corresponds to CA3c, and distal CA3 roughly corresponds to CA3a and CA3b (Raus Balind et al., 2019; Sun et al., 2017).

In a subset of experiments, morphological parameters of the dendritic tree were extracted from semiautomated analysis of fully reconstructed CA3PCs with the most complete dendritic arbor using Vaa3D software (Peng et al., 2014, 2010), followed by visual inspection, and manual corrections where necessary.

To characterize the complexity of the dendritic arbor, Sholl analysis was performed on the 2D maximal intensity projections of the z-stacks of the recorded CA3PCs. In Raus

Balind et al. (2019) the analysis was done on the whole dendritic tree, whereas in Kis et al. (2024) Sholl analysis was performed on the apical dendritic arbor in a subset of the recorded CA3PCs in which the apical dendritic arborization was fully conserved and well visualized in the 2P z-stack until at least 200 μm apical distance from the soma. We measured the number of apical dendritic intersections along concentric circles with 50, 100, 150 and 200 μm radius, centered at the soma.

3.10. Statistical analysis

Statistical analysis was performed with the Statistica software (Statsoft, Tulsa, OK). Where possible, nonparametric tests (Wilcoxon test for two paired groups or for one sample compared to median=1, Mann–Whitney test for two unpaired groups, Kruskal-Wallis test with post hoc multiple comparisons for 3 unpaired groups, Friedman test for one-way repeated measures, Spearman correlation) were used, which do not make assumptions about the distribution of data. Mixed ANOVA with post hoc Tukey's test was used for Sholl analysis. The specific test used for a given analysis is indicated in the text. All statistical tests were two-tailed. Differences were considered significant when $P < 0.05$. In all figures, *$P < 0.05$; **$P < 0.01$; ***$P < 0.001$.

4. RESULTS

4.1. Diverse CSB generation in hippocampal CA3PCs

To explore the role of distal apical dendrites in CSB generation in CA3PCs, neurons were loaded with a Ca^{2+}-sensitive fluorescent dye (either OGB-1 or OGB-6, 100 µM) and a Ca^{2+}-insensitive marker (Alexa Fluor 594, 50 µM) via somatic patch pipettes (**Fig. 3A**). To assess CSB generation, we applied somatic depolarizing current injections (I_{inj}, five 100-ms-long pulses of 300–600 pA with 80.55-ms-long interpulse intervals) from a baseline V_m of approximately −70 mV (**Fig. 3B**).

Using this protocol, in many CA3PCs we readily observed CSBs, characterized as bursts of ≥ 2 APs with progressively smaller amplitudes and longer durations riding on a prolonged ADP of variable duration (~20–70 ms), that were distinct from simple APs. CSB were accompanied by time-locked Ca^{2+} responses detected even in the most distal apical dendrites of the SLM, occurring in an all-or-none fashion (**Fig. 3C**). To quantify the propensity of CA3PCs to generate CSBs, we calculated the CSB rate, defined as the ratio of pulses with CSBs to the total number of pulses. The results demonstrated that the CSB rate increased with stronger I_{inj}. Within the pulse series, CSBs were most commonly triggered by the first pulse but also occurred on subsequent pulses, especially with higher depolarizing currents (**Fig. 3E, F**). When comparing CA3PCs with CA1PCs, we observed that CSB propensity was significantly higher in CA3PCs than in CA1PCs under comparable conditions (**Fig. 3F**).

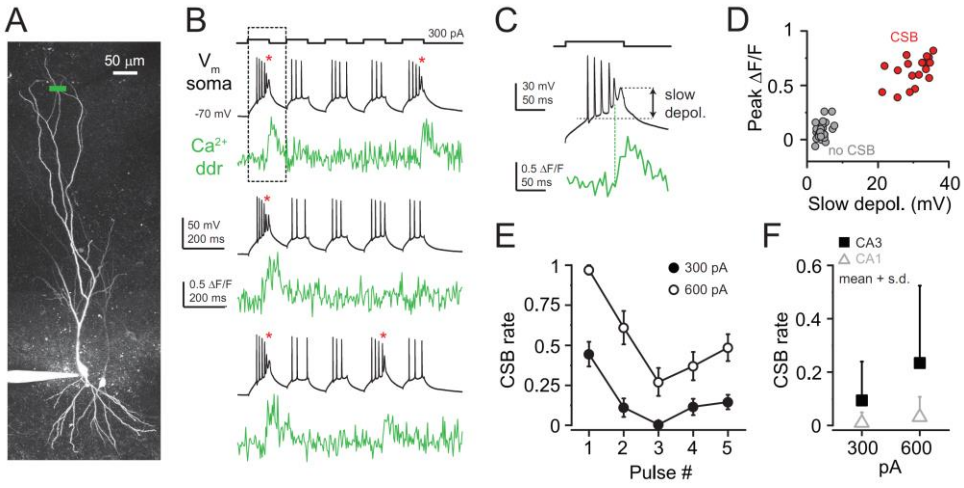

Figure 3. Characterization of CSBs and associated dendritic Ca^{2+} signals in CA3PCs. ***(A)*** *Z-stack of a CA3PCs loaded with 50 µM Alexa594 and 100 µM OGB-6F. Ca^{2+}*

imaging line is indicated in green. ***(B)*** *Example traces showing simultaneous somatic current-clamp recordings and corresponding dendritic (ddr)* Ca^{2+} *signals from the cell shown in (A). CSBs are marked by red asterisks. The* I_{inj} *protocol is shown above the traces.* ***(C)*** *Zoomed-in view of the dashed region from (B), illustrating the slow depolarization underlying CSB and the time-locked dendritic* Ca^{2+} *signal.* ***(D)*** *Results of the total 50 pulses of 10 traces recorded from the cell shown in (A-C).* ***(E)*** *CSB rate across different pulses in a train of* I_{inj} *in a set of 20 CA3PCs that generated CSBs in response to 300 pA* I_{inj}*. Data points and whiskers represent mean ± SEM* ***(F)*** *Comparison of CSB rates at 300 pA and 600 pA* I_{inj} *between CA3PCs (n = 118 and 117 cells, respectively) and CA1PCs (n = 26 cells). Data are shown as mean ± SD (Raus Balind et al., 2019).*

This elevated CSB propensity aligns with the distinctive dendritic architecture and input-output dynamics of CA3PCs, which often serve as integrative hubs in hippocampal memory circuits.

Interestingly, heterogeneity was evident among individual CA3PCs, which we categorized into three groups based on their CSB propensity: 1) high bursting cells (CSB_H), which exhibited CSBs at lower I_{inj} thresholds (300 pA); 2) low bursting cells (CSB_L), which required stronger I_{inj} (400–600 pA) for CSB generation, and 3) regular spiking cells (RS), which did not generate CSBs, even at higher I_{inj} levels (no CSB at 600 pA) (**Fig 4. A-C**).

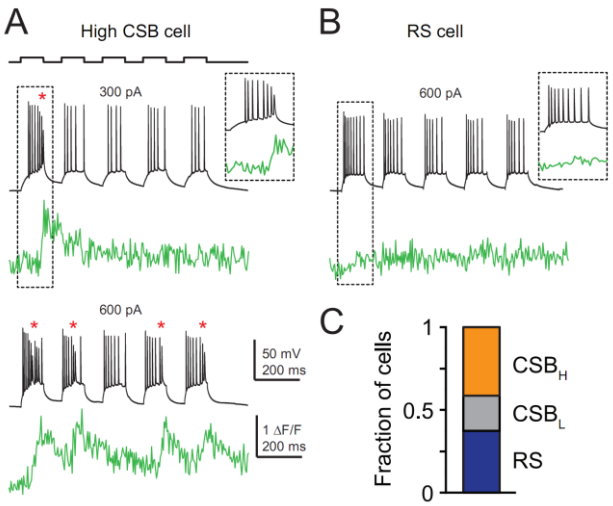

Figure 4. Diversity of CSB propensity among CA3PCs. ***(A)*** *Representative voltage traces and distal dendritic* Ca^{2+} *signals recorded from a* CSB_H *cell in response to*

repetitive 100-ms-long somatic I_{inj} (300 and 600 pA). The I_{inj} protocol is shown above. Red asterisks mark the CSBs. The region within the dashed box is magnified in the inset to highlight the detailed waveform. ***(B)*** *RS cell upon 600 pA. Note the absence of CSBs.* ***(C)*** *Fraction of CSB_H, CSB_L, and RS cells in the whole recorded dataset (Raus Balind et al., 2019).*

We first examined whether synaptic or rather intrinsic mechanisms underlie CSB generation. Blocking AMPA/NMDA glutamate receptors (**Fig. 5A**, n = 10, p = 0.753, Wilcoxon test) or $GABA_A$/$GABA_B$ receptors (**Fig. 5B**, n = 11, p = 0.892, Wilcoxon test) did not affect CSB rate, indicating that CSBs are primarily driven by intrinsic cellular properties. Indeed, blockade of APs by TTX in CSB cells uncovered an underlying depolarizing component that was eliminated by the VGCC blocker cadmium (Cd^{2+}, 100–200 µM, **Fig. 5C, D**, n = 7, p = 0.017, Wilcoxon test), suggesting the role of VGCCs in CSB generation.

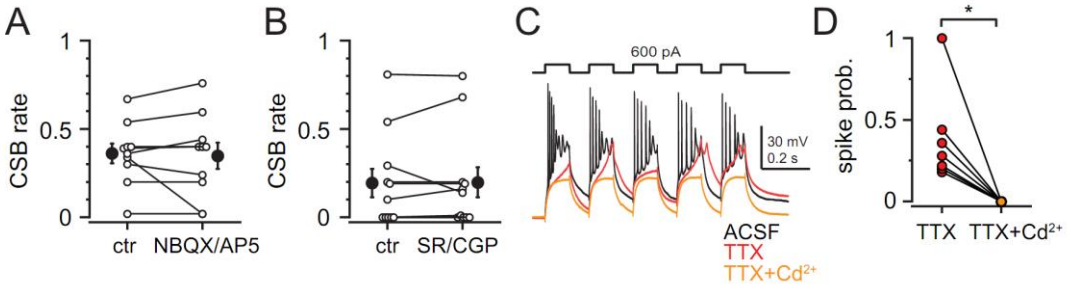

Figure 5*.* ***Intrinsic mechanisms and VGCC dependence of CSBs.*** ***(A)*** *Effect of AMPA and NMDA receptor blockade on CSB generation. CSB rates were measured at 300 pA and 600 pA I_{inj} before and after the application of 10 µM NBQX and 50 µM D-AP5.* ***(B)*** *Effect of $GABA_A$/$GABA_B$ receptor inhibitors (2 µM SR95531 and 2 µM CGP55845) on CSB rate at the same I_{inj}.* ***(C)*** *Representative voltage traces from a CSB_H cell under three conditions: control (black), after the application of 1 µM TTX (red), and following subsequent addition of 200 µM Cd^{2+} (orange). Regenerative responses in TTX are eliminated by Cd^{2+}.* ***(D)*** *Summary illustrating the effect of Cd^{2+} on Ca^{2+} spikes recorded (Raus Balind et al., 2019).*

We next aimed to identify the potential anatomical factors associated with the vast heterogeneity in CSB generation observed among different CA3PCs. Since several properties of CA3PCs vary according to their topographic location, we investigated the relationship between CSB propensity and soma position in dorsal CA3PCs by categorizing cells based on their proximodistal (three regions: CA3a, CA3b, CA3c (equal one-thirds of the full proximodistal length (Sun et al., 2017)) and radial (superficial: soma within str. pyramidale or deep: soma in str. oriens or on the pyramidale-oriens border) locations (**Fig. 6A, B**).

Analysis (two-way ANOVA, using data with 600 pA I_{inj} in deep and superficial CA3a and CA3c cells ($p = 0.027$ for proximodistal axis, $p = 0.173$ for radial axis, $p = 0.025$ for interaction)) revealed a complex dependency of CSB propensity on these parameters. CSB rates increased along the proximodistal axis (CA3c to CA3a) ($p = 0.027$, **Fig. 6C-F**), while differences between superficial and deep cells were significant only in CA3a, where deep cells exhibited higher CSB rates ($p = 0.065$, Tukey's post hoc test) and had higher proportions of CSB cells ($p = 0.034$, χ^2 test), whereas in CA3c there was no significant difference (**Fig. 6C**, CSB rate: $p = 0.909$, Tukey's test; ratio of CSB cells, $p = 0.424$, χ^2 test). Basic electrophysiological properties, such as input resistance (R_{in}) and V_m, did not fully explain these patterns (although R_{in} showed an increase in the a-to-c and deep-to-superficial direction, **Fig. 6D, E**, two-way ANOVA, $p = 0.004$ for proximo-distal axis, $p = 0.005$ for radial axis, $p = 0.028$ for interaction).

We next examined whether variations in dendritic morphology are related to CSB propensity with the help of 3D reconstructions (Vaa3D) and Sholl analysis of dendritic arborization. We compared several dendritic parameters of CA3PCs of the two extreme electrophysiological phenotypes: CSB_H and RS cells, and analyzed them separately within CA3a and CA3c without distinction by radial position (**Fig. 6G-J**). The primary apical dendrite was longer in CSB_H cells compared to RS cells (two-way ANOVA, $p < 0.001$ for subregion, $p = 0.082$ for firing type, $p = 0.011$ for interaction, significant paired comparisons by post hoc Tukey test are indicated in **Fig. 6I**). This is consistent with dependence of CSB rate on soma position (**Fig. 6C**), because the primary apical trunk of deep CA3PCs runs longer to reach str. lucidum where it typically branches.

In a subset of fully reconstructed CA3PCs we analyzed dendritic arbor complexity, which exhibited significant variability across all cell groups. Sholl analysis highlighted some

previously reported differences between PCs in CA3a and CA3c (**Fig. 6H**). However, no major differences were observed in total dendritic length, branchpoint numbers, or the

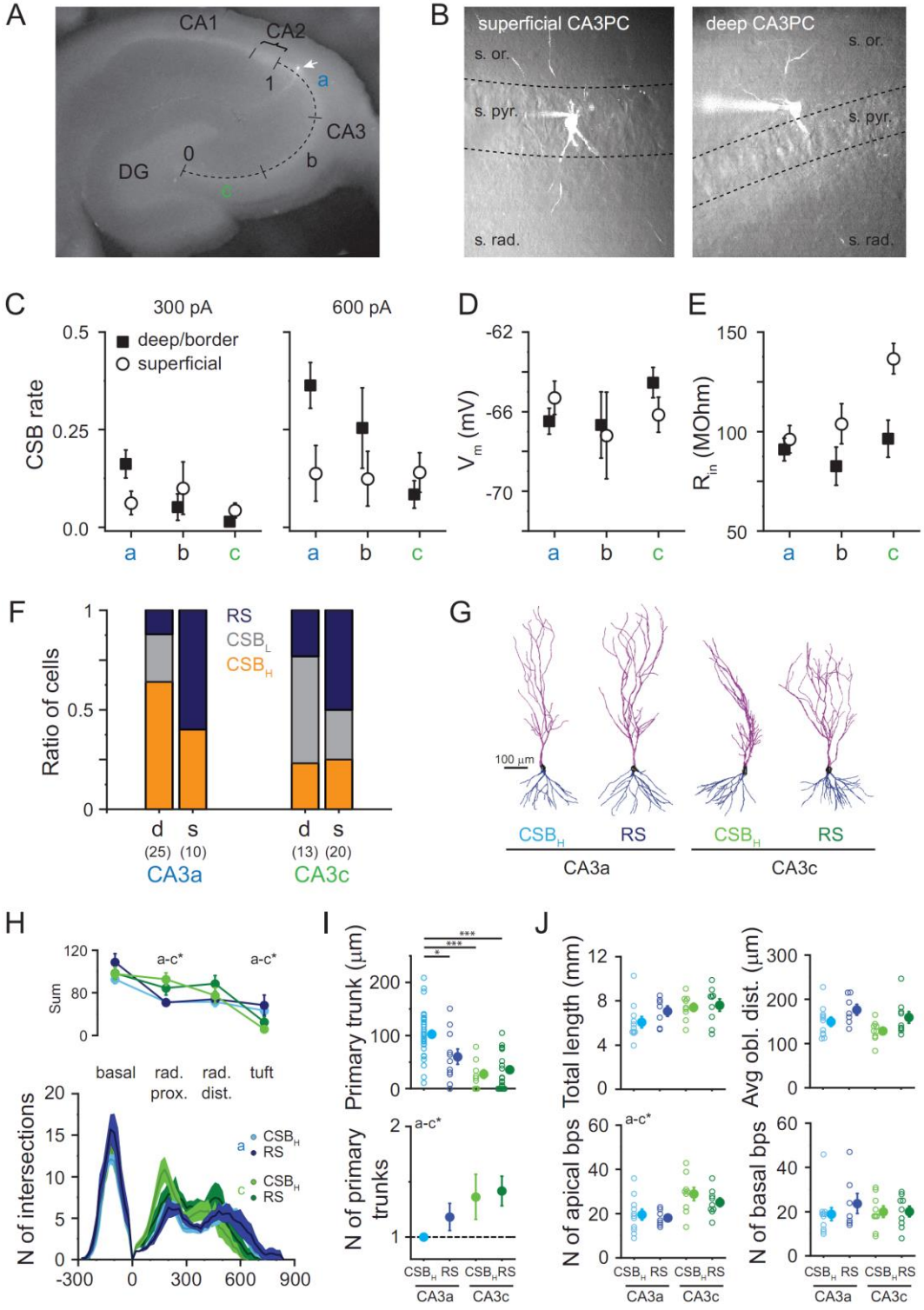

Figure 6. Spatial and morphological factors influencing CSB propensity in CA3PCs. ***(A)*** *Definition of CA3 subregions along the proximodistal CA3a, CA3b, CA3c.* ***(B)***

Definition of radial cell groups based on soma location. Superficial cells had their somas located within the str. pyramidale, while deep/border cells had somas positioned on or beyond the border between str. pyramidale and str. oriens. ***(C)*** *CSB propensity across CA3PC subgroups. The graph shows the propensity for CSB generation in response to 300 pA (left) and 600 pA (right)* I_{inj} *series across the six defined CA3PC groups (subregion × radial position). Symbols and error bars represent mean ± SEM.* ***(D, E)*** V_m *and* R_{in} *measurements across the six CA3PC groups (mean ± SEM).* ***(F)*** *Ratio of* CSB_H*,* CSB_L*, and RS in the CA3a and CA3c regions. Number of deep and superficial cells, respectively: CA3a: 25/10, CA3c: 13/20.* ***(G)*** *Representative morphologies of CA3PCs from CA3a and CA3c subregions.* ***(H)*** *Sholl analysis comparing dendritic arborization patterns of* CSB_H *and RS cells in CA3a and CA3c. Upper panel: sum of dendritic intersections in str. oriens, proximal str. radiatum (100–280 μm), distal str. radiatum (300–500 μm) and SLM (>520 μm). Symbols and error bars represent mean ± SEM. The branching profile was different between CA3a and CA3c PCs, but did not depend on CSB propensity (two-way repeated measures ANOVA,* $p < 0.001$ *for subregion,* $p = 0.310$ *for bursting phenotype,* $p = 0.409$ *for interaction). Lower panel: branching profiles as mean lines ± SEM shadings.* ***(I)*** *Primary apical trunk length and number, measured from 2P image stacks (CA3a* CSB_H*:* $n = 34$*; CA3a RS:* $n = 11$*; CA3c* CSB_H*:* $n = 11$*; CA3c RS:* $n = 24$*).* ***(J)*** *Morphometric analysis of dendritic architecture, including total dendritic length, average distance of oblique dendrites from the soma, and branch point numbers across the analyzed groups (CA3a* CSB_H*:* $n = 11$*; CA3a RS:* $n = 7$*; CA3c* CSB_H*:* $n = 9$*; CA3c RS:* $n = 9$*). Statistical comparisons were performed using two-way ANOVA with Holm-Bonferroni correction. Filled symbols and error bars in (I-J) represent mean ± SEM.* $*p < 0.05$*;* $***p < 0.001$ *(Raus Balind et al., 2019).*

distance of oblique dendrites from the soma between the two electrophysiological phenotypes (**Fig. 6J**), although there was a trend for apical obliques to branch from the trunk more distally in RS cells. Overall, while primary dendrite length appeared to be a reliable predictor for bursting activity in distal CA3 (Bilkey and Schwartzkroin, 1990; Hunt et al., 2018), dendritic morphology generally did not correlate strongly with CSB rate across the entire CA3 region.

Based on the previous study (Hunt et al., 2018), that suggested the presence of 'athorny' CA3PCs in deeper distal layers with bursting phenotype, we examined the proximal apical dendrites of our CSB_H cells located in deep CA3a-b using high-magnification imaging. Our analysis revealed that all examined CSB_H cells (n = 11) displayed at least one, and often several, large, lobular, complex spine-like postsynaptic structures on first- or higher-order dendritic trunks in str. lucidum. This confirms that these cells were not 'athorny' CA3 cells. Thus, our findings indicate that the majority of classical thorny CA3PCs in deep distal CA3 exhibit a CSB phenotype.

4.2. Distinct dendritic Ca^{2+} spike forms

To better understand the dendritic electrophysiological mechanisms underlying the diverse firing patterns observed in CA3PCs, we focused on dendritic Ca^{2+} spikes, which play a central role in the generation of CSBs described earlier. We performed dendritic and dual patch-clamp recordings combined with 2P Ca^{2+} imaging (**Fig. 7A**). These recordings targeted higher-order dendritic trunks at distances of approximately 165–400 μm from the soma. Using 1-s-long depolarizing I_{inj} via either somatic or dendritic electrodes, we aimed to characterize the distinct properties of dendritic Ca^{2+} spikes and their contributions to somatic outputs.

Our experiments revealed two distinct types of dendritic Ca^{2+} spikes (beside other regenerative events including bAPs and Na^+ spikes): ADP-type spikes (**Fig. 7B, C**) and dendritically initiated (DI) spikes (**Fig. 7D, E**). ADP spikes followed bAPs and often triggered bursts of somatic action potentials, whereas DI spikes were fast, locally generated regenerative events that were initiated independently of bAPs.

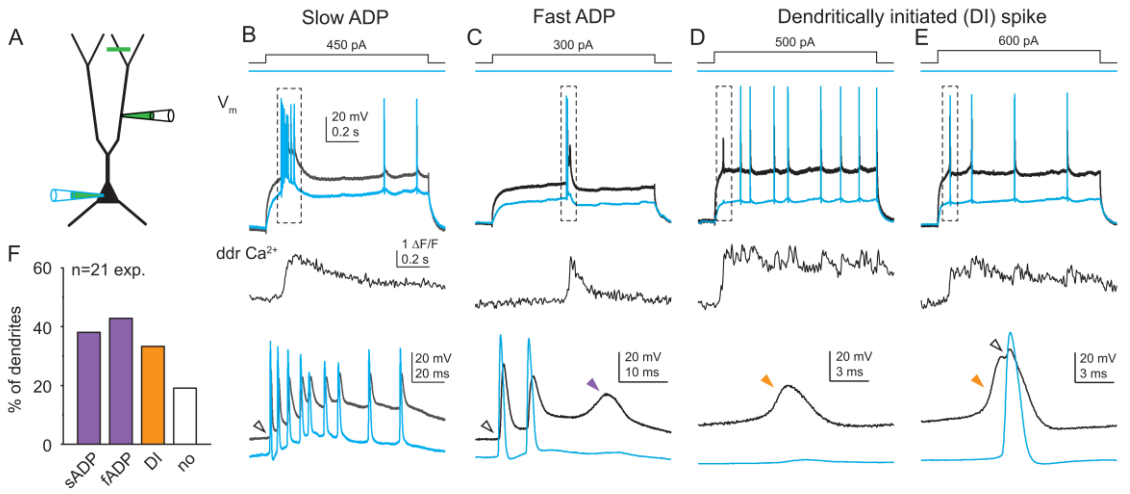

Figure 7. Diversity of dendritic Ca^{2+} spike forms in dual soma-dendrite recordings from CA3PCs. ***(A)*** *Schematic of a soma-dendrite dual patch recording configuration. The green line indicates a typical Ca^{2+} imaging site located distal to the dendritic patch electrode.* ***(B)*** *Example recording of a slow ADP. The top panel shows simultaneous dendritic (black) and somatic (blue) voltage responses to dendritic I_{inj}. The middle panel displays the corresponding distal dendritic Ca^{2+} signal. The dashed box highlights an event magnified in the bottom panel, showing a prolonged, sustained ADP that generates a gradual depolarization larger in the dendrite than in the soma. The open arrowhead marks the characteristic sharp inflection (kink) of the initiating bAP.* ***(C)*** *Example recording of a fast ADP. Panel ordering is the same as (B). The purple arrowhead on the bottom panel marks the fast ADP event.* ***(D-E)*** *Representative recordings of DI spikes. Panels follow the same structure as in (B, C).* ***(E)*** *The DI spike can evoke a consecutive somatic AP. The open arrowhead marks the AP kink, while orange arrowheads indicate the DI spikes. Note the differences in time scales across the various Ca^{2+} spike forms.* ***(F)*** *Proportional distribution of Ca^{2+} spike types across recorded dendrites (n = 21) from dual soma-dendrite patch recordings (Magó et al., 2021). Dual patch-clamp recordings were done by Ádám Magó.*

We further characterized the properties of these spikes using I_{inj} in a larger set of single-site dendritic recordings (n = 69, at 159–450 µm from soma, mean ± SEM: 272 ± 8 µm). Replicating the findings of dual recordings, 1-s-long dendritic I_{inj} steps elicited different types of putative Ca^{2+} spikes, that is, ADPs and/or DI spikes in the majority

(~85%) of individual dendrites (**Fig. 8A-D**). Within the tested I_{inj} range (300–600 pA), ADP and DI spikes were observed in 56% and 53% of dendrites, respectively, with 24% exhibiting both types (**Fig. 8E**, pooled dual- and single-site recordings, n = 70). The dominant spike type often depended on the magnitude of the current injection, with ADPs typically occurring at lower I_{inj} levels and DI spikes requiring stronger depolarization (**Fig. 8C, E**). In some cases, both spike types occurred intermingled within the same depolarizing trace (**Fig. 8D**).

The role of VGCCs in generating these spikes was confirmed by pharmacological experiments. Bath application of 200 µM Ni^{2+}, which nonspecifically blocks Ca^{2+} channels at this concentration, abolished all types of Ca^{2+} spikes while sparing bAPs, reinforcing the conclusion that VGCCs are fundamental for ADP and DI spike generation (**Fig. 8G**).

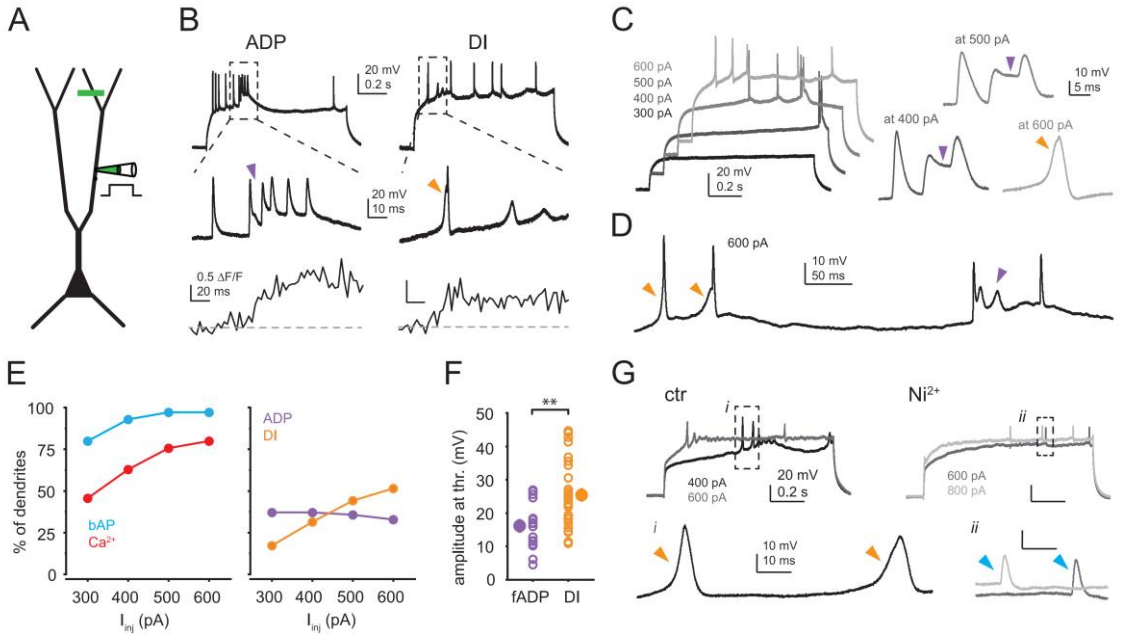

Figure 8. Characterization of dendritic Ca^{2+} spike types. ***(A)*** *Schematic of dendritic patch-clamp experiment.* ***(B)*** *Example dendritic voltage (top) and Ca^{2+} signal (bottom) traces illustrating two distinct forms of Ca^{2+} spikes: ADP (left) and DI spike (right) from different cells.* ***(C)*** *Dendritic responses to increasing I_{inj}. Magnified views on the right highlight the distinct spike types, with purple arrowheads marking ADPs and the orange arrowhead indicating a DI spike.* ***(D)*** *Heterogeneous Ca^{2+} spike activity recorded from a single dendritic trace at 600 pA I_{inj}, showing the coexistence of multiple spike forms.* ***(E)***

Left: proportion of dendrites expressing bAPs and Ca^{2+} spikes (ADPs and DI spikes included) in response to 300–600 pA I_{inj}. Right: proportion of dendrites expressing distinct Ca^{2+} spike types (ADPs and DI spikes) under the same current conditions (pooled dual- and single-site recordings, n = 70 dendrites). ***(F)*** *Amplitude comparison of fast ADPs and DI spikes at threshold current injections. Open circles represent individual dendrites, filled symbols indicate the mean ± SEM across experiments.* ***(G)*** *Example traces recorded at two different I_{inj} levels under control conditions (top) and after bath application of 200 µM Ni^{2+} (bottom). Insets on the right (dashed boxes) highlight distinct spike components: (i) DI spikes (orange arrowhead) and (ii) bAPs (light blue arrowhead) (Magó et al., 2021).*

To determine whether these distinct Ca^{2+} spike forms could also be evoked under more physiological stimulation, we employed 2PGU to activate synaptic inputs (**Fig. 9A-C**). We patched dendrites (n = 10 experiments, 230 ± 17 µm from soma); clustered spines (20 per dendrite) located 171–441 µm from the soma were stimulated quasi-simultaneously 5x at 40 Hz, with laser power adjusted to achieve moderately suprathreshold activation. Importantly, these experiments were conducted in the presence of 50 µM D-AP5 to block slow NMDA spikes and isolate Ca^{2+}-spike-specific responses. Synaptic stimulation successfully evoked both ADP and DI spikes, either individually (ADP only: 3/10 dendrites, **Fig. 9B**; DI spikes only: 4/10 dendrites, **Fig. 9C**) or in combination (1/10 dendrites). In the remaining two dendrites, stronger stimulation eventually triggered ADP spikes. All these spike profiles elicited by uncaging closely resembled those evoked by direct current injection.

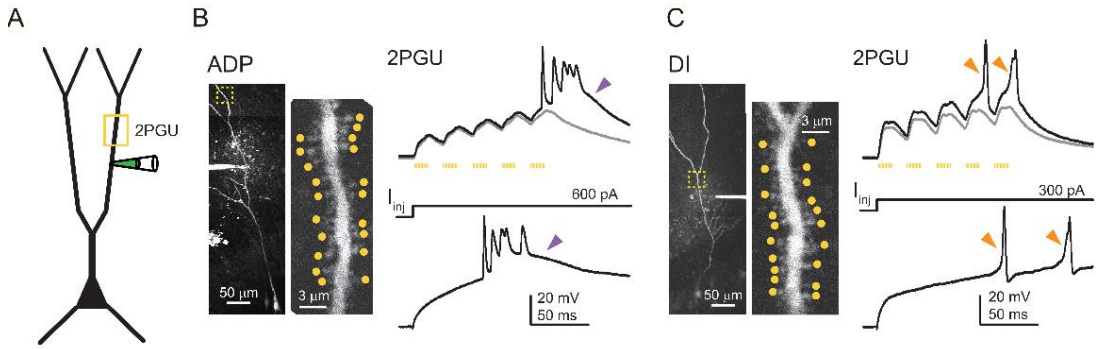

Figure 9. Synaptic activation of dendritic Ca^{2+} spikes via 2PGU. (A) *Schematic of 2PGU experiments.* ***(B)*** *Example dendrite responding to 2PGU. Left: single scan image of a*

dendritic segment showing 20 identified synapses in the plane, targeted for glutamate uncaging (yellow dots). Right, top: voltage responses to five quasi-synchronous stimulations at 40 Hz. Gray traces: subthreshold responses, black traces: suprathreshold events. Right, bottom: The same dendrite responding to I_{inj} via the patch pipette. ***(C)*** *Dendritic recording with a DI spike evoked by 2PGU. The panel follows the same layout as (B), showing similar spike characteristics between 2PGU and I_{inj} stimulation (Magó et al., 2021).*

To isolate dendritic Ca^{2+} spikes from other regenerative events, we applied 1 µM TTX to block VGNCs. As expected, TTX abolished bAPs and dendritic Na^{+} spikes while preserving Ca^{2+} spikes associated with large dendritic Ca^{2+} signals. The kinetics of these spikes were diverse and correlated with the types observed in control conditions. In dendrites expressing only ADP spikes under baseline conditions, the remaining TTX-resistant spikes were typically slow (166.6 ± 26.8 ms, n = 12, **Fig. 10A, C**), whereas dendrites that fired DI spikes exhibited fast, transient TTX-resistant Ca^{2+} spikes (9.3 ± 0.7 ms, n = 13; Mann–Whitney test, $p < 0.001$, **Fig. 10B, C**). In some cases, both fast and slow spike components were observed.

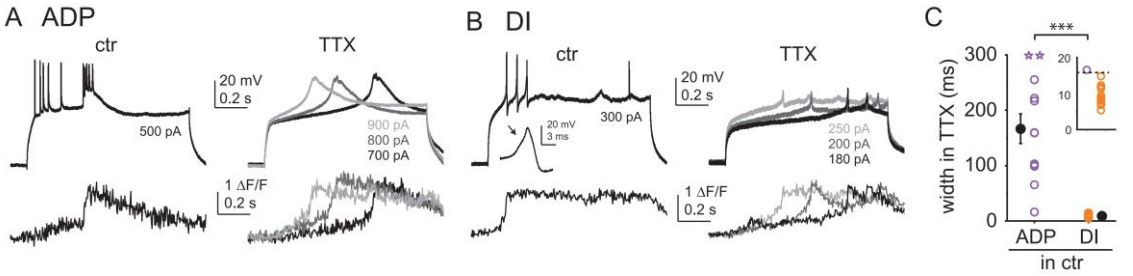

Figure 10. Effect of TTX on ADP and DI spikes. ***(A)*** *Representative traces showing membrane potential (V_m, top traces) and distal dendritic Ca^{2+} signals (bottom traces) recorded during ADP-type Ca^{2+} spikes under control conditions (left) and following application of 1 µM TTX at various I_{inj} levels.* ***(B)*** *Similar recordings from a dendrite exhibiting DI-type Ca^{2+} spikes, showing the effect of TTX on spike waveform and associated Ca^{2+} signals. The inset magnifies the 0–20 ms width range for better visualization of short-duration spikes.* ***(C)*** *Quantification of TTX-resistant Ca^{2+} spike width. Data are shown for dendrites expressing ADP spikes only (purple, n = 12) and dendrites exhibiting DI spikes (orange, n = 13). Open circles represent individual*

dendritic recordings, while open stars indicate dendrites where the spike width was capped at 300 ms because the V_m did not return to half amplitude during the current step duration. Filled black symbols indicate the mean ± SEM. Inset magnifies the 0–20 ms width range (Magó et al., 2021).

The variability in dendritic Ca^{2+} spike properties observed in CA3PCs raised the question of how these compare to the well-characterized dendritic Ca^{2+} spikes in CA1PCs (Golding et al., 1999; Magee and Carruth, 1999; Takahashi and Magee, 2009). Performing similar experiments in CA1PC apical trunks (227–457 μm from the soma, n = 12), we observed that dendritic depolarization by 300–600 pA I_{inj} primarily evoked VGCC-mediated ADP spikes, but these required higher current thresholds than that in CA3PCs (**Fig. 11A–D**). Importantly, DI spikes were absent in CA1PCs, and bAPs consistently preceded Ca^{2+} spikes (**Fig. 11C**).

The duration of TTX-resistant Ca^{2+} spikes in CA1PCs was clearly distinct from those observed in CA3PC dendrites under similar conditions. CA1PC Ca^{2+} spikes displayed an intermediate duration compared to the fast and slow spike types observed in CA3PCs, while their amplitudes were similar (width: 39.4 ± 5.1 ms, n = 6, **Fig. 11F, G**), further indicating cell-type-specific differences in Ca^{2+} spike properties. The Ca^{2+} spikes in CA1PCs were also eliminated by 200 μM Ni^{2+} (**Fig. 11E**), confirming a fundamental role of VGCCs in generating a wide kinetic range of Ca^{2+} spikes.

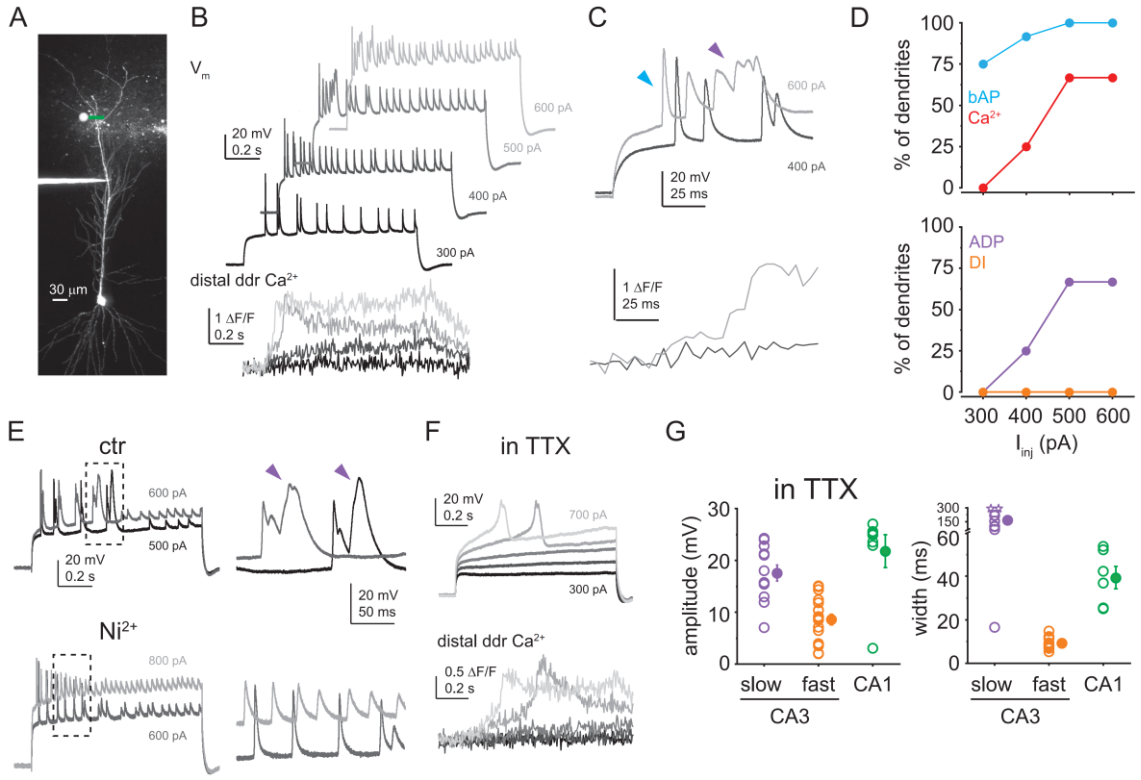

Figure 11. Dendritic Ca^{2+} spikes in CA1PCs. ***(A)*** *2P image of a CA1PC filled with OGB-1 and Alexa Fluor 594 via a dendritic patch pipette.* ***(B)*** *Representative dendritic recordings showing V_m (upper traces) and corresponding distal dendritic Ca^{2+} signals (lower traces) in response to 1-s-long I_{inj} (300–600 pA).* ***(C)*** *Enlarged view of the initial responses to I_{inj} steps, highlighting the prolonged depolarization phase characteristic of ADP-like Ca^{2+} spikes. The first bAP is marked by a blue arrowhead, while the ADP-type Ca^{2+} spike is indicated by a purple arrowhead.* ***(D)*** *Top: proportion of dendrites exhibiting bAPs (light blue) and dendritic Ca^{2+} spikes (red) (n = 12). Bottom: relative distribution of ADP-type Ca^{2+} spikes (purple) and DI Ca^{2+} spikes (orange) across the recorded dendrites (n = 12).* ***(E)*** *Pharmacological analysis of Ca^{2+} spikes. Left: V_m responses to current steps under control conditions (upper traces) and following bath application of 200 µM Ni^{2+} (lower traces). Right: magnified view of the boxed regions, showing the inhibition of ADP-type Ca^{2+} spikes (purple arrows) by Ni^{2+} (n = 3 experiments).* ***(F)*** *Ca^{2+} spikes recorded in the presence of 1 µM TTX to block voltage-gated Na^+ channels. I_{inj} was applied in 100 pA increments (300–700 pA), and associated dendritic Ca^{2+} signals are shown.* ***(G)*** *Comparison of dendritic Ca^{2+} spike properties between CA1PCs and CA3PCs. Spike amplitude and width (measured in TTX) are plotted*

for CA1PCs (green, n = 7/6 for amplitude/width), slow Ca^{2+} spikes in CA3PCs (purple, n = 12), and fast Ca^{2+} spikes in CA3PCs (orange, n = 18/13 for amplitude/width). Spike width was quantified for events with an amplitude exceeding 5 mV. Open stars: where width was maximized as 300 ms because V_m did not return to half amplitude within the duration of the I_{inj} step (Magó et al., 2021).

The distinct characteristics of fast and slow Ca^{2+} spike components raise the question whether their propagation and compartmentalization properties are also different. To address this, we recorded Ca^{2+} spike-associated dendritic Ca^{2+} signals in TTX, both distally within the same dendritic family (250 ± 28 µm distal from the patch pipette, n = 14 cells; depicted as d1 in **Fig. 12A**) and in another dendrite branching off more proximally, typically from a different low-order trunk segment (d2; dendritic distance from pipette: 294 ± 23 µm, n = 14, **Fig. 12A**). We used the high-affinity dye OGB-1 to be able to detect even small increases in Ca^{2+} as a reporter of spike propagation within and across dendritic compartments. We found a strong difference between fast and slow spikes in their propagation properties (two- way repeated measures ANOVA, $p < 0.001$ for kinetic group, $p = 0.005$ for location, $p < 0.001$ for interaction). Slow Ca^{2+} spikes (width > 60 ms) propagated efficiently across major dendritic bifurcation points and were detectable in distant dendritic branches (**Fig. 12B, C**, n = 5 cells, $p = 0.781$, Tukey's post hoc test), including basal dendrites (measured in n = 3 cells). In contrast, fast Ca^{2+} spikes (width < 20 ms) remained restricted to their originating dendritic compartment and did not propagate efficiently across proximal branch points (**Fig. 12B, C**; n = 9 cells, $p < 0.001$, Tukey's post hoc test). These findings highlight distinct propagation mechanisms for fast and slow Ca^{2+} spikes, suggesting that slow spikes may act as global signals across the dendritic tree, whereas fast spikes remain compartmentalized within specific dendritic domains, where they originate (**Fig. 12D)**.

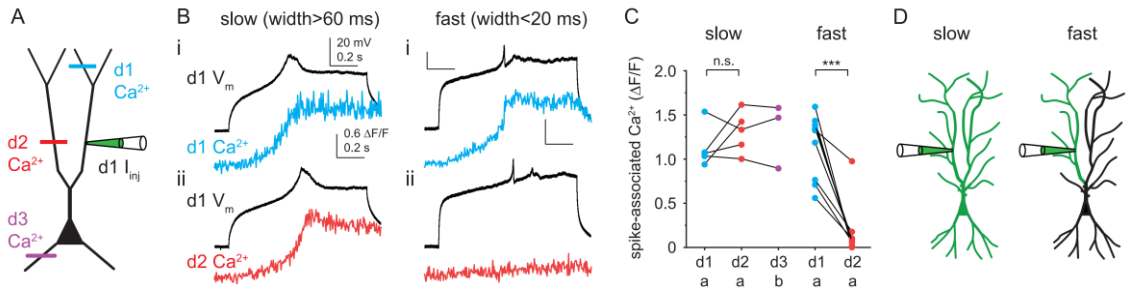

Figure 12. Propagation of different Ca^{2+} spikes. ***(A)*** *Dendritic Ca^{2+} signals were monitored using 2P imaging across different regions of the dendritic tree.* ***(B)*** *Examples of TTX-resistant Ca^{2+} spikes showing distinct propagation patterns. Left: a slow Ca^{2+} spike evoking robust Ca^{2+} signals in both the patched dendritic branch (i) and a neighboring apical subtree (ii). Right: a fast Ca^{2+} spike generates strong Ca^{2+} signal in the patched branch (i) but shows no propagation to the neighboring subtree (ii). Ca^{2+} signals were measured using the high-affinity Ca^{2+} indicator OGB-1.* ***(C)*** *Slow Ca^{2+} spikes generated large, widespread Ca^{2+} signals in apical (a) as well as basal (b) dendrites, whereas fast Ca^{2+} spikes exhibited localized signals.* ***(D)*** *Schematic representation of compartmentalization rules governing Ca^{2+} spike propagation (Magó et al., 2021).*

As our previous results have indicated, the electrophysiological properties of CA3PCs are linked to their topographic position and dendritic morphology. We therefore also examined the relationship between dendritic Ca^{2+} spike phenotype and some of the morphological properties (the abundance of TEs and the number and length of primary apical trunks) of CA3PCs in our dendritic recording dataset. TE coverage of proximal dendrites varied significantly (**Fig. 13A, B**) and was inversely correlated with the length of first-order apical trunks (**Fig. 13C**, Spearman $R = -0.495$, $p < 0.001$, $n = 89$), consistent with our previous observation as well as with prior reports (Fitch et al., 1989). The dendritic Ca^{2+} spike phenotype correlated with these anatomical features. CA3PCs expressing DI spikes in the recorded dendrite (with or without ADPs) had approximately twice the TE coverage (**Figure 13D**, ADP-only: 40 ± 5 µm, n = 19; DI: 84 ± 8 µm, n = 35, $p < 0.001$, Mann–Whitney test) compared to ADP-only cells. Furthermore, DI spike-expressing cells had shorter primary trunks (**Figure 13E**, ADP-only: 128 ± 11 µm, n =

20; DI: 57 ± 5 µm, n = 41, p = 0.002) and were more likely to have multiple first-order trunks (**Figure 13F**, ADP-only: 1 ± 0, n = 20; DI: 1.49 ± 0.11, n = 41, p < 0.001).

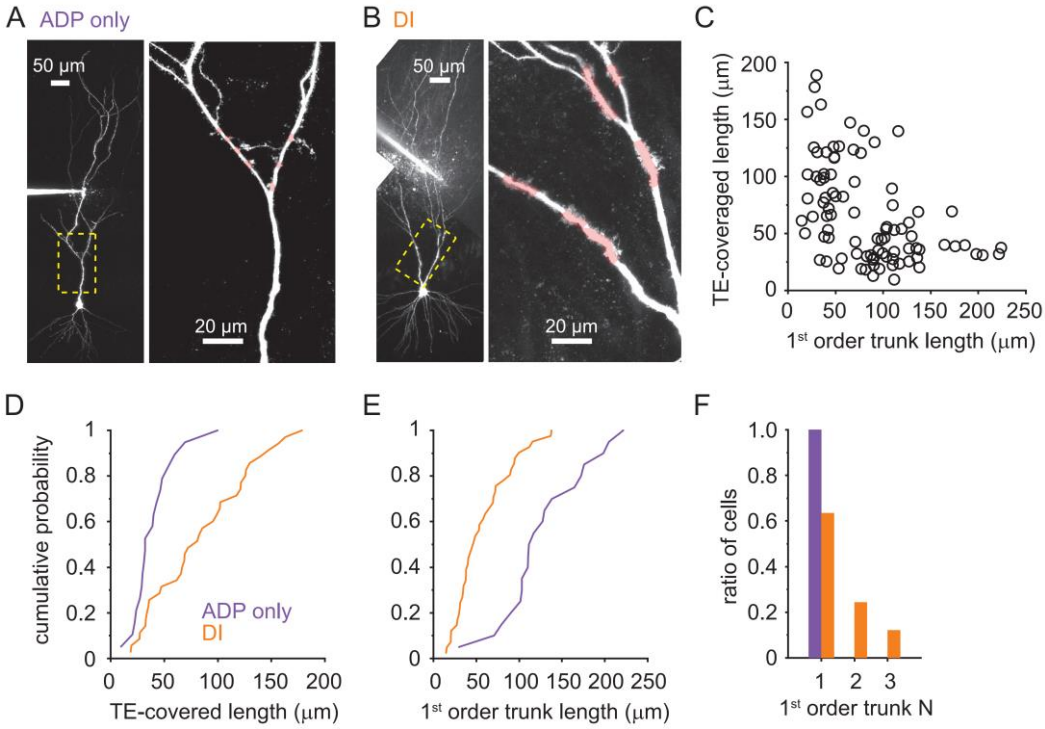

Figure 13. Correlation between dendritic Ca^{2+} spike phenotypes and morphological features. ***(A, B)*** *Representative 2P images show two distinct CA3PC morphologies corresponding to ADP-only spikes (A) and DI spikes (B). Enlarged views of the yellow dashed boxes highlight TEs, marked by pink shading on the primary trunk segments.* ***(C)*** *Scatter plot showing the relationship between the length of the first-order apical trunk and the total dendritic length covered by TEs among CA3PCs (n = 89 cells). For cells with multiple primary trunks, the mean trunk length is plotted.* ***(D, E)*** *Cumulative probability distributions of morphological parameters for cells exhibiting ADP-only (purple) or DI (orange) Ca^{2+} spike phenotypes: (D) Total TE-covered dendrite length (n = 19 ADP-only; n = 35 DI) and (E) first-order apical trunk length (n = 20 ADP-only; n = 41 DI).* ***(F)*** *Number of first-order apical trunks in CA3PCs expressing ADP-only (purple, n = 20) or DI (orange, n = 41) Ca^{2+} spikes (Magó et al., 2021).*

Importantly, at the somatic level, ADP and DI spikes evoked in the patched dendrites evoked distinct output patterns. ADP spikes promoted bursts of APs, whereas DI spikes

produced only single somatic action potentials (**Fig. 14A-B**). These findings suggest that the two spike types serve different computational roles within CA3PCs, potentially contributing to diverse synaptic integration and firing behaviors.

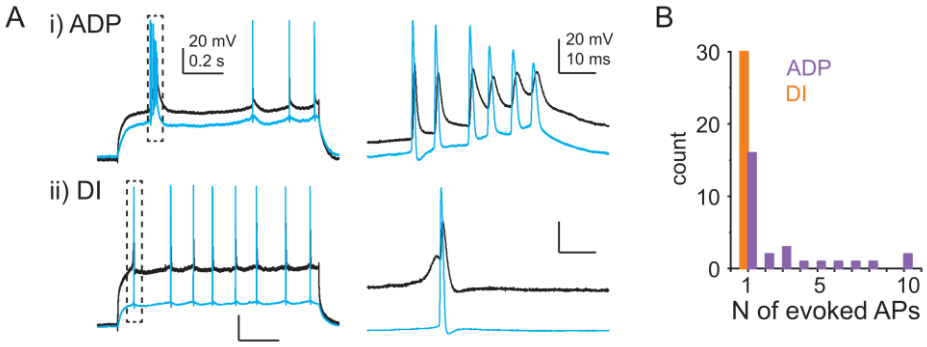

Figure 14. Opposing impact of different Ca^{2+} spike types on somatic output. (A) *Example AP output evoked by ADP (i) and DI spike (ii) in dual recordings at different cells (blue: somatic voltage, black: dendritic voltage). Responses (dashed box) are shown at higher temporal resolution on the right panels.* ***(B)*** *Median number of APs evoked at threshold I_{inj} by ADPs and DI spikes in individual cells (Magó et al., 2021).*

The results of our dendritic recordings suggested a surprisingly complex dendritic integrative regime in CA3PCs, where individual apical dendrites can act as diverse Ca^{2+} spike generators producing fast or slow Ca^{2+} spikes. Nevertheless, the cell population displayed large cell-to-cell heterogeneity in these properties. The results opened fundamental questions about the ion channel mechanisms underlying the diversity of spike characteristics, the spatial organization of the different Ca^{2+} spikes in the arbor, their final integration at the soma to produce AP output.

Furthermore, it remained to be addressed whether the Ca^{2+} spike profile of a given CA3PC is static or dynamically regulated. On one hand, the correlation between functional and morphological properties of CA3PCs points to an at least partially rigid organization of dendritic spike mechanisms across dendritic compartments; for example, long primary trunks may facilitate the generation of low-threshold, slow Ca^{2+} spikes, whereas higher-order trunks act as individual Ca^{2+} spike generators. On the other hand, the ion channels contributing to generating or shaping the Ca^{2+} spikes might be under

activity- or state-dependent regulation, rendering further flexibility to active dendritic properties of CA3PCs.

In the following part of our study, we aimed to address these open questions. The following chapters present our findings on how various dendritic spike summation at the soma determines the shape and burstiness of AP output.

4.3. Compound Ca^{2+} spikes

4.3.1. Cell-to-cell heterogeneity of compound dendritic Ca^{2+} spikes

To gain a deeper understanding of how dendritic Ca^{2+} spikes in different branches can interact and contribute to somatic activity in CA3PCs, we next employed a different approach, where we recorded at the soma and induced dendritic Ca^{2+} spikes by somatic depolarization while pharmacologically blocking VGNC with TTX (1 μM). Long (1 s) step or ramp depolarizing current injections (**Fig. 15A**) were applied to induce widespread Ca^{2+} channel activation across the apical dendritic tree, during which dendritic Ca^{2+} signals were also recorded (**Fig. 15B**). This approach allowed us to investigate how Ca^{2+} spikes with diverse kinetic properties from various dendritic compartments combine into compound somatic Ca^{2+} spike events. We hypothesized that global depolarization of the apical dendritic tree could recruit spatially distributed dendritic Ca^{2+} spikes with varying kinetics, resulting in compound Ca^{2+} spikes dominated by either fast or slow components.

Under these conditions, regenerative compound Ca^{2+} spikes could be consistently evoked in the majority of cells (331 out of 361 cells, 91.7%; **Fig. 15C**). Interestingly, while the waveform of Ca^{2+} spikes remained stereotypical within individual CA3PCs (regardless of the level of I_{inj}) (**Fig. 15D**), their properties varied across different cells. Specifically, spike amplitude showed a normal distribution ($n = 317$, $P = 0.416$, Shapiro–Wilks test for normality), whereas kinetic parameters, including the duration (measured as the halfwidth), showed non-Gaussian distribution and large coefficient of variation (CV; **Fig. 15E**). The most heterogeneous parameter was Ca^{2+} spike halfwidth (CV = 0.984, $P < 0.001$, Shapiro–Wilks test; **Fig. 15E**). Based on this parameter, cells could be categorized into two main groups: short-duration Ca^{2+} spikes (peak halfwidth ~9.44 ms) and long-lasting Ca^{2+} spikes (peak halfwidth ~46.24 ms). Within the long-lasting group, further heterogeneity was observed, with many cells exhibiting complex, multipeak spike

phenotypes, which were a mixture of slow and superimposed fast components characterized by repetitive activations at frequencies between 10–70 Hz (35.3 ± 1.3 Hz, n = 89; **Fig. 15C** and **Div**).

While the Ca^{2+} spikes were evoked by I_{inj} at the soma, both short and long-duration events were accompanied by time-locked Ca^{2+} signals in distal apical dendrites located more than 300 µm from soma, with similar amplitudes across spike types (**Fig. 15C**).

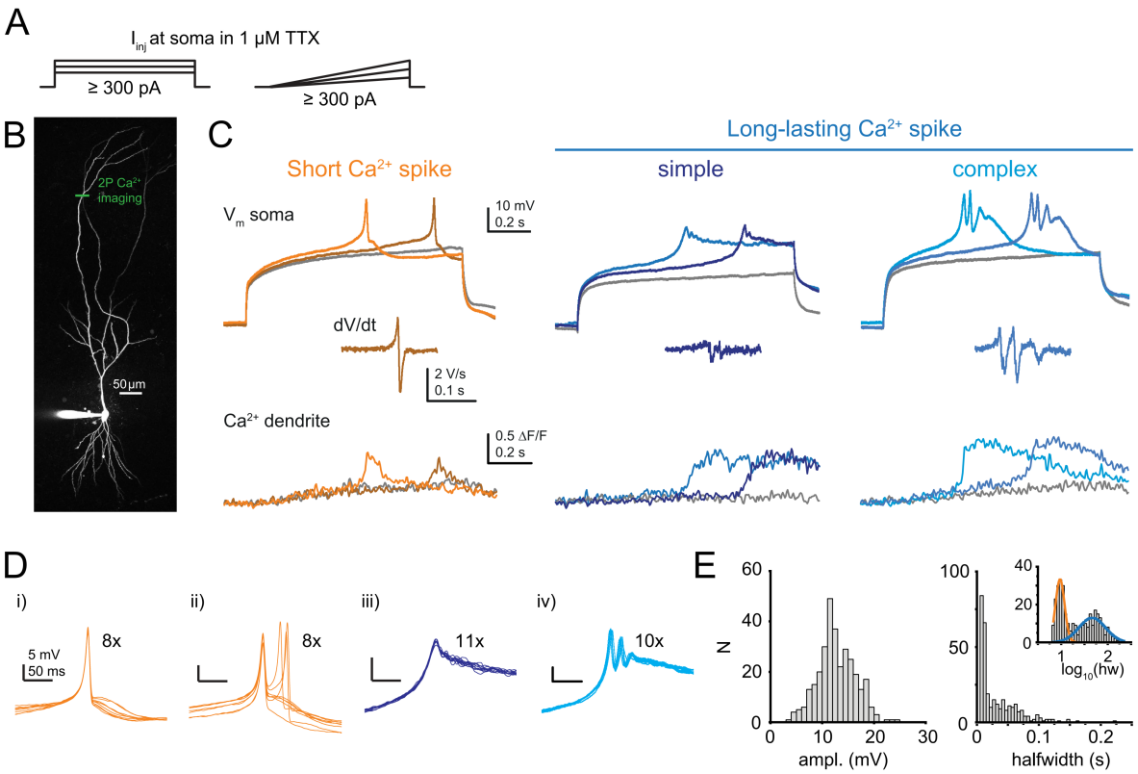

Figure 15. Characterization of compound Ca^{2+} spikes in CA3PCs using somatic I_{inj} and 2P imaging. ***(A)*** *1-s-long step (left) and ramp (right) somatic I_{inj} protocols with variable amplitude to evoke compound Ca^{2+} spikes.* ***(B)*** *2P collapsed Z-stack image of a CA3PC loaded with Alexa Fluor 594 and OGB-1. The green line indicates the position of the Ca^{2+} imaging.* ***(C)*** *Representative examples of compound Ca^{2+} spike types recorded from three distinct CA3PCs. Top panels: somatic voltage responses to subthreshold and two levels of suprathreshold I_{inj}. Middle panels: dV/dt traces showing the temporal dynamics of the corresponding Ca^{2+} spikes (color-matched with the top panel). Bottom panels: Ca^{2+} signals recorded distally from dendrites, aligned with the somatic voltage traces* ***(D)*** *(i, iii, iv) Examples showing stereotypical Ca^{2+} spikes, where repeated stimulations produced highly consistent waveforms. (ii) In some cases, short-duration Ca^{2+} spikes*

displayed an additional secondary peak, with slight temporal variability across repetitions. ***(E)*** *Distribution of the amplitude (left) and the halfwidth (right) of compound* Ca^{2+} *spikes (n = 317 cells). The inset shows the* log_{10} *(halfwidth) values that segregate to two distinct groups (Kis et al., 2024).*

We performed hierarchical clustering analysis based on the most distinctive spike parameters, including dV/dt_{total}, duration, and number of peaks (**Fig. 16A**). The analysis confirmed that the observed heterogeneity in Ca^{2+} spike waveforms could be well described by three clusters: a first division of the dendrogram produced short- and long-lasting Ca^{2+} spike groups, and the latter group was further subdivided into simple and complex forms (**Fig. 16B**, n = 317 cells). Short Ca^{2+} spikes had on average steeper rise and decay compared to long-lasting Ca^{2+} spikes, while their amplitude and threshold were relatively similar (**Fig. 16C**).

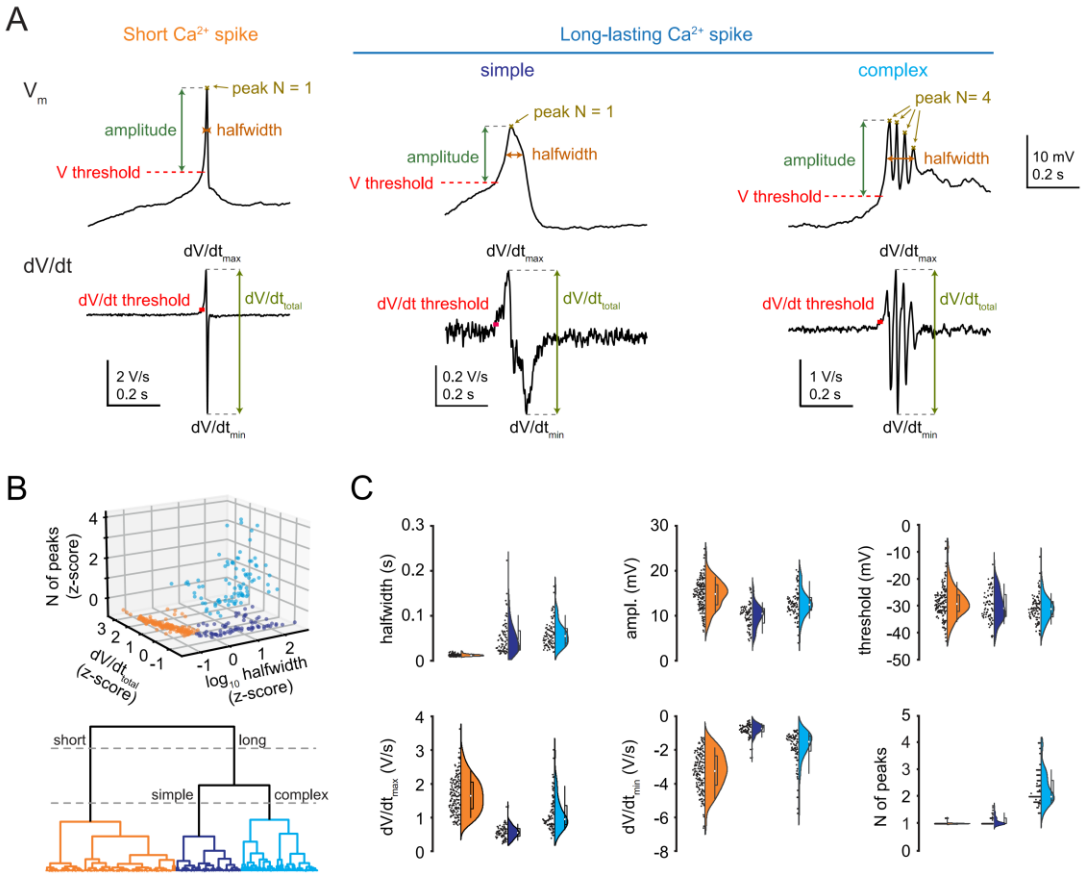

Figure 16. Properties, hierarchical cluster analysis and the distribution of kinetic parameters of Ca^{2+} ***spikes (A)*** *Definition of compound* Ca^{2+} *spike parameters. Top:*

example somatic voltage responses to I_{inj}. Bottom: the corresponding dV/dt belonging to the Ca^{2+} spike. Same scale bar applies for all V_m traces, whereas the Y scales of dV/dt traces are different. ***(B)*** *Hierarchical clustering of Ca^{2+} spike types based on kinetic parameters. Top panel: individual data points representing 317 CA3PCs plotted along the three primary z-scored kinetic parameters. Bottom panel: dendrogram of the clustered dataset, revealing three distinct groups: short Ca^{2+} spikes (n = 152), simple long-lasting Ca^{2+} spikes (n = 76), and complex long-lasting Ca^{2+} spikes (n = 89).* ***(C)*** *Comparison of kinetic parameters across Ca^{2+} spike groups. Distribution plots highlight significant differences between short-duration spikes and long-lasting spikes across several parameters: maximum rise rate (dV/dt_{max}, $P < 0.001$), maximum decay rate (dV/dt_{min}, $P < 0.001$), amplitude ($P < 0.001$), halfwidth ($P < 0.001$), spike threshold ($P = 0.004$), and number of peaks ($P < 0.001$) (Mann–Whitney test) (Kis et al., 2024).*

Ca^{2+} spikes, as shown in both our work (Raus Balind et al., 2019) and that of others (Grienberger et al., 2014; Wong and Prince, 1978), play a critical role in driving CSB firing at the soma. To directly determine the relationship between compound Ca^{2+} spikes and somatic firing pattern, we measured CSB rates and durations under control conditions in ACSF and subsequently in TTX to eliminate APs and isolate Ca^{2+} spikes. Cells expressing short-duration compound spikes displayed a low (or no) propensity for CSB generation and predominantly exhibited regular spiking behavior. When CSBs were observed in these cells (typically at higher I_{inj} levels), they were short in duration. In contrast, cells exhibiting long-duration compound Ca^{2+} spikes showed a higher CSB propensity, often producing long, plateau-like bursts (**Fig. 17A** and **B**).

These results again demonstrated significant cell-to-cell heterogeneity in compound Ca^{2+} spike properties among CA3PCs, consistent with the previous observations. Importantly, our data altogether suggest that a subpopulation of CA3PCs expresses only short-duration Ca^{2+} spikes and therefore cannot sustain prolonged depolarization and CSBs, whereas cells with long-lasting spikes effectively drive somatic plateau potential.

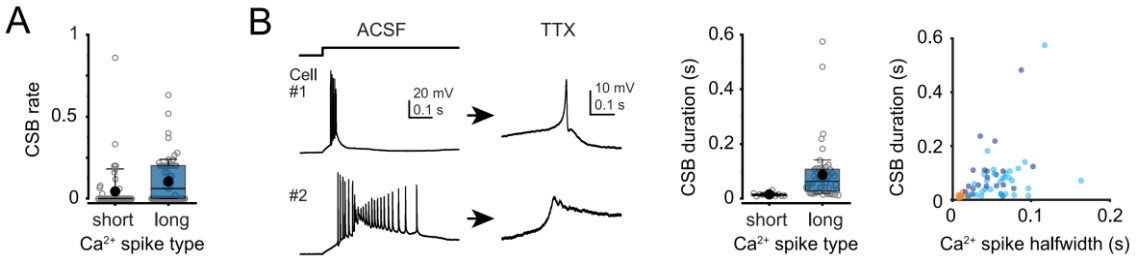

Figure 17. Relationship between Ca^{2+} spike types and CSB properties. (A) *Comparison of CSB rate between short (n = 62) and long-lasting Ca^{2+} spikes (n = 75), measured at 600 pA (P = 0.002, Mann–Whitney test). Gray open circles represent individual cells, the box plot shows the interquartile range, the horizontal line indicates the median, the filled black circle denotes the mean and whiskers represent the 10th to 90th percentile.* ***(B)*** *Kinetic relationship between CSBs and underlying Ca^{2+} spike types. Left panel: example CSBs recorded in ACSF alongside their corresponding Ca^{2+} spikes observed in TTX (segments taken from 1-s-long I_{inj} steps). Middle panel: CSB duration was significantly longer in cells expressing long-lasting Ca^{2+} spikes (n = 52) compared to those with short Ca^{2+} spikes (n = 11, P < 0.001, Mann–Whitney test). Box plot follows the same conventions as in (A). Right panel: correlation between CSB duration and Ca^{2+} spike halfwidth across recorded cells (n = 63, Spearman R = 0.564, P < 0.001), indicating a positive relationship between spike kinetics and burst duration (Kis et al., 2024).*

4.3.2. Morpho-topographic mapping of compound Ca^{2+} spike heterogeneity

As mentioned in the previous chapters, we observed correlations between topographic location and CSB propensity, as well as between dendritic morphology and dendritic Ca^{2+} spike properties in CA3PCs. We therefore also aimed to investigate comprehensively how compound Ca^{2+} spike phenotypes relate to these anatomical features. By mapping Ca^{2+} spike phenotypes onto the proximo-distal and radial (taking primary dendrite length as a proxy) position of the cells (**Fig. 18A and B)** (Bilkey and Schwartzkroin, 1990; Fitch et al., 1989; Hunt et al., 2018; Ishizuka et al., 1995; Lee et al., 2004; Masukawa et al., 1982; Sun et al., 2017; Yao et al., 2021), we discovered a non-uniform distribution of spike types across the CA3 area (**Fig. 18C**). Cells with short-duration Ca^{2+} spikes were mainly located in proximal CA3, whereas long-lasting spikes were enriched in distal CA3, particularly in deeper layers associated with longer primary

apical dendrites (**Fig. 18C and D**). In distal CA3, short spikes were mostly restricted to PCs with short primary trunks (**Fig. 18C and D**), often heavily decorated with TEs. These results are in line with our previously described distribution of RS and CSB cells (Raus Balind et al., 2019) as well as with our earlier finding that individual apical dendrites expressing fast dendritic Ca^{2+} spikes are more likely to be observed in cells with short trunk(s) (Magó et al., 2021).

Next, we analyzed whether different Ca^{2+} spike types are also associated with distinct apical dendritic arborization patterns in the CA3 area. This analysis revealed that cells with short-duration spikes often possessed multiple primary apical trunks, while those with long-lasting spikes typically had one (**Fig. 18E**). To further explore the relationship between proximal apical dendritic structure and Ca^{2+} spike phenotype, we performed Sholl analysis at four distances from the soma (50, 100, 150, and 200 μm), which revealed that cells with long-duration spikes had simpler apical dendritic arbors, reflected in a lower number of intersections at all measured distances (**Fig. 18F, G**). These differences were more pronounced than those found in our earlier study investigating CSBs using Sholl analysis, where only subtler morphological differences were detected between CSB_H and RS cells (Raus Balind et al., 2019): Sholl analysis highlighted some proximodistal differences but showed correlation only of primary dendrite length (but not with dendritic complexity) with CSB propensity (**Fig. 6H**). However, in that study we had much lower sample size, and we focused only on the CSB propensity (CSB_H or RS) without considering the duration of the burst, whereas in the current study we categorized cells based on their compound Ca^{2+} spike properties. One possible explanation for the discrepancy can be the relationship between Ca^{2+} spike phenotype and CSB propensity. Cells with short-duration Ca^{2+} spikes mostly exhibit RS firing, but they can occasionally also fire CSBs; however, these CSBs are short in duration. In contrast, cells with a higher tendency to produce CSBs (especially long, plateau-like bursts) are more likely to exhibit long-lasting compound Ca^{2+} spikes. Thus, the characteristics of the compound Ca^{2+} spike better predict the anatomical and morphological properties of CA3PCs than CSB propensity.

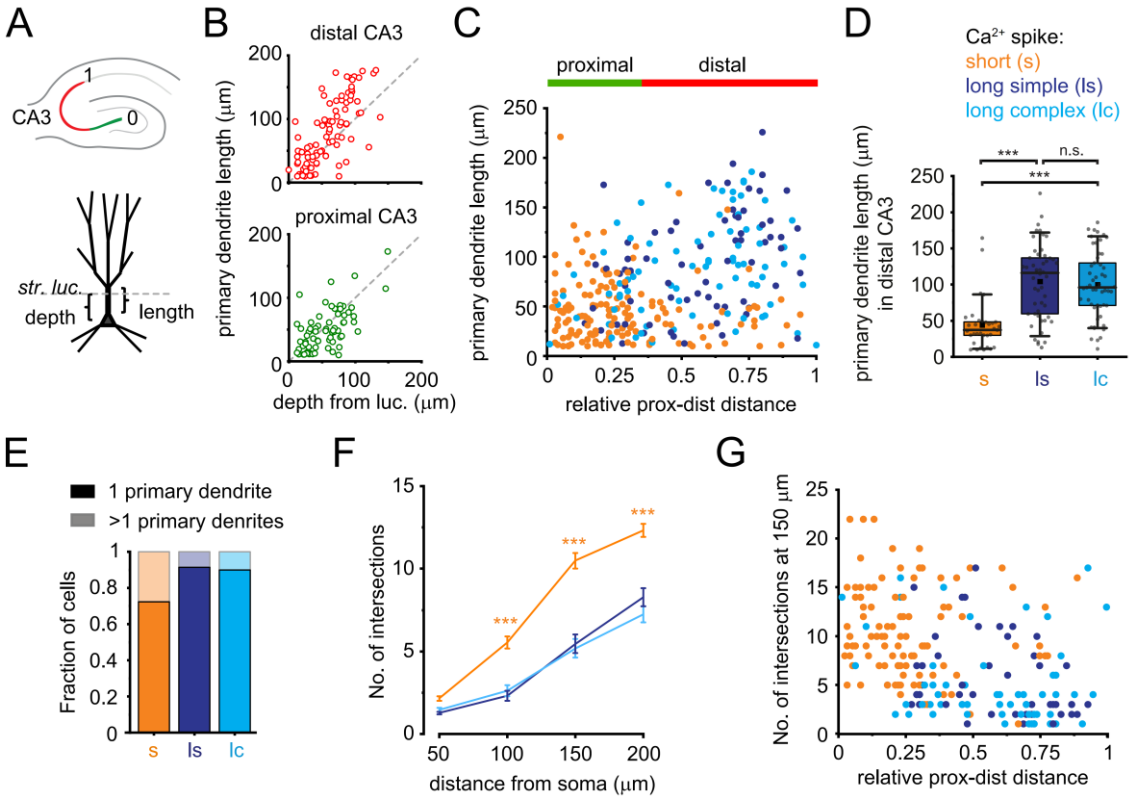

Figure 18. Morpho-topographic correlates of Ca^{2+} spikes. ***(A)*** *Measurement parameters for morphological and positional analysis. Top: proximodistal position was defined relative to the dentate gyrus (proximal) and CA2 (distal). Bottom: primary apical trunk length was measured from the soma to the first main bifurcation point.* ***(B)*** *Correlation between soma depth and primary trunk length across proximal (green, relative position ≤0.3, n = 68) and distal (red, relative position 0.4–1, n = 94) CA3PCs. Deeper soma correlated with longer primary trunks (distal: Spearman R = 0.748, P < 0.001, proximal: Spearman R = 0.556, P < 0.001).* ***(C)*** *Distribution of Ca^{2+} spike clusters across the proximodistal axis and primary trunk length. Individual cells (n = 298) are represented as dots, color-coded by Ca^{2+} spike cluster: short (orange), simple long-lasting (deep blue), and complex long-lasting (light blue).* ***(D)*** *Comparison of primary dendrite length in distal CA3PCs. Primary dendrite length differed significantly between short and long-lasting spike cells (Kruskal–Wallis test: P < 0.001), but not between simple and complex long-lasting clusters (P = 1).* ***(E)*** *Proportion of CA3PCs with one or multiple primary apical trunks analyzed separately for short-duration (n = 148), simple long-lasting (n = 70), and complex long-lasting (n = 80) spike clusters.* ***(F)*** *Sholl analysis of apical dendrites (n = 211 cells). Statistical analysis revealed significant effects of distance from*

soma, spike cluster type, and their interaction (P < 0.001 for all, Mixed ANOVA). Post hoc Tukey's tests showed significant differences between short vs. simple long-lasting (P < 0.001) and short vs. complex long-lasting clusters (P < 0.001) at 100, 150, and 200 µm, but no differences between the two long-lasting clusters (P > 0.890) at any distance. ***(G)*** *Apical dendritic intersections at 150 µm were plotted against proximodistal position, color-coded by* Ca^{2+} *spike cluster identity (n = 211, colors as in (C)) (Kis et al., 2024).*

In our large dataset of hundreds of recorded and 2P-imaged CA3PCs throughout the research project, we consistently observed TEs – albeit in varying densities – on the proximal dendrites. Despite our best effort, we did not find cells that completely lacked TEs (athorny cells', Hunt et al. 2018); TE-like structures (even if only one or a few) were always present even in deep distal CA3PCs. Nevertheless, because 2P imaging has relatively lower resolution compared to other fluorescent cellular imaging techniques, we aimed to confirm this conclusion by examining a subset of CA3PCs (after 2P microscopy) using stimulated emission depletion (STED) super-resolution imaging to visualize proximal dendrites in str. lucidum. Our primary focus was on deep distal CA3PCs, as this subpopulation was most likely to correspond to the previously described bursting cells. Using these advanced imaging techniques, we observed that every CA3PC, recorded and STED-imaged in a subset of experiments (n = 10 cells), displayed well-defined TEs, including those in deep distal regions (**Fig. 19A and C-H**). While the density and spatial distribution of TEs appeared somewhat reduced in distal CA3 compared to proximal regions (**Fig. 19B and I–K**), TEs were consistently present. This finding strongly indicates that CA3PCs in adult rats, regardless of their proximodistal or radial location, receive innervation from MFs.

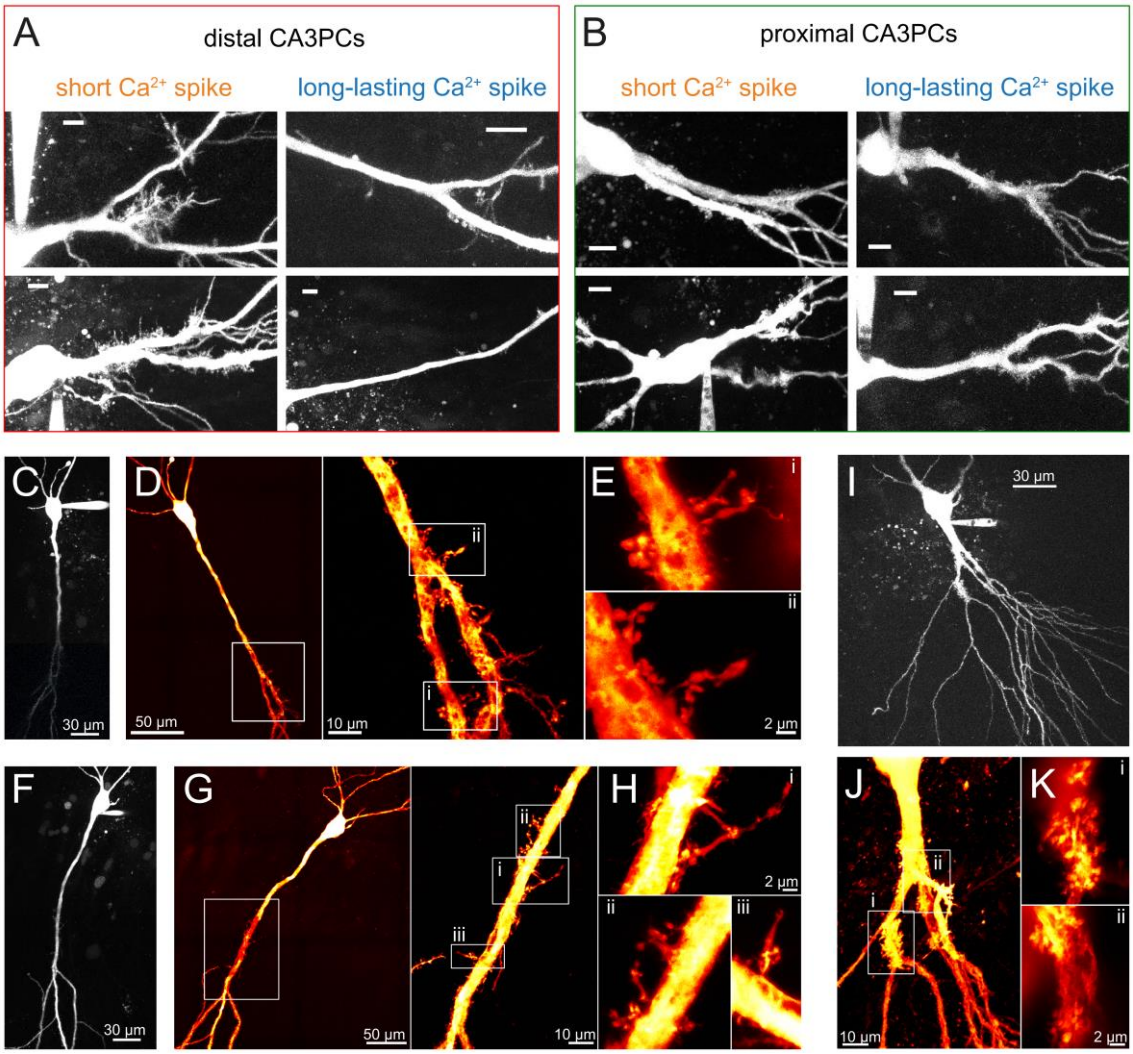

Figure 19. 2P, confocal and STED images of proximal apical dendrites of CA3PCs with diverse TE coverage and Ca^{2+} spike phenotypes. ***(A)*** *Example distal CA3PCs expressing short, and long Ca^{2+} spikes. Scale bars: 10 µm.* ***(B)*** *Proximal CA3PCs with both short and long-duration Ca^{2+} spikes show dense TE clustering along their primary apical trunks and, in some cases, extending onto basal dendrites. Scale bars: 10 µm.* ***(C)*** *2P z-stack of a long-shafted deep distal CA3PCs filled with Alexa Fluor 594 and biocytin.* ***(D)*** *Confocal maximum intensity projection images of the cell in C. White box indicates the location of the enlarged apical dendritic area. Note the TEs along the trunk.* ***(E)*** *Boxed areas (i, ii) are shown at higher magnification with STED microscopy.* ***(F–H)*** *Same as C–E for another long-shafted deep distal CA3PCs filled with Alexa Fluor 594 and biocytin.* ***(I)*** *2P z-stack of a short-shafted proximal CA3PCs filled with Alexa Fluor 594 and biocytin.* ***(J)*** *Confocal image of the apical trunk of the cell in I. Note the clusters of TEs on the primary and secondary apical trunks.* ***(K)*** *STED microscopy image sections*

of TE clusters of the cell in I and J (i, ii) (Kis et al., 2024). Confocal and STED images were made by Judit Herédi.

4.3.3. Ion channels underlying diverse Ca^{2+} spike forms

What are the biophysical mechanisms driving the kinetic diversity of dendritic Ca^{2+} spikes? While passive properties arising from different morphologies might contribute, we hypothesized that the observed variability is more likely attributed to differences in the VGCCs and K^+ channels responsible for generating and modulating Ca^{2+} spikes. Using the high-throughput somatic recording approach, we next explored the ion channels contributing to short- and long-duration compound Ca^{2+} spikes.

One possibility we considered was that distinct types of VGCCs might differentially shape the kinetics and duration of Ca^{2+} sikes. VGCCs have many subtypes (T, L, R, N, and P/Q) and exhibit unique activation and inactivation kinetics (Avery and Johnston, 1996; Fisher et al., 1990; Johnston et al., 1980; Mogul and Fox, 1991; Tanabe et al., 1998). To determine whether specific VGCC subtypes contribute differently to short- and long-lasting Ca^{2+} spikes, we systematically applied specific pharmacological blockers and analyzed their effects on Ca^{2+} spike amplitude and rate of rise (dV/dt_{max}). We found that the T-type channel inhibitor TTA-P2 (10 μM) (along with other T-type blockers), caused only a slight reduction in long-lasting Ca^{2+} spikes. Similarly, the R-type channel inhibitor SNX-482 (0.5 μM) marginally affected long-duration spikes, while the N/P/Q-type channel inhibitor ω-CTX MVIIC (CTX, 1 μM) slightly suppressed short Ca^{2+} spikes. However, none of these blockers produced robust effects (**Fig. 20A**, **B**). The efficacy of these blockers at the applied concentrations was verified in independent control experiments (data not shown).

In contrast to the above VGCC inhibitors, blocking L-type VGCCs with nimodipine (20 μM) or nifedipine (10 μM) consistently abolished or strongly reduced the amplitude and dV/dt_{max} of both short- and long-lasting Ca^{2+} spikes (**Fig. 20A**, **B**). This finding suggests that L-type VGCCs are the dominant contributors to dendritic Ca^{2+} spikes in CA3PCs, irrespective of their kinetic properties. Therefore, the heterogeneity in Ca^{2+} spikes cannot be explained by different contributions from distinct VGCC subtypes.

Since VGCCs could not explain the observed variability in Ca^{2+} spike kinetics, we turned our attention to K^+ channels. Specifically, we hypothesized that K^+ conductances

might actively regulate the duration of short Ca^{2+} spikes by accelerating their repolarization and preventing the emergence of prolonged event. We began by testing blockers for several prominent candidate K^+ channel types, including Ca^{2+}-activated K^+ channels (combination of 0.1 µM IbTx and 0.1 µM apamin), Kv1-containing channels (0.1 µM DTX), and Kv2-containing channels (0.1 µM GxTX). While these treatments modulated spike amplitude and dV/dt, they failed to significantly prolong the halfwidth of short Ca^{2+} spikes, suggesting that these channel types are not primarily responsible for regulating spike duration (**Fig. 20D**). However, two VGKC types emerged as key regulators of Ca^{2+} spike duration. First, inhibition of the A-type K^+ current (mediated by

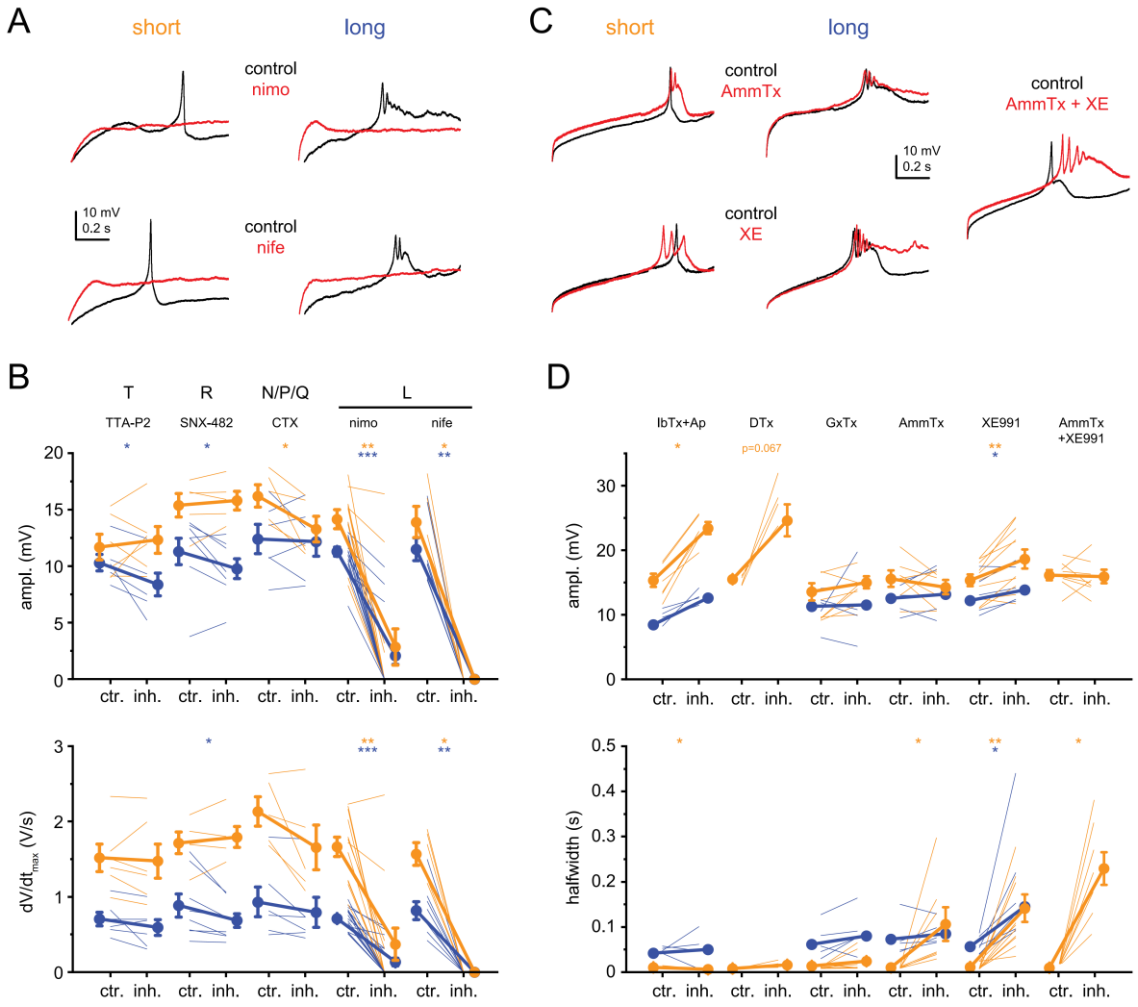

Figure 20. Ion channel contributions to diverse Ca^{2+} spike forms in CA3PCs. (A) *Example recordings of short (left) and long-lasting (right) Ca^{2+} spikes in the presence of TTX. Voltage responses are shown before (black, control) and 10–20 minutes after (red) bath application of the L-type VGCC inhibitors: nimodipine (top) and nifedipine*

(bottom). ***(B)*** *Summary of various VGCC inhibitors effect on Ca^{2+} spike amplitude (top) and dV/dt_{max} (bottom) in short (orange) and long (blue) Ca^{2+} spikes. Thin lines are individual experiments, connected symbols show the mean ± SEM. Complete spike elimination is represented by a value of 0. Tested inhibitors: TTA-P2: n = 6 short, n = 6 long; SNX-482: n = 5 short, n = 8 long; CTX: n = 5 short, n = 6 long; nimodipine: n = 12 short, n = 19 long; nifedipine: n = 5 short, n = 8 long.* ***(C)*** *Representative traces of short (left) and long (middle) Ca^{2+} spikes in TTX, recorded before (black) and after (red) bath application of A-type VGKC inhibitor AmmTx3 (top) and M-type VGKC inhibitor XE991 (bottom). Right panel: example showing the effect of combined A-type and M-type VGKC inhibition in a cell initially expressing a short Ca^{2+} spike.* ***(D)*** *Summary of the changes in spike amplitude (top) and halfwidth (bottom) in short (orange) and long-lasting (blue) Ca^{2+} spikes after applying various VGKC inhibitors. The following inhibitors were tested: combined IbTx and apamin: n = 6 short, n = 4 long; DTX: n = 4 short; GxTx: n = 8 short, n = 5 long; AmmTx3: n = 7 short, n = 5 long; XE991: n = 11 short, n = 6 long; combined AmmTx3 and XE991: n = 8 short.*
**p<0.05, **p<0.01, ***p<0.001, Wilcoxon test (Kis et al., 2024).*

Kv4 channels) using AmmTx3 (1–2 μM) (Zoukimian et al., 2019) resulted in an increase in the halfwidth of short spikes. This suggests that A-type K^+ currents rapidly repolarize dendritic Ca^{2+} spikes, effectively limiting their duration. Second, blocking the M-type K^+ current (mediated by Kv7 channels) with XE991 (10 μM) amplified the slow spike component and prolonged all Ca^{2+} spike forms. In many cases, this blockade also induced repetitive short spike components. When both A-type and M-type K^+ currents were simultaneously inhibited, the effects were even more pronounced: short-duration spikes shifted toward a complex, long-lasting phenotype, resembling the kinetic behavior of the longest compound Ca^{2+} spikes observed under baseline conditions (**Fig. 20C, D**). These results indicate that A-type and M-type K^+ channels play a critical role in determining Ca^{2+} spike kinetics.

4.3.4. Cholinergic regulation of Ca^{2+} spike kinetics

ACh, released by axons originating from the medial septum/diagonal band of Broca, is a key modulator of hippocampal circuits and plays an important role in learning and

memory processes through diverse intrinsic, synaptic, and network-level effects (Hasselmo, 2006; Solari and Hangya, 2018). Among its many molecular targets (Cobb and Davies, 2005; Dannenberg et al., 2017; Prince et al., 2016), ACh is known to modulate the activity of voltage-gated ion channels, including VGCCs (Fisher and Johnston, 1990; Gähwiler and Brown, 1987; Tai et al., 2006; Williams and Fletcher, 2019) and A-type and M-type VGKCs (Gähwiler and Brown, 1987; Nakajima et al., 1986), as well as facilitate burst firing (Macvicar et al., 1989). These effects suggest that cholinergic signaling could regulate CSB firing via modulation of dendritic Ca^{2+} spike properties.

To test this hypothesis, we investigated the impact of cholinergic receptor activation on dendritic Ca^{2+} spikes using the non-hydrolysable cholinergic agonist carbachol (CCh, 2 μM) in the presence of TTX to isolate Ca^{2+} spikes. Remarkably, carbachol transformed short Ca^{2+} spikes into long-lasting forms, reflected in an approximate five-fold increase in spike halfwidth, along with a reduction in amplitude and dV/dt_{max} (**Fig. 21A)**. In contrast, combined blockade of nicotinic and muscarinic ACh receptors with hexamethonium (100 μM) and ipratropium bromide (10 μM) failed to shorten the long-lasting Ca^{2+} spikes (**Fig. 21B**). This observation suggests that the baseline heterogeneity of Ca^{2+} spike kinetics in CA3PCs cannot be explained by variable levels of cholinergic tone in the acute slice.

To further investigate the functional consequences of cholinergic modulation, we examined the effect of carbachol (2 μM in the bath) on somatic firing patterns in the absence of TTX. Consistent with its effects on dendritic Ca^{2+}spikes, carbachol facilitated CSB firing in response to both somatic I_{inj} and synaptic stimulation via 2PGU on clustered spines located on apical dendrites (**Fig. 21C-F**). To avoid activation of confounding NMDA spikes, these experiments were performed in the continuous presence of an NMDAR blocker in the bath (D-AP5, 50 μM).

The CSBs triggered by carbachol were eliminated by the L-type VGCC inhibitor nifedipine (10 μM), confirming that L-type VGCCs mediate the observed cholinergic effects on Ca^{2+} spike kinetics and CSB firing (**Fig. 21G)**.

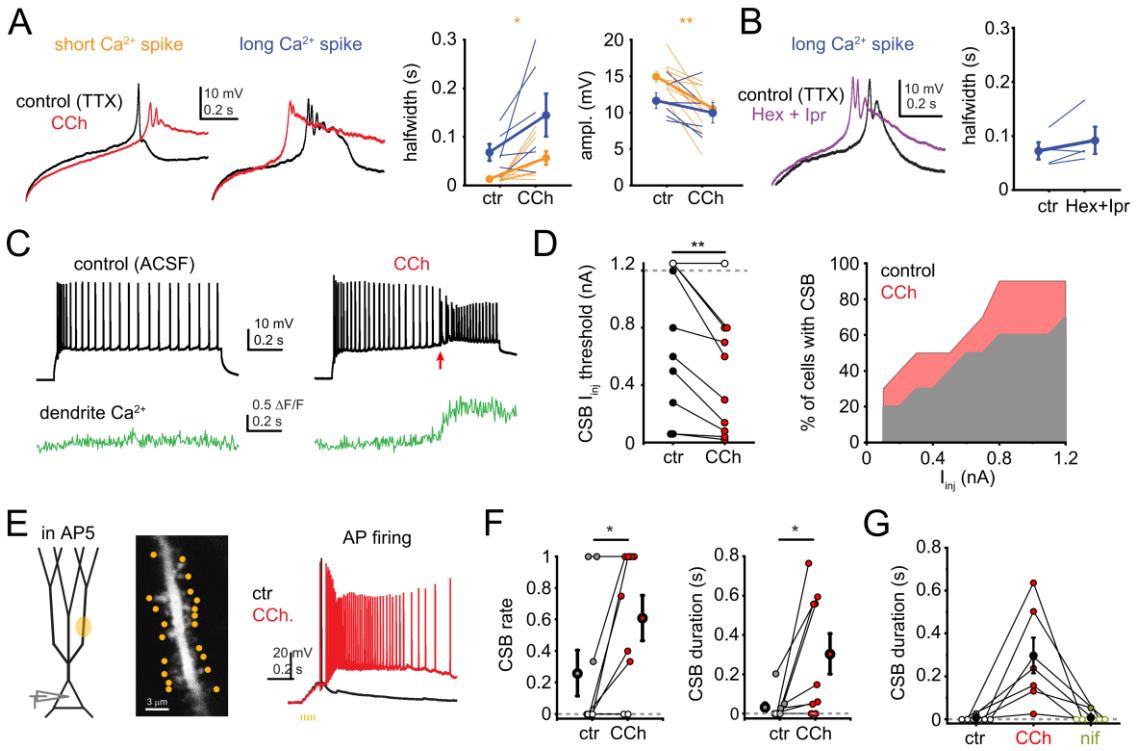

Figure 21. Cholinergic modulation of Ca^{2+} spike kinetics and CSBs. ***(A)*** *Representative Ca^{2+} spikes in TTX, before (black) and after bath application of 2 µM CCh (red). Right panels: summary of CCh's effect on short (orange, n = 9) and long-lasting (blue, n = 6) spikes (*P < 0.05, **P < 0.01, Wilcoxon test).* ***(B)*** *Left: example long Ca^{2+} spike in TTX (black) and after the application of 100 µM hexamethonium- and 10 µM ipratropium bromide (purple). Right: summary effect on long Ca^{2+} spike properties.* ***(C)*** *Example recording in ACSF, showing somatic firing patterns (top) and distal dendritic Ca^{2+} signals (bottom) before (left) and after (right) CCh application.* ***(D)*** *CCh effect on CSB threshold (left) and occurrence (right) (P < 0.01, Wilcoxon test). Lines connect data from the same cells. Filled symbols indicate CSB generation, open symbols indicate failure to evoke CSB at up to 1.2 nA I_{inj}. Right: proportion of CA3PCs (n = 10) generating CSBs in control (gray) and in CCh (red).* ***(E)*** *Effect of CCh on firing pattern, evoked by synaptic stimulation. Left: schematic of 2PGU experiment. Middle: single frame scan indicating the stimulated 20 synapses (yellow dots). Right: example suprathreshold voltage traces to 2PGU (20 spines stimulated quasi-synchronously 5x@40 Hz) under control conditions (black) and in the presence of CCh (red).* ***(F)*** *CCh effect on CSB rate (left) and duration (right) in response to 2PGU stimulation (n=9 cells). White dots: no CSB; grey dots: CSB in control; red dots: CSB in CCh (*p<0.05, Wilcoxon test).* ***(G)*** *CSB duration with CCh*

and CCh + nifedipine (n=7 cells). White dots: no CSB; colored dots: CSB. Filled black circles and error bars represent mean ± SEM (Kis et al., 2024).

Finally, to determine whether endogenous acetylcholine release could induce similar effects, we employed optogenetic stimulation of cholinergic axons in a transgenic mouse line (ChAT-Cre/Ai32) expressing ChR2-eYFP under the choline acetyltransferase (ChAT) promoter.

Since all of our previous work was conducted in slices from rats, we first compared Ca^{2+} spike properties and CSBs in wild-type mice (FVB/AntJ) to that in rats. We found that CA3PCs showed qualitatively similar (although less pronounced) heterogeneity in Ca^{2+} spike kinetics to rat CA3PCs (**Fig. 22A-C**), with both short- and long-duration Ca^{2+} spikes.

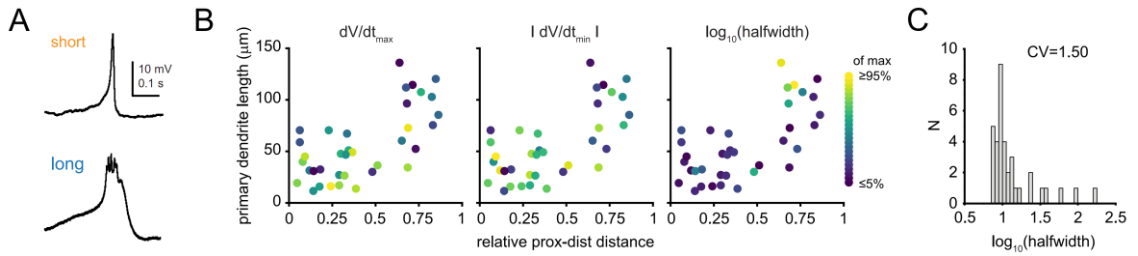

Figure 22. Different types of Ca^{2+} spikes in mice. (A) *Example short and long-lasting Ca^{2+} spike evoked by I_{inj} in two CA3PCs from wild type FVB/AntJ mice.* ***(B)*** *Distribution of various Ca^{2+} spike parameters (color-coded based on the parameters indicated on top) depending on proximodistal position and apical trunk length of mouse CA3PCs.* ***(C)*** *Histogram of the log_{10}(halfwidth) values (Kis et al., 2024).*

Examining the distribution of cholinergic axons in the ChAT-Cre/Ai32 mouse line (enhanced with immunostaining), we observed robust eYFP+ axonal innervation around the perisomatic region of CA3PCs (**Fig. 23A**), consistent with earlier reports (Aznavour et al., 2002; Grybko et al., 2011; Hunt et al., 2018). Using phasic photostimulation of cholinergic fibers (similar to Hunt et al., 2018) for 8 seconds before, and during somatic I_{inj}, we observed a significant increase in CSB rate and duration, along with an elevated steady-state AP frequency at comparable membrane potentials (**Fig. 23B and C**).

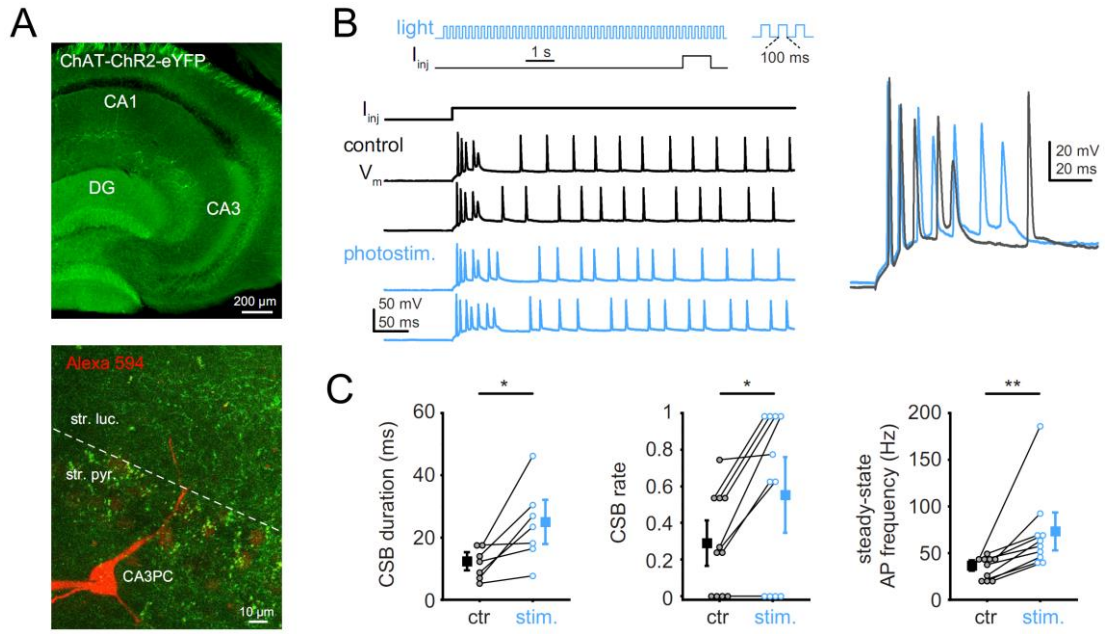

Figure 23. Optogenetic activation of cholinergic fibers in CA3PCs. (A) *Top: widefield fluorescent image showing ChR2-eYFP expression in the CA3 region of ChAT-Cre/Ai32 mice. Bottom: 2P Z-stack of a patched CA3PC loaded with Alexa Fluor 594 (red) surrounded by eYFP-ChR2-positive cholinergic axons (green).* ***(B)*** *Top left: experimental protocol combining photostimulation with somatic I_{inj}. Bottom: representative voltage responses of a CA3PC to somatic I_{inj} alone (black) and with light stimulation (blue) of ChR2-expressing axons. Right: overlayed traces highlight the increase in CSB duration with photostimulation.* ***(C)*** *Summary of the effects of stimulation on CSB duration (left, n = 7 cells with CSBs, *P < 0.05, Wilcoxon test), CSB rate (middle, n = 11, *P < 0.05, Wilcoxon test) and AP frequency during steady-state firing at 400–600 ms of the depolarization step (right, n = 10, **P < 0.01, Wilcoxon test) (Kis et al., 2024).*

These findings highlight that cholinergic activity regulates CSB rate and duration in CA3PCs by modulating Ca^{2+} spike kinetics. The transformation of short Ca^{2+} spikes into prolonged plateau-like events suggests a state-dependent mechanism for switching CA3PCs from a regular spiking mode to one characterized by sustained plateau potentials and CSBs. This mechanism may promote synaptic plasticity and rapid memory encoding, particularly in CA3PCs predisposed to short Ca^{2+} spikes under baseline conditions.

5. DISCUSSION

Understanding the mechanisms of dendritic integration and synaptic processing in hippocampal CA3PCs is crucial for elucidating their role in memory encoding and retrieval. Previous studies have provided some evidence for complex dendritic computations in CA3PCs, including the generation of dendritic Ca^{2+} spikes. However, the properties of these spikes and in general the diversity in dendritic integration mechanisms across different CA3PC subtypes remained poorly understood.

This thesis focused on investigating the mechanisms of dendritic Ca^{2+} spike and CSB generation in CA3PCs, the morphological and functional heterogeneity across the CA3 subregions, and the modulatory effects of cholinergic signaling. Using a combination of somatic, dendritic and dual soma-dendritic patch-clamp recordings, along with 2P Ca^{2+} imaging, we examined CSBs and Ca^{2+} spikes.

Our findings reveal diversity in dendritic spike mechanisms across CA3PC subtypes, with differential propensities for CSB generation and distinct ion channel contributions shaping these properties. These results suggest that CA3PCs contribute to hippocampal computations in a more complex and heterogeneous manner than previously assumed, with implications for learning, plasticity, and network dynamics.

5.1. CSB heterogeneity in the CA3

Previous studies in CA1 and L5 PCs have shown that certain spatiotemporal synaptic input patterns trigger dendritic Ca^{2+} spikes that can potentially contribute to associative cellular learning mechanisms (Bittner et al., 2015; Larkum et al., 2009; Stuart and Spruston, 2015; Takahashi and Magee, 2009). These findings demonstrate that Ca^{2+} spikes, together with NMDARs, generate dendritic plateau potentials, sustaining slow afterdepolarization at the soma, producing CSBs. The most effective excitatory synaptic input pattern for CSB induction in CA1 and L5 PCs involves the convergence of proximal and strong distal apical inputs, integrating local and long-range afferent activity (Bittner et al., 2015; Larkum, 2013). On the other hand, somatic depolarization alone is typically not effective to trigger CSBs. In CA3PCs, we examined whether CSB generation follows the same scheme and identified both similarities and differences. Like CA1, dendritic (primarily Ca^{2+}) spikes drive CSBs in CA3PCs. However, we found that CSB propensity varies among the CA3PC population, including CSB_H, CSB_L, and RS cells. CSB propensity varied along the proximodistal CA3 axis, with distal CA3PCs exhibiting

higher CSB rates, consistent with previous findings on CA3 burst firing (Hunt et al., 2018; Marissal et al., 2012; Masukawa et al., 1982; Oliva et al., 2016). Additionally, radial position played a role, as deep-layer distal CA3PCs exhibited the highest CSB propensity. Interestingly, this topographic pattern is consistent with developmental findings showing that hippocampal PCs are generated in an inside-out pattern, whereby early-born neurons settle in deeper layers and later-born cells migrate past them to occupy more superficial positions (Li et al., 2009; Soltesz and Losonczy, 2018). In the CA3 region, early-born cells preferentially localize to deep CA3a-b and tend to fire in bursts (Marissal et al., 2012). Thus, the embryonic birthdate and resulting radial positioning may contribute to the functional heterogeneity of CA3PCs.

5.2. Different types of dendritic Ca^{2+} spikes

Using dual soma-dendritic and single-site dendritic patch-clamp recordings in CA3PCs, we identified two distinct forms of Ca^{2+} spikes – ADP-type spikes and DI spikes – that differentially influence neuronal firing patterns. ADP-type spikes, which resemble previously described global Ca^{2+} spikes in other PCs, were longer lasting in CA3PCs (on average approximately threefold) than in CA1PCs and typically promoted somatic burst firing. These slow Ca^{2+} spikes appear globally throughout the apical (or even the whole) dendritic arbor, and they are most prevalent in CA3PCs with relatively long single primary trunks, consistent with the higher CSB propensity of deep distal CA3PCs. Although their precise origin remains uncertain, whether they are evoked as a 'global' dendritic spike (Connelly et al., 2015) or they have a specific generation zone from where they invade the arbor. The results suggest that the long primary apical trunk may act as a specialized generation site for slow Ca^{2+} spikes, but it is also possible that this dendritic trait simply correlates with other features (possibly including passive and/or active ion channel-mediated dendritic properties) that promote slow spike generation.

In contrast, DI spikes were much faster, spatially restricted, and triggered strictly a single APs followed by pronounced AHP, effectively preventing burst firing. This suggests that certain CA3PCs do not merely lack burst-promoting mechanisms but actively generate DI spikes to enforce a regular spiking phenotype. From another perspective, DI spikes may amplify specific local apical synaptic inputs in the absence of strong perisomatic activity (i.e., without bAPs) to promote neuronal output.

Another interesting feature of DI spikes is their semi-compartmentalization: they propagate efficiently within higher-order dendritic trunks but fail to propagate to other dendritic subtrees. This suggests that dendritic subtrees function as independent computational units for synaptic integration and plasticity. This reflects a 'mesoscale' level of compartmentalization that is between global and local branch specific dendritic spikes. DI spikes may promote localized synaptic or intrinsic (Losonczy et al., 2008) plasticity within a dendritic subtree, as the resulting single APs are unlikely to affect distant branches.

Interestingly, a subset of CA3PCs exhibited both slow and fast Ca^{2+} spikes, further increasing the complexity of their input-output transformations. The relative contribution of each spike type likely depends on the spatiotemporal pattern of activity of the three different sources of afferent synaptic inputs (MF, RC, and EC).

The DI spikes observed in rat CA3PCs resemble the dendritic Ca^{2+} spikes (called dCaAPs) recently reported in layer 2/3 PCs of the human neocortex, studied in tissue from epilepsy or tumor patients (Gidon et al., 2020). Although there were minor differences in amplitude, both the kinetics and the inverse relationship between spike amplitude and membrane depolarization were similar. Our findings contradict the idea that DI spikes would have developed specifically to support computational functions in the human cortex. Instead, DI spikes may participate in basic circuit computation motifs common to both hippocampal CA3 and superficial cortical PCs, for example, related to their intermediate position in a sequential chain of input processing (Shepherd, 2011). Their presence in healthy rat PCs also suggests a physiological role, rather than one associated with disease or treatment effects.

Our findings demonstrate unique diversity of dendritic computation in CA3PCs and suggest that distinct subpopulations of PCs may be specialized for different information processing functions. Future research should explore how different spike types summarize at the soma and contribute to network computations such as pattern separation and pattern completion during spatial navigation and memory processing.

5.3. Compound Ca^{2+} spikes

Evoking compound Ca^{2+} spikes by widespread somatic depolarization revealed that many CA3PCs exhibit combination of slow and fast Ca^{2+} spike components suggesting possible dendritic heterogeneity. However, a large subset of cells showed short, uniform

compound Ca^{2+} spikes (~10 ms), suggesting largely homogeneous fast Ca^{2+} spikes expressed in their dendrites. This diversity may stem from differences in ion channel expression and interaction dynamics.

The electrophysiological phenotype strongly correlated with morpho-topographic features: CA3PCs with short Ca^{2+} spikes are mostly located in proximal CA3 and superficial layers of distal CA3. These cells tended to have shorter and often multiple primary apical trunks, extensive dendritic arborization, and dense TEs. Under baseline conditions, these CA3PCs typically have low propensity to fire CSBs and when they do, the CSBs are brief, consistent with their short-duration Ca^{2+} spikes.

Pharmacological experiments indicated that L-type VGCCs play a dominant role in generating both short- and long Ca^{2+} spikes, aligning with their relatively high voltage threshold and the low expression of Cav2.3 (mediating R-type VGCCs) in CA3PCs (Parajuli et al., 2012). N-type Ca^{2+} channels had a minor role, as their blocker moderately reduced short Ca^{2+} spikes. It is still possible that distinct Cav1 subunits or their cell subtype-dependent regulation contributes to the varieties of Ca^{2+} spikes (Zhou et al., 2004). Our data suggests that differences in K_A and K_M currents (mediated by members of Kv4 and Kv7 channel families, respectively) are primarily responsible for the differences between the two main Ca^{2+} spike forms. This aligns with expression patterns of Kv7.5 channel subunit in CA3PCs (Tzingounis et al., 2010), particularly in superficial cell layers (Thompson et al., 2008), and of Kv4.2 and Kv4.3 that are expressed in moderate to high densities in CA3PC dendrites (Rhodes et al., 2004).

5.4. Cholinergic regulation of Ca^{2+} spikes and CSBs

We found that cholinergic activation prolongs short compound Ca^{2+} spikes converting them into long-lasting forms, promoting sustained CSB firing that may effectively induce synaptic plasticity (Li et al., 2024; Takahashi and Magee, 2009), suggesting a state-dependent dendritic mechanism for memory encoding and retrieval. ACh is released on a second-scale during exploration and salient experiences (Lovett-Barron et al., 2014; Zhang et al., 2021), which are typically associated with learning. Elevated ACh induces cellular, synaptic, and network changes in CA3 and it is thought to facilitate encoding of novel information over retrieval of previously stored patterns (Hasselmo, 2006). In CA1PCs ACh enhances dendritic excitability and Ca^{2+} signaling (Egorov and Müller, 1999; Tsubokawa and Ross, 1997) and facilitates Ca^{2+} spikes by

modulating K^+ conductances and R-type VGCCs (Benardo and Prince, 1982; Park and Spruston, 2012; Tai et al., 2006). Similar effects are seen in cortical L5PCs (Nuñez et al., 2012; Williams and Fletcher, 2019). While our results show that cholinergic agonists also increase bursting in CA3PCs, R-type channels are only weakly expressed in these neurons (Parajuli et al., 2012) and do not significantly contribute to dendritic Ca^{2+} spikes, suggesting that different mechanisms underlie cholinergic modulation in CA3.

5.5. Morpho-functional heterogeneity of CA3PCs

Together with previous findings, our results support a model where CA3PCs form a morpho-functionally diverse population with distinct topographic locations, morphologies, firing properties, and state-dependent regulation (Cembrowski and Spruston, 2019; Hunt et al., 2018; Lee et al., 2020). It is still unclear whether these differences represent a gradual spectrum or truly distinct subpopulations, and if the latter, how many groups exist. Hunt et al. (Hunt et al., 2018; Linaro et al., 2022) identified two groups: thorny and athorny PCs in juvenile rodents (mice and rats), distinguished by their TEs, morphology, transcriptomics and firing profiles. In contrast, all CA3PCs recorded in our adult rat dataset exhibited TEs, though at varying densities, associated with different primary dendritic morphologies, similar to previous studies in adult rats (Juraska et al., 1989). This discrepancy may reflect developmental changes, as TEs and dendritic structures undergo significant maturation and refinement with age. It is possible that athorny cells represent a transient developmental stage in younger animals that later develop into thorny PCs as they integrate into the CA3 network. Alternatively, some of the differences could also be attributed to species-specific factors (mice vs. rats) or variations in experimental conditions. Notably, while cholinergic stimulation suppressed bursting in athorny cells (Hunt et al., 2018) , we consistently observed a facilitation of CSBs under similar conditions.

Our findings support the existence of two main morpho-functional CA3PC subtypes, which may represent ends of a functional continuum and serve distinct computational roles. One subtype, primarily located in proximal CA3 and superficial distal CA3, shows low CSB propensity and brief Ca^{2+} spikes under baseline conditions. High ACh levels enable these neurons to generate long Ca^{2+} plateaus and CSBs, likely crucial for rapid synaptic plasticity and encoding of novel information. These cells receive strong MF input, consistent with the role of proximal CA3 in cooperation with the DG to form new

representations (Almeida et al., 2007; Hunsaker et al., 2008; Lee et al., 2015; Lu et al., 2015). ACh may enhance dendritic excitability to promote plateau generation and plasticity at stratum radiatum synapses, while suppressing recurrent inputs to reduce interference during memory encoding (Hasselmo, 2006). Notably, these CA3c neurons have also been implicated in pattern separation, likely through their tight interaction with the DG (GoodSmith et al., 2019; Lee et al., 2015). The second subtype, located deeper in distal CA3, appears more heterogeneous, receives less MF input, and generates longer Ca^{2+} spikes and CSBs even under low ACh condition. Many of these cells exhibit both fast and slow spike components, complicating predictions about their role in input–output transformation. These CA3a-b neurons may be particularly involved in pattern completion and SWR generation (Csicsvari et al., 2000; Lee et al., 2015; Lu et al., 2015; Oliva et al., 2016). It remains to be determined whether different inputs selectively trigger different spike types, and how short vs. long Ca^{2+} spikes support plasticity with or without cholinergic modulation. We propose that this variability allows dynamic switching between encoding and retrieval modes depending on the spike type.

While our slice experiments mimic elevated cholinergic tone, in vivo studies are needed to fully understand how natural ACh release shapes CA3PC activity. Overall, our study highlights the cellular diversity in CA3 and reveals distinct forms of Ca^{2+} spikes and their modulation by cholinergic activation.

6. CONCLUSIONS

This dissertation investigated the mechanisms underlying dendritic Ca^{2+} spikes and CSBs in CA3PCs, addressing key questions about their structural, functional, and neuromodulatory properties. The results demonstrate that:

1. CA3PCs exhibit a significantly higher CSB propensity compared to CA1PCs, with heterogeneity among individual cells, which can be categorized into CSB_H, CSB_L, and RS subtypes. This variability reflects diverse intrinsic properties and may be crucial for playing specific roles in recurrent network computations.
2. Two distinct forms of Ca^{2+} spikes were characterized in individual higher-order dendrites of CA3PCs: ADP and DI spikes. ADP spikes are slow, triggered by bAPs and promote somatic burst firing, whereas DI spikes are fast, arise independently of bAPs and generate only single APs.
3. Compound Ca^{2+} spikes measured at the soma exhibited large cell-to-cell variability and could be classified into short and long-duration forms. Long Ca^{2+} spikes could be further divided into simple and complex subtypes. The kinetics of Ca^{2+} spikes were closely linked to the bursting properties of CA3PCs: most cells with short Ca^{2+} spikes were RS or produced only brief CSBs, whereas long-duration Ca^{2+} spikes were associated with higher CSB propensity and sustained plateau potentials. The heterogeneity in compound Ca^{2+} spikes was related to proximodistal and radial positions as well as dendritic morphology. Ion channel mechanisms were found to play a central role in regulating these processes. Ca^{2+} spikes are mediated mainly by L-type Ca^{2+} channels and modulated by A- and M-type K^+ channels.
4. Cholinergic neuromodulation emerged as a critical regulator of dendritic and somatic activity. Pharmacologically or optogenetically enhanced cholinergic activity increased the duration of Ca^{2+} spikes converting short-duration events into prolonged plateau potentials, and thereby facilitated firing of prolonged CSBs.

These findings highlight the remarkable diversity and adaptability of CA3PCs, which enable them to perform complex computations necessary for memory encoding, retrieval, and pattern separation in the hippocampus. By elucidating the cellular and molecular mechanisms underlying these processes, this work provides a deeper understanding of the CA3 region's critical role in hippocampal function.

7. SUMMARY

Hippocampal CA3PCs play a crucial role in memory encoding and retrieval. These neurons are known to exhibit prominent CSB firing activity, which has been proposed to serve as an important signal for robust intercellular communication and synaptic plasticity. However, the mechanisms underlying CSB generation in CA3PCs remain poorly understood.

To explore the generation mechanisms of CSBs and the properties of Ca^{2+} spikes, we performed somatic and dendritic patch-clamp recordings combined with two-photon Ca^{2+} imaging in acute hippocampal slices from male rats and mice. These techniques enabled detailed characterization of dendritic Ca^{2+} spikes and their influence on neuronal output. Pharmacological manipulations were used to dissect the roles of different subtypes of Ca^{2+} and K^+ channels in regulating Ca^{2+} spike generation. Additionally, pharmacological and optogenetic stimulation of cholinergic activity was employed to investigate neuromodulatory control over CSB activity.

Our findings reveal that CSBs in CA3PCs are driven by dendritic Ca^{2+} spikes, which exhibit remarkable heterogeneity across cells influenced by their topographic position and dendritic morphology. All spike forms were dominantly mediated by L-type Ca^{2+} channels. With dendritic recordings, we identified two distinct types of dendritic Ca^{2+} spikes in CA3PCs: ADP-type global Ca^{2+} spikes promoting CSB firing and a novel, fast Ca^{2+} spike type that is initiated independently of bAPs and drives single APs. At the soma, compound Ca^{2+} spikes varied in duration, with long-lasting Ca^{2+} spikes (~50 ms) supporting plateau potentials and short spikes (few ms long) failing to sustain prolonged depolarization. We revealed that the time course of short spikes is restricted by A- and M- type K^+ channels. Cholinergic activation via carbachol and optogenetic stimulation transformed short Ca^{2+} spikes into prolonged forms and enhanced CSB firing, indicating strong neuromodulatory control over dendritic excitability.

These results uncover the diversity in dendritic Ca^{2+} spike dynamics among CA3PCs. The ability of cholinergic inputs to modulate Ca^{2+} spike kinetics and CSB generation suggests a state-dependent mechanism for memory encoding and retrieval within the CA3 network. These findings provide new insights into how CA3 network dynamics support associative learning and may inform future research on therapeutic strategies for memory-related disorders.

8. REFERENCES

Almeida L De, Idiart M, Lisman JE. 2007. Memory retrieval time and memory capacity of the CA3 network: Role of gamma frequency oscillations. *Learn Mem* **14**:795–806. doi:10.1101/lm.730207

Amaral DG, Witter MP. 1989. The three-dimensional organization of the hippocampal formation: a review of anatomical data. *Neuroscience* **31**:571–591. doi:10.1016/0306-4522(89)90424-7

Andersen P, Bliss TVP, Skrede KK. 1971. Lamellar organization of hippocampal excitatory pathways. *Exp Brain Res* **13**:222–238. doi:10.1007/BF00234087

Ariav G, Polsky A, Schiller J. 2003. Submillisecond precision of the input-output transformation function mediated by fast sodium dendritic spikes in basal dendrites of CA1 pyramidal neurons. *J Neurosci* **23**:7750–7758. doi:10.1523/jneurosci.23-21-07750.2003

Avery RB, Johnston D. 1996. Multiple Channel Types Contribute to the Low-Voltage-Activated Calcium Current in Hippocampal CA3 Pyramidal Neurons. *J Neurosci* **16**:5567–5582. doi:10.1523/JNEUROSCI.16-18-05567.1996

Aznavour N, Mechawar N, Descarries L. 2002. Comparative analysis of cholinergic innervation in the dorsal hippocampus of adult mouse and rat: A quantitative immunocytochemical study. *Hippocampus* **12**:206–217. doi:10.1002/hipo.1108

Benardo LS, Prince DA. 1982. Ionic Mechanisms of Cholinergic Excitation in Mammalian Hippocampal Pyramidal Cells. *Brain Res* **249**:333–344.

Bilkey DK, Schwartzkroin PA. 1990. Variation in electrophysiology and morphology of hippocampal CA3 pyramidal cells. *Brain Res* **514**:77–83. doi:10.1016/0006-8993(90)90437-G

Bishop HI, Guan D, Bocksteins E, Parajuli LK, Murray KD, Cobb MM, Misonou H, Zito K, Foehring RC, Trimmer JS. 2015. Distinct cell-and layer-specific expression patterns and independent regulation of kv2 channel subtypes in cortical pyramidal neurons. *J Neurosci* **35**:14922–14942. doi:10.1523/JNEUROSCI.1897-15.2015

Bittner KC, Grienberger C, Vaidya SP, Milstein AD, Macklin JJ, Suh J, Tonegawa S, Magee JC. 2015. Conjunctive input processing drives feature selectivity in hippocampal CA1 neurons. *Nat Neurosci* **18**:1133–1142. doi:10.1038/nn.4062

Bittner KC, Milstein AD, Grienberger C, Romani S, Magee JC. 2017. Behavioral time scale synaptic plasticity underlies CA1 place fields. *Science (80-)* **357**:1033–1036. doi:10.1126/science.aan3846

Brandalise F, Carta S, Helmchen F, Lisman J, Gerber U. 2016. Dendritic NMDA spikes are necessary for timing-dependent associative LTP in CA3 pyramidal cells. *Nat Commun* **7**:1–9. doi:10.1038/ncomms13480

Buzsáki G. 2015. Hippocampal sharp wave-ripple: A cognitive biomarker for episodic memory and planning. *Hippocampus* **25**:1073–1188. doi:10.1002/hipo.22488

Cappaert NLM, Van Strien NM, Witter MP. 2015. Chapter 20 - Hippocampal Formation In: Paxinos G, editor. The Rat Nervous System (Fourth Edition). San Diego: Academic Press. pp. 511–573. doi:https://doi.org/10.1016/B978-0-12-374245-2.00020-6

Cembrowski MS, Spruston N. 2019. Heterogeneity within classical cell types is the rule: lessons from hippocampal pyramidal neurons. *Nat Rev Neurosci* **20**:193–204. doi:10.1038/s41583-019-0125-5

Cenquizca LA, Swanson LW. 2007. Spatial organization of direct hippocampal field CA1 axonal projections to the rest of the cerebral cortex. *Brain Res Rev* **56**:1–26. doi:10.1016/j.brainresrev.2007.05.002

Chevaleyre V, Siegelbaum SA. 2010. Strong CA2 pyramidal neuron synapses define a powerful disynaptic cortico-hippocampal loop. *Neuron* **66**:560–572. doi:10.1016/j.neuron.2010.04.013

Choe WJ, Messinger RB, Leach E, Eckle VS, Obradovic A, Salajegheh R, Jevtovic-Todorovic V, Todorovic SM. 2011. TTA-P2 is a potent and selective blocker of T-type calcium channels in rat sensory neurons and a novel antinociceptive agent. *Mol Pharmacol* **80**:900–910. doi:10.1124/mol.111.073205

Cobb SR, Davies CH. 2005. Cholinergic modulation of hippocampal cells and circuits.

J Physiol **562**:81–88. doi:10.1113/jphysiol.2004.076539

Connelly WM, Crunelli V, Errington AC. 2015. The global spike: Conserved dendritic properties enable unique ca2+ spike generation in low-threshold spiking neurons. *J Neurosci* **35**:15505–15522. doi:10.1523/JNEUROSCI.2740-15.2015

Corkin S. 1984. Lasting Consequences of Bilateral Medial Temporal Lobectomy: Clinical Course and Experimental Findings in H.M. *Semin Neurol*. doi:10.1055/s-2008-1041556

Csicsvari J, Hirase H, Mamiya A, Buzsá GR. 2000. Ensemble Patterns of Hippocampal CA3-CA1 Neurons during Sharp Wave-Associated Population Events multisynaptic hippocampal circuits (Amaral and Witter, 1989), processing of information occurs during macro-scopic oscillations (Buzsaki and Chrobak, 1995). St. *Neuron* **28**:585–594.

Dannenberg H, Young K, Hasselmo M. 2017. Modulation of hippocampal circuits by muscarinic and nicotinic receptors. *Front Neural Circuits* **11**:102. doi:10.3389/fncir.2017.00102

Dasari S, Gulledge AT. 2011. M1 and M4 receptors modulate hippocampal pyramidal neurons. *J Neurophysiol* **105**:779–792. doi:10.1152/jn.00686.2010

Delatour B, Witter MP. 2002. Projections from the parahippocampal region to the prefrontal cortex in the rat: evidence of multiple pathways. *Eur J Neurosci* **15**:1400–1407. doi:https://doi.org/10.1046/j.1460-9568.2002.01973.x

Ding L, Chen H, Diamantaki M, Coletta S, Preston-Ferrer P, Burgalossi A. 2020. Structural Correlates of CA2 and CA3 pyramidal cell activity in freely-moving mice. *J Neurosci* **40**:5797–5806. doi:10.1523/JNEUROSCI.0099-20.2020

Dreyfus FM, Tscherter A, Errington AC, Renger JJ, Shin HS, Uebele VN, Crunelli V, Lambert RC, Leresche N. 2010. Selective T-type calcium channel block in thalamic neurons reveals channel redundancy and physiological impact of ITwindow. *J Neurosci* **30**:99–109. doi:10.1523/JNEUROSCI.4305-09.2010

Duebel J, Marazova K, Sahel J-A. 2015. Optogenetics. *Curr Opin Ophthalmol* **26**:226–232. doi:10.1097/ICU.0000000000000140

Dvorak-Carbone H, Schuman EM. 1999. Long-Term Depression of Temporoammonic-CA1 Hippocampal Synaptic Transmission. *J Neurophysiol* **81**:1036–1044. doi:10.1152/jn.1999.81.3.1036

Egorov A V, Müller W. 1999. Subcellular muscarinic enhancement of excitability and Ca2+-signals in CA1-dendrites in rat hippocampal slice. *Neurosci Lett* **261**:77–80. doi:10.1016/s0304-3940(99)00007-5

Eichenbaum H. 2017. The role of the hippocampus in navigation is memory. *J Neurophysiol* **117**:1785–1796. doi:10.1152/jn.00005.2017

Eichenbaum H. 2013. What H.M. taught us. *J Cogn Neurosci* **25**:14–21. doi:10.1162/jocn_a_00285

Feria Pliego JA, Pedroarena CM. 2020. Kv1 potassium channels control action potential firing of putative GABAergic deep cerebellar nuclear neurons. *Sci Rep* **10**:1–13. doi:10.1038/s41598-020-63583-7

Fisher R, Johnston D. 1990. Differential modulation of single voltage-gated calcium channels by cholinergic and adrenergic agonists in adult hippocampal neurons. *J Neurophysiol* **64**:1291–1302. doi:10.1152/jn.1990.64.4.1291

Fisher RE, Gray R, Johnston D. 1990. Properties and Distribution of Single Voltage-Gated Calcium Channels in Adult Hippocampal Neurons. *J Neurophysiol* **64**:91–104. doi:10.1152/jn.1990.64.1.9

Fitch JM, Juraska JM, Washington LW. 1989. The dendritic morphology of pyramidal neurons in the rat hippocampal CA3 area. I. Cell types. *Brain Res* **479**:105–114. doi:10.1016/0006-8993(89)91340-1

Francioni V, Harnett MT. 2021. Rethinking Single Neuron Electrical Compartmentalization: Dendritic Contributions to Network Computation In Vivo. *Neuroscience*. doi:10.1016/j.neuroscience.2021.05.038

Furukawa T, Nukada T, Miura R, Ooga K, Honda M, Watanabe S, Koganesawa S, Isshiki T. 2005. Differential blocking action of dihydropyridine Ca2+ antagonists on a T-type Ca2+ channel (α1G) expressed in Xenopus oocytes. *J Cardiovasc Pharmacol* **45**:241–246. doi:10.1097/01.fjc.0000154374.88283.15

Furukawa T, Yamakawa T, Midera T, Sagawa T, Mori Y, Nukada T. 1999. Selectivities of dihydropyridine derivatives in blocking Ca(2+) channel subtypes expressed in Xenopus oocytes. *J Pharmacol Exp Ther* **291**:464–473.

Gähwiler BH, Brown DA. 1987. Muscarine affects calcium-currents in rat hippocampal pyramidal cells in vitro. *Neurosci Lett* **76**:301–306. doi:10.1016/0304-3940(87)90419-8

Gasparini S, Migliore M, Magee JC. 2004. On the initiation and propagation of dendritic spikes in CA1 pyramidal neurons. *J Neurosci* **24**:11046–11056. doi:10.1523/JNEUROSCI.2520-04.2004

Gidon A, Zolnik TA, Fidzinski P, Bolduan F, Papoutsi A, Poirazi P, Holtkamp M, Vida I, Larkum ME. 2020. Dendritic action potentials and computation in human layer 2/3 cortical neurons. *Science (80-)* **367**:83–87. doi:10.1126/science.aax6239

Golding NL, Jung HY, Mickus T, Spruston N. 1999. Dendritic calcium spike initiation and repolarization are controlled by distinct potassium channel subtypes in CA1 pyramidal neurons. *J Neurosci* **19**:8789–8798. doi:10.1523/jneurosci.19-20-08789.1999

Golding NL, Kath WL, Spruston N. 2001. Dichotomy of action-potential backpropagation in CA1 pyramidal neuron dendrites. *J Neurophysiol* **86**:2998–3010. doi:10.1152/jn.2001.86.6.2998

GoodSmith D, Lee H, Neunuebel JP, Song H, Knierim JJ. 2019. Dentate Gyrus Mossy Cells Share a Role in Pattern Separation with Dentate Granule Cells and Proximal CA3 Pyramidal Cells. *J Neurosci Off J Soc Neurosci* **39**:9570–9584. doi:10.1523/JNEUROSCI.0940-19.2019

Grienberger C, Chen X, Konnerth A. 2014. NMDA receptor-dependent multidendrite Ca2+ spikes required for hippocampal burst firing invivo. *Neuron* **81**:1274–1281. doi:10.1016/j.neuron.2014.01.014

Grybko MJ, Hahm ET, Perrine W, Parnes JA, Chick WS, Sharma G, Finger TE, Vijayaraghavan S. 2011. A transgenic mouse model reveals fast nicotinic transmission in hippocampal pyramidal neurons. *Eur J Neurosci* **33**:1786–1798.

doi:10.1111/j.1460-9568.2011.07671.x

Gulledge AT, Kampa BM, Stuart GJ. 2005. Synaptic integration in dendritic trees. *J Neurobiol* **64**:75–90. doi:10.1002/neu.20144

Guzman SJ, Schlögl A, Frotscher M, Jonas P. 2016. Synaptic mechanisms of pattern completion in the hippocampal CA3 network. *Science (80-)* **353**:1117–1123. doi:10.1126/science.aaf1836

Hablitz JJ, Johnston D. 1981. Endogenous nature of spontaneous bursting in hippocampal pyramidal neurons. *Cell Mol Neurobiol* **1**:325–334. doi:10.1007/BF00716267

Hájos N, Papp EC, Acsády L, Levey AI, Freund TF. 1998. Distinct interneuron types express m2 muscarinic receptor immunoreactivity on their dendrites or axon terminals in the hippocampus. *Neuroscience* **82**:355–376. doi:10.1016/s0306-4522(97)00300-x

Harnett MT, Xu NL, Magee JC, Williams SR. 2013. Potassium channels control the interaction between active dendritic integration compartments in layer 5 cortical pyramidal neurons. *Neuron* **79**:516–529. doi:10.1016/j.neuron.2013.06.005

Hasselmo ME. 2006. The role of acetylcholine in learning and memory. *Curr Opin Neurobiol* **16**:710–715. doi:10.1016/j.conb.2006.09.002

Hasselmo ME. 1999. Neuromodulation and the hippocampus: Memory function and dysfunction in a network simulation. *Prog Brain Res* **121**:3–18. doi:10.1016/s0079-6123(08)63064-2

Häusser M. 2014. Optogenetics: The age of light. *Nat Methods* **11**:1012–1014. doi:10.1038/nmeth.3111

Henze DA, Wittner L, Buzsáki G. 2002. Single granule cells reliably discharge targets in the hippocampal CA3 network in vivo. *Nat Neurosci* **5**:790–795. doi:10.1038/nn887

Hillyard DR, Monje VD, Mintz IM, Bean BP, Nadasdi L, Ramachandran J, Miljanich G, Azimi-Zoonooz A, McIntosh JM, Cruz LJ, Imperial JS, Olivera BM. 1992. A

new conus peptide ligand for mammalian presynaptic Ca2+ channels. *Neuron* **9**:69–77. doi:10.1016/0896-6273(92)90221-X

Hoffman DA, Johnston D. 1998. Downregulation of transient K+ channels in dendrites of hippocampal CA1 pyramidal neurons by activation of PKA and PKC. *J Neurosci Off J Soc Neurosci* **18**:3521–3528. doi:10.1523/JNEUROSCI.18-10-03521.1998

Hu W, Tian C, Li T, Yang M, Hou H, Shu Y. 2009. Distinct contributions of Nav1.6 and Nav1.2 in action potential initiation and backpropagation. *Nat Neurosci* **12**:996–1002. doi:10.1038/nn.2359

Hunsaker MR, Rosenberg JS, Kesner RP. 2008. The role of the dentate gyrus, CA3a,b, and CA3c for detecting spatial and environmental novelty. *Hippocampus* **18**:1064–1073. doi:10.1002/hipo.20464

Hunt DL, Linaro D, Si B, Romani S, Spruston N. 2018. A novel pyramidal cell type promotes sharp-wave synchronization in the hippocampus. *Nat Neurosci* **21**:985–995. doi:10.1038/s41593-018-0172-7

Ishizuka N, Cowan WM, Amaral DG. 1995. A quantitative analysis of the dendritic organization of pyramidal cells in the rat hippocampus. *J Comp Neurol* **362**:17–45. doi:10.1002/cne.903620103

Ishizuka N, Weber J, Amaral DG. 1990. Organization of intrahippocampal projections originating from CA3 pyramidal cells in the rat. *J Comp Neurol* **295**:580–623. doi:10.1002/cne.902950407

Johnston D, Hablitz JJ, Wilson WA. 1980. Voltage clamp discloses slow inward current in hippocampal burst-firing neurones. *Nature* **286**:391–393. doi:10.1038/286391a0

Juraska JM, Fitch JM, Washburne DL. 1989. The dendritic morphology of pyramidal neurons in the rat hippocampal CA3 area. II. Effects of gender and the environment. *Brain Res* **479**:115–119. doi:10.1016/0006-8993(89)91341-3

Kametani H, Kawamura H. 1990. Alterations in acetylcholine release in the rat hippocampus during sleep-wakefulness detected by intracerebral dialysis. *Life Sci* **47**:421–426. doi:10.1016/0024-3205(90)90300-G

Kaneda M, Oyama Y, Ikemoto Y, Akaike N. 1989. Blockade of the voltage-dependent sodium current in isolated rat hippocampal neurons by tetrodotoxin and lidocaine. *Brain Res* **484**:348–351. doi:10.1016/0006-8993(89)90379-X

Kellar KJ, Martino AM, Hall DP, Schwartz RD, Taylor RL. 1985. High-affinity binding of [3H]acetylcholine to muscarinic cholinergic receptors. *J Neurosci* **5**:1577–1582. doi:10.1523/jneurosci.05-06-01577.1985

Kerti K, Lorincz A, Nusser Z. 2012. Unique somato-dendritic distribution pattern of Kv4.2 channels on hippocampal CA1 pyramidal cells. *Eur J Neurosci* **35**:66–75. doi:10.1111/j.1460-9568.2011.07907.x

Kim S, Guzman SJ, Hu H, Jonas P. 2012. Active dendrites support efficient initiation of dendritic spikes in hippocampal CA3 pyramidal neurons. *Nat Neurosci* **15**:600–606. doi:10.1038/nn.3060

Kimm T, Bean BP. 2014. Inhibition of A-type potassium current by the peptide toxin SNX-482. *J Neurosci* **34**:9182–9189. doi:10.1523/JNEUROSCI.0339-14.2014

Kis N, Lükő B, Herédi J, Magó Á, Erlinghagen B, Ahmadi M, Raus Balind S, Irás M, Ujfalussy BB, Makara JK. 2024. Cholinergic regulation of dendritic Ca2+ spikes controls firing mode of hippocampal CA3 pyramidal neurons. *Proc Natl Acad Sci* **121**. doi:10.1073/pnas.2321501121

Kohara K, Pignatelli M, Rivest AJ, Jung H-Y, Kitamura T, Suh J, Frank D, Kajikawa K, Mise N, Obata Y, Wickersham IR, Tonegawa S. 2014. Cell type-specific genetic and optogenetic tools reveal hippocampal CA2 circuits. *Nat Neurosci* **17**:269–279. doi:10.1038/nn.3614

Kowalski J, Gan J, Jonas P, Pernía-Andrade AJ. 2016. Intrinsic membrane properties determine hippocampal differential firing pattern in vivo in anesthetized rats. *Hippocampus* **26**:668–682. doi:10.1002/hipo.22550

Larkum M. 2013. A cellular mechanism for cortical associations: an organizing principle for the cerebral cortex. *Trends Neurosci* **36**:141–151. doi:10.1016/j.tins.2012.11.006

Larkum ME, Nevian T, Sandier M, Polsky A, Schiller J. 2009. Synaptic integration in

tuft dendrites of layer 5 pyramidal neurons: A new unifying principle. *Science (80-)* **325**:756–760. doi:10.1126/science.1171958

Lazarewicz MT, Migliore M, Ascoli GA. 2002. A new bursting model of CA3 pyramidal cell physiology suggests multiple locations for spike initiation. *BioSystems* **67**:129–137. doi:10.1016/S0303-2647(02)00071-0

Lee H, GoodSmith D, Knierim JJ. 2020. Parallel processing streams in the hippocampus. *Curr Opin Neurobiol* **64**:127–134. doi:10.1016/j.conb.2020.03.004

Lee H, Wang C, Deshmukh SS, Knierim JJ. 2015. Neural Population Evidence of Functional Heterogeneity along the CA3 Transverse Axis: Pattern Completion versus Pattern Separation. *Neuron* **87**:1093–1105. doi:10.1016/j.neuron.2015.07.012

Lee I, Yoganarasimha D, Rao G, Knierim JJ. 2004. Comparison of population coherence of place cells in hippocampal subfields CA1 and CA3. *Nature* **430**:456–459. doi:10.1038/nature02739

Levey AI, Edmunds SM, Koliatsos V, Wiley RG, Heilman CJ. 1995. Expression of m1-m4 muscarinic acetylcholine receptor proteins in rat hippocampus and regulation by cholinergic innervation. *J Neurosci Off J Soc Neurosci* **15**:4077–4092. doi:10.1523/JNEUROSCI.15-05-04077.1995

Li Y, Briguglio JJ, Romani S, Magee JC. 2024. Mechanisms of memory-supporting neuronal dynamics in hippocampal area CA3. *Cell* **187**:6804-6819.e21. doi:10.1016/j.cell.2024.09.041

Li Y, Mu Y, Gage FH. 2009. Development of neural circuits in the adult hippocampus. *Curr Top Dev Biol* **87**:149–174. doi:10.1016/S0070-2153(09)01205-8

Linaro D, Levy MJ, Hunt DL. 2022. Cell type-specific mechanisms of information transfer in data-driven biophysical models of hippocampal CA3 principal neurons. *PLoS Comput Biol* **18**:e1010071. doi:10.1371/journal.pcbi.1010071

Lisman JE. 1997. Bursts as a unit of neural information: Making unreliable synapses reliable. *Trends Neurosci* **20**:38–43. doi:10.1016/S0166-2236(96)10070-9

London M, Häusser M. 2005. Dendritic computation. *Annu Rev Neurosci* **28**:503–532. doi:10.1146/annurev.neuro.28.061604.135703

Lorente de No R. 1934. Studies on the structure of the cerebral cortex XI Continuation of the study of the ammonic system. *J Psychol Neurol* **46**:113--177.

Lorincz A, Nusser Z. 2010. Molecular identity of dendritic voltage-gated sodium channels. *Science* **328**:906–909. doi:10.1126/science.1187958

Losonczy A, Magee JC. 2006. Integrative Properties of Radial Oblique Dendrites in Hippocampal CA1 Pyramidal Neurons. *Neuron* **50**:291–307. doi:10.1016/j.neuron.2006.03.016

Losonczy A, Makara JK, Magee JC. 2008. Compartmentalized dendritic plasticity and input feature storage in neurons. *Nature* **452**:436–441. doi:10.1038/nature06725

Lovett-Barron M, Kaifosh P, Kheirbek MA, Danielson N, Zaremba JD, Reardon TR, Turi GF, Hen R, Zemelman B V, Losonczy A. 2014. Dendritic inhibition in the hippocampus supports fear learning. *Science (80-)* **343**:857–863. doi:10.1126/science.1247485

Lu L, Igarashi KM, Witter MP, Moser EI, Moser MB. 2015. Topography of Place Maps along the CA3-to-CA2 Axis of the Hippocampus. *Neuron* **87**:1078–1092. doi:10.1016/j.neuron.2015.07.007

Maccaferri G, McBain CJ. 1995. Passive propagation of LTD to stratum oriens-alveus inhibitory neurons modulates the temporoammonic input to the hippocampal CA1 region. *Neuron* **15**:137–145. doi:10.1016/0896-6273(95)90071-3

Macvicar Brian A, Tse Frederick W Y, Macvicar B A, Tse F W Y. 1989. Local neuronal circuitry underlying cholinergic rhythmical slow activity in CA3 area of rat hippocampal slices. *J Physiol* **417**:197–212. doi:10.1113/jphysiol.1989.sp017797

Madeja M. 2000. Do neurons have a reserve of sodium channels for the generation of action potentials? A study on acutely isolated CA1 neurons from the guinea-pig hippocampus. *Eur J Neurosci* **12**:1–7. doi:10.1046/j.1460-9568.2000.00871.x

Magee JC, Carruth M. 1999. Dendritic voltage-gated ion channels regulate the action potential firing mode of hippocampal CA1 pyramidal neurons. *J Neurophysiol* **82**:1895–1901. doi:10.1152/jn.1999.82.4.1895

Magee JC, Johnston D. 1995. Characterization of single voltage-gated Na+ and Ca2+ channels in apical dendrites of rat CA1 pyramidal neurons. *J Physiol* **487**:67–90. doi:10.1113/jphysiol.1995.sp020862

Magó Á, Kis N, Lükő B, Makara JK. 2021. Distinct dendritic Ca2+ spike forms produce opposing input-output transformations in rat ca3 pyramidal cells. *Elife* **10**:1–21. doi:10.7554/eLife.74493

Major G, Polsky A, Denk W, Schiller J, Tank DW. 2008. Spatiotemporally graded NMDA spike/plateau potentials in basal dendrites of neocortical pyramidal neurons. *J Neurophysiol* **99**:2584–2601. doi:10.1152/jn.00011.2008

Makara JK, Magee JC. 2013. Variable dendritic integration in hippocampal CA3 pyramidal neurons. *Neuron* **80**:1438–1450. doi:10.1016/j.neuron.2013.10.033

Marissal T, Bonifazi P, Picardo MA, Nardou R, Petit LF, Baude A, Fishell GJ, Ben-Ari Y, Cossart R. 2012. Pioneer glutamatergic cells develop into a morpho-functionally distinct population in the juvenile CA3 hippocampus. *Nat Commun* **3**. doi:10.1038/ncomms2318

Marr D. 1971. Simple memory: a theory for archicortex. *Philos Trans R Soc Lond B Biol Sci* **262**:23–81. doi:10.1098/rstb.1971.0078

Martinello K, Huang Z, Lujan R, Tran B, Watanabe M, Cooper EC, Brown DA, Shah MM. 2015. Cholinergic afferent stimulation induces axonal function plasticity in adult hippocampal granule cells. *Neuron* **85**:346–363. doi:10.1016/j.neuron.2014.12.030

Masukawa LM, Benardo LS, Prince DA. 1982. Variations in electrophysiological properties of hippocampal neurons in different subfields. *Brain Res* **242**:341–344. doi:10.1016/0006-8993(82)90320-1

McIntyre CK, Marriott LK, Gold PE. 2003. Patterns of brain acetylcholine release predict individual differences in preferred learning strategies in rats. *Neurobiol*

Learn Mem **79**:177–183. doi:10.1016/S1074-7427(02)00014-X

McNaughton BL, Morris RGM. 1987. Hippocampal synaptic enhancement and information storage within a distributed memory system. *Trends Neurosci* **10**:408–415. doi:10.1016/0166-2236(87)90011-7

Mineur YS, Picciotto MR. 2023. How can I measure brain acetylcholine levels in vivo? Advantages and caveats of commonly used approaches. *J Neurochem* **167**:3–15. doi:10.1111/jnc.15943

Mishra SK, Hermsmeyer K. 1994. Selective inhibition of T-type Ca2+ channels by Ro 40-5967. *Circ Res* **75**:144–148. doi:10.1161/01.RES.75.1.144

Mizuseki K, Royer S, Diba K, Buzsáki G. 2012. Activity dynamics and behavioral correlates of CA3 and CA1 hippocampal pyramidal neurons. *Hippocampus* **22**:1659–1680. doi:10.1002/hipo.22002

Mogul DJ, Fox AP. 1991. Evidence for multiple types of Ca2+ channels in acutely isolated hippocampal CA3 neurones of the guinea-pig. *J Physiol* **433**:259–281. doi:10.1113/jphysiol.1991.sp018425

Murakoshi H, Trimmer JS. 1999. Identification of the Kv2.1 K+ channel as a major component of the delayed rectifier K+ current in rat hippocampal neurons. *J Neurosci* **19**:1728–1735. doi:10.1523/jneurosci.19-05-01728.1999

Nail-Boucherie K, Dourmap N, Jaffard R, Costentin J. 2000. Contextual fear conditioning is associated with an increase of acetylcholine release in the hippocampus of rat. *Cogn Brain Res* **9**:193–197. doi:10.1016/S0926-6410(99)00058-0

Nakajima Y, Nakajima S, Leonard RJ, Yamaguchi K. 1986. Acetylcholine raises excitability by inhibiting the fast transient potassium current in cultured hippocampal neurons. *Proc Natl Acad Sci U S A* **83**:3022–3026. doi:10.1073/pnas.83.9.3022

Newcomb R, Szoke B, Palma A, Wang G, Chen XH, Hopkins W, Cong R, Miller J, Urge L, Tarczy-Hornoch K, Loo JA, Dooley DJ, Nadasdi L, Tsien RW, Lemos J, Miljanich G. 1998. Selective peptide antagonist of the class E calcium channel

from the venom of the tarantula Hysterocrates gigas. *Biochemistry* **37**:15353–15362. doi:10.1021/bi981255g

Nuñez A, Buño W. 1992. Intracellular effects of QX-314 and Cs+ in hippocampal pyramidal neurons in vivo. *Exp Neurol* **115**:266–270. doi:10.1016/0014-4886(92)90061-T

Nuñez A, Domínguez S, Buño W, Sevilla DF De. 2012. Cholinergic-mediated response enhancement in barrel cortex layer V pyramidal neurons. *J Neurophysiol* **108**:1656–1668. doi:10.1152/jn.00156.2012.-Neocortical

O'Keefe J, Conway DH. 1978. Hippocampal place units in the freely moving rat: why they fire where they fire. *Exp brain Res* **31**:573–590. doi:10.1007/BF00239813

O'Keefe J, Dostrovsky J, J O, J D, O'Keefe J, Dostrovsky J, J. O'Keefe JD. 1971. The hippocampus as a spatial map. Preliminary evidence from unit activity in the freely-moving rat. *Brain Res* **34**:171–175. doi:10.1016/0006-8993(71)90358-1

Oliva A, Fernández-Ruiz A, Buzsáki G, Berényi A. 2016. Spatial coding and physiological properties of hippocampal neurons in the Cornu Ammonis subregions. *Hippocampus* **26**:1593–1607. doi:10.1002/hipo.22659

Palacio S, Chevaleyre V, Brann DH, Murray KD, Piskorowski RA, Trimmer JS. 2017. Heterogeneity in Kv2 channel expression shapes action potential characteristics and firing patterns in CA1 versus CA2 hippocampal pyramidal neurons. *eNeuro* **4**:1–12. doi:10.1523/ENEURO.0267-17.2017

Palacios-Filardo J, Mellor JR. 2019. Neuromodulation of hippocampal long-term synaptic plasticity. *Curr Opin Neurobiol* **54**:37–43. doi:10.1016/j.conb.2018.08.009

Parajuli LK, Nakajima C, Kulik A, Matsui K, Schneider T, Shigemoto R, Fukazawa Y. 2012. Quantitative regional and ultra structural localization of the Ca v2.3 subunit of R-type calcium channel in mouse brain. *J Neurosci* **32**:13555–13567. doi:10.1523/JNEUROSCI.1142-12.2012

Park JY, Spruston N. 2012. Synergistic actions of metabotropic acetylcholine and glutamate receptors on the excitability of hippocampal CA1 pyramidal neurons. *J*

Neurosci **32**:6081–6091. doi:10.1523/JNEUROSCI.6519-11.2012

Peng H, Bria A, Zhou Z, Iannello G, Long F. 2014. Extensible visualization and analysis for multidimensional images using Vaa3D. *Nat Protoc* **9**:193–208. doi:10.1038/nprot.2014.011

Peng H, Ruan Z, Long F, Simpson JH, Myers EW. 2010. V3D enables real-time 3D visualization and quantitative analysis of large-scale biological image data sets. *Nat Biotechnol* **28**:348–353. doi:10.1038/nbt.1612

Pepeu G, Giovannini MG. 2004. Changes in acetylcholine extracellular levels during cognitive processes. *Learn Mem* **11**:21–27. doi:10.1101/lm.68104

Prince LY, Bacon TJ, Tigaret CM, Mellor JR. 2016. Neuromodulation of the feedforward dentate gyrus-CA3 microcircuit. *Front Synaptic Neurosci* **8**:32. doi:10.3389/fnsyn.2016.00032

Ranck JB. 1973. Studies on single neurons in dorsal hippocampal formation and septum in unrestrained rats. Part I. Behavioral correlates and firing repertoires. *Exp Neurol* **41**:462–531. doi:10.1016/0014-4886(73)90290-2

Raus Balind S, Magó Á, Ahmadi M, Kis N, Varga-Németh Z, Lőrincz A, Makara JK. 2019. Diverse synaptic and dendritic mechanisms of complex spike burst generation in hippocampal CA3 pyramidal cells. *Nat Commun* **10**. doi:10.1038/s41467-019-09767-w

Rhodes KJ, Carroll KI, Sung MA, Doliveira LC, Monaghan MM, Burke SL, Strassle BW, Buchwalder L, Menegola M, Cao J, An WF, Trimmer JS. 2004. KChIPs and Kv4 α subunits as integral components of A-type potassium channels in mammalian brain. *J Neurosci* **24**:7903–7915. doi:10.1523/JNEUROSCI.0776-04.2004

Rolls ET. 2013. The mechanisms for pattern completion and pattern separation in the hippocampus. *Front Syst Neurosci* **7**:1–21. doi:10.3389/fnsys.2013.00074

Sah P, Faber ESL. 2002. Channels underlying neuronal calcium-activated potassium currents. *Prog Neurobiol* **66**:345–353. doi:10.1016/S0301-0082(02)00004-7

Sammons RP, Vezir M, Moreno-Velasquez L, Cano G, Orlando M, Sievers M, Grasso E, Metodieva VD, Kempter R, Schmidt H, Schmitz D. 2024. Structure and function of the hippocampal CA3 module. *Proc Natl Acad Sci* **121**:e2312281120. doi:10.1073/pnas.2312281120

Schiller D, Eichenbaum H, Buffalo EA, Davachi L, Foster DJ, Leutgeb S, Ranganath C. 2015. Memory and space: Towards an understanding of the cognitive map. *J Neurosci* **35**:13904–13911. doi:10.1523/JNEUROSCI.2618-15.2015

Schiller J, Schiller Y, Stuart G, Sakmann B. 1997. Calcium action potentials restricted to distal apical dendrites of rat neocortical pyramidal neurons. *J Physiol* **505**:605–616. doi:10.1111/j.1469-7793.1997.605ba.x

Scoville WB, Milner B. 2000. Loss of recent memory after bilateral hippocampal lesions. 1957. *J Neuropsychiatry Clin Neurosci* **12**:103–113. doi:10.1176/jnp.12.1.103

Shepherd GM. 2011. The microcircuit concept applied to cortical evolution: From three-layer to six-layer cortex. *Front Neuroanat* **5**:1–15. doi:10.3389/fnana.2011.00030

Simms BA, Zamponi GW. 2014. Neuronal voltage-gated calcium channels: Structure, function, and dysfunction. *Neuron* **82**:24–45. doi:10.1016/j.neuron.2014.03.016

Solari N, Hangya B. 2018. Cholinergic modulation of spatial learning, memory and navigation. *Eur J Neurosci* **48**:2199–2230. doi:10.1111/ejn.14089

Soltesz I, Losonczy A. 2018. CA1 pyramidal cell diversity enabling parallel information processing in the hippocampus. *Nat Neurosci* **21**:484–493. doi:10.1038/s41593-018-0118-0

Spruston N. 2008. Pyramidal neurons: Dendritic structure and synaptic integration. *Nat Rev Neurosci* **9**:206–221. doi:10.1038/nrn2286

Stuart GJ, Spruston N. 2015. Dendritic integration: 60 years of progress. *Nat Neurosci* **18**:1713–1721. doi:10.1038/nn.4157

Stuyt G, Godenzini L, Palmer LM. 2021. Local and Global Dynamics of Dendritic

Activity in the Pyramidal Neuron. *Neuroscience*. doi:10.1016/j.neuroscience.2021.07.008

Sun Q, Sotayo A, Cazzulino AS, Snyder AM, Denny CA, Siegelbaum SA. 2017. Proximodistal Heterogeneity of Hippocampal CA3 Pyramidal Neuron Intrinsic Properties, Connectivity, and Reactivation during Memory Recall. *Neuron* **95**:656-672.e3. doi:10.1016/j.neuron.2017.07.012

Sun Q, Srinivas K V, Sotayo A, Siegelbaum SA. 2014. Dendritic Na+ spikes enable cortical input to drive action potential output from hippocampal CA2 pyramidal neurons. *Elife* **3**:1–24. doi:10.7554/eLife.04551

Tai C, Kuzmiski JB, MacVicar BA. 2006. Muscarinic enhancement of R-type calcium currents in hippocampal CA1 pyramidal neurons. *J Neurosci* **26**:6249–6258. doi:10.1523/JNEUROSCI.1009-06.2006

Takahashi H, Magee JC. 2009. Pathway Interactions and Synaptic Plasticity in the Dendritic Tuft Regions of CA1 Pyramidal Neurons. *Neuron* **62**:102–111. doi:10.1016/j.neuron.2009.03.007

Tanabe M, Gähwiler BH, Gerber U. 1998. L-type Ca2+ channels mediate the slow Ca2+-dependent afterhyperpolarization current in rat CA3 pyramidal cells in vitro. *J Neurophysiol* **80**:2268–2273. doi:10.1152/jn.1998.80.5.2268

Thompson CL, Pathak SD, Jeromin A, Ng LL, MacPherson CR, Mortrud MT, Cusick A, Riley ZL, Sunkin SM, Bernard A, Puchalski RB, Gage FH, Jones AR, Bajic VB, Hawrylycz MJ, Lein ES. 2008. Genomic Anatomy of the Hippocampus. *Neuron* **60**:1010–1021. doi:10.1016/j.neuron.2008.12.008

Traub RD, Jefferys JGR, Miles R, Whittington MA, Tóth K. 1994. A branching dendritic model of a rodent CA3 pyramidal neurone. *J Physiol* **481**:79–95. doi:10.1113/jphysiol.1994.sp020420

Tsubokawa H, Ross WN. 1997. Muscarinic Modulation of Spike Backpropagation in the Apical Dendrites of Hippocampal CA1 Pyramidal Neurons. *J Neurosci* **17**:5782–5791. doi:10.1523/JNEUROSCI.17-15-05782.1997

Tzingounis A V, Heidenreich M, Kharkovets T, Spitzmaul G, Jensen HS, Nicoll RA,

Jentsch TJ. 2010. The KCNQ5 potassium channel mediates a component of the afterhyperpolarization current in mouse hippocampus. *Proc Natl Acad Sci U S A* **107**:10232–10237. doi:10.1073/pnas.1004644107

van Strien NM, Cappaert NLM, Witter MP. 2009. The anatomy of memory: an interactive overview of the parahippocampal-hippocampal network. *Nat Rev Neurosci* **10**:272–282. doi:10.1038/nrn2614

Vyleta NP, Borges-Merjane C, Jonas P. 2016. Plasticity-dependent, full detonation at hippocampal mossy fiber-CA3 pyramidal neuron synapses. *Elife* 5:e17977. doi:10.7554/eLife.17977.001

Waters J, Schaefer A, Sakmann B. 2005. Backpropagating action potentials in neurones: Measurement, mechanisms and potential functions. *Prog Biophys Mol Biol* **87**:145–170. doi:10.1016/j.pbiomolbio.2004.06.009

Watson JF, Vargas-Barroso V, Jonas P. 2024. Cell-specific wiring routes information flow through hippocampal CA3. *bioRxiv*. doi:10.1101/2024.06.24.600436

Williams SR, Fletcher LN. 2019. A Dendritic Substrate for the Cholinergic Control of Neocortical Output Neurons. *Neuron* **101**:486-499.e4. doi:10.1016/j.neuron.2018.11.035

Williams SR, Stuart GJ. 1999. Mechanisms and consequences of action potential burst firing in rat neocortical pyramidal neurons. *J Physiol* **521**:467–482. doi:10.1111/j.1469-7793.1999.00467.x

Witter MP. 2007. Intrinsic and extrinsic wiring of CA3: Indications for connectional heterogeneity. *Learn Mem* **14**:705–713. doi:10.1101/lm.725207

Witter MP. 1993. Organization of the entorhinal-hippocampal system: a review of current anatomical data. *Hippocampus* **3 Spec No**:33–44.

Wong RKS, Prince DA. 1978. Participation of calcium spikes during intrinsic burst firing in hippocampal neurons. *Brain Res* **159**:385–390. doi:10.1016/0006-8993(78)90544-9

Wong RKS, Prince DA, Basbaum AI. 1979. Intradendritic recordings from

hippocampal neurons. *Proc Natl Acad Sci U S A* **76**:986–990. doi:10.1073/pnas.76.2.986

Yamamura HI, Snyder SH. 1974. Muscarinic cholinergic binding in rat brain. *Proc Natl Acad Sci U S A* **71**:1725–1729. doi:10.1073/pnas.71.5.1725

Yao Z, van Velthoven CTJ, Nguyen TN, Goldy J, Sedeno-Cortes AE, Baftizadeh F, Bertagnolli D, Casper T, Chiang M, Crichton K, Ding SL, Fong O, Garren E, Glandon A, Gouwens NW, Gray J, Graybuck LT, Hawrylycz MJ, Hirschstein D, Kroll M, Lathia K, Lee C, Levi B, McMillen D, Mok S, Pham T, Ren Q, Rimorin C, Shapovalova N, Sulc J, Sunkin SM, Tieu M, Torkelson A, Tung H, Ward K, Dee N, Smith KA, Tasic B, Zeng H. 2021. A taxonomy of transcriptomic cell types across the isocortex and hippocampal formation. *Cell* **184**:3222-3241.e26. doi:10.1016/j.cell.2021.04.021

Yavas E, Gonzalez S, Fanselow MS. 2019. Interactions between the hippocampus, prefrontal cortex, and amygdala support complex learning and memory. *F1000Research* **8**. doi:10.12688/f1000research.19317.1

Zamponi GW, Striessnig J, Koschak A, Dolphin AC. 2015. The physiology, pathology, and pharmacology of voltage-gated calcium channels and their future therapeutic potential. *Pharmacol Rev* **67**:821–870. doi:10.1124/pr.114.009654

Zhang Y, Cao L, Varga V, Jing M, Karadas M, Li Y, Buzsáki G. 2021. Cholinergic suppression of hippocampal sharp-wave ripples impairs working memory. *Proc Natl Acad Sci* **118**:e2016432118. doi:10.1073/pnas.2016432118/-/DCSupplemental

Zhou H, Kim SA, Kirk EA, Tippens AL, Sun H, Haeseleer F, Lee A. 2004. Ca2+-binding protein-1 facilitates and forms a postsynaptic complex with Cav1.2 (L-type) Ca2+ channels. *J Neurosci* **24**:4698–4708. doi:10.1523/JNEUROSCI.5523-03.2004

Zoukimian C, Meudal H, Waard S De, Ouares KA, Nicolas S, Canepari M, Béroud R, Landon C, Waard M De, Boturyn D. 2019. Synthesis by native chemical ligation and characterization of the scorpion toxin AmmTx3. *Bioorganic Med Chem* **27**:247–253. doi:10.1016/j.bmc.2018.12.009

Zucca S, Griguoli M, Malézieux M, Grosjean N, Carta M, Mulle C. 2017. Control of Spike Transfer at Hippocampal Mossy Fiber Synapses In Vivo by GABAA and GABAB Receptor-Mediated Inhibition. *J Neurosci* **37**:587–598. doi:10.1523/jneurosci.2057-16.2017

9. BIBLIOGRAPHY OF THE CANDIDATE'S PUBLICATIONS

Publications related to the Ph.D. dissertation

- Raus Balind, S., Magó, Á., Ahmadi, M., Kis, N., Varga-Németh, Z., Lőrincz, A., & Makara, J. K. (2019). Diverse synaptic and dendritic mechanisms of complex spike burst generation in hippocampal CA3 pyramidal cells. *Nature Communications, 10*(1), 1859.

- Magó, Á.*, Kis, N.*, Lükő, B., & Makara, J. K. (2021). Distinct dendritic Ca^{2+} spike forms produce opposing input-output transformations in rat CA3 pyramidal cells. *eLife, 10*, e74493.
  *shared first authors

- Kis, N., Lükő, B., Herédi, J., Magó, Á., Erlinghagen, B., Ahmadi, M., Raus Balind, S., Irás, M., Ujfalussy, B. B., & Makara, J. K. (2024). Cholinergic regulation of dendritic Ca^{2+} spikes controls firing mode of hippocampal CA3 pyramidal neurons. *Proceedings of the National Academy of Sciences, 121*(46), e2321501121.

10. ACKNOWLEDGEMENTS

First and foremost, I would like to express my deepest gratitude to my supervisor, Judit Makara, who has supported and guided me ever since I joined her lab as a BSc student. I am especially thankful for her guidance in teaching me how to perform patch-clamp recordings and for encouraging me throughout my scientific journey.

I am grateful to the entire lab for creating a warm and motivating atmosphere.
I would like to thank my former colleague, Ádám Magó, for helping me overcome the technical difficulties I faced in the early days of my electrophysiological experiments.
Special thanks to my colleagues, Zsófia Varga-Németh and Snezana Raus Balind, for their friendship, which made both the everyday work and the tougher moments in the lab much more enjoyable. I am especially thankful to Zsófi for consistently preparing excellent slices and assisting me with experiments, and to Snezana for her continued encouragement and for the many inspiring scientific and non-scientific discussions we shared.

I would like to thank to Brunner János who was my internal reviewer, who gave useful comments, suggestions and very good questions about my thesis.

To my friends and colleagues outside the lab, thank you for your encouragement and for reminding me that life exists beyond the microscope and the electrophysiology rig.

Finally, and most importantly, I would like to thank my family for their love and support. To my parents, my sister and my partner, thank you for always believing in me and standing by me through every challenge.

This thesis would not have been possible without all of you.